Improving the Performance and Reproducibility of Lead - Tin Perovskite Absorbers Toward All-Perovskite Tandem Solar Cells

Michael D. Farrar

Corpus Christi College

University of Oxford

A thesis submitted for the degree of

Doctor of Philosophy

Trinity 2022

Acknowledgements

Well, it's taken a while and thanks to COVID-19 it felt like an age. It has however, been a most excellent adventure and I have many to thank.

First and foremost, I must thank my family, who have supported me throughout my life and this DPhil. Through several extremely challenging moments, they never wavered in their support. Without them I wouldn't have gotten far enough to start the DPhil let alone the courage to finish it.

Secondly, I'd like to thank Professor Henry Snaith. Thank you for the opportunity and for your abundant positivity, enthusiasm, and scientific knowledge. I'm also glad you're just as you appear on YouTube–I made the right choice. Massive thanks must go to Clare Maloney, who holds the group together and has helped me so much, especially since COVID hit. A huge thank you must also go to the staff at my college, Corpus Christi, and in particular Andy Rolfe for his help with accommodation. I would also like to thank the Engineering and Physical Sciences Research Council Centre for Doctoral Training in Plastic Electronic Materials for my funding.

Now on to my colleagues and friends. I must thank Matt Klug for starting me off on my lead-tin journey and for being an excellent mentor. James Ball, for his fountain of knowledge, candour, and friendship. Grey, for all his help, patience, and almost finishing the solar sim. Suhas Mahesh, for teaching me so much at the start of my DPhil and his continuing help from a far. Augustin, for supporting me with more than his friendship multiple times, you have truly been a lifesaver and more like a brother to me over the years. Derek, who has become a friend for life and given me many a side-splitting moment and very fond memories…and some sweet Excel sheets.

To the pre-COVID crew, you know who you are…we had a blast. To the post-COVID crew thank you for reigniting the group and my enthusiasm for the science…especially Mr Enthusiasm, my running buddy, Jake. A special mention must go to David for his help in the final push toward this thesis, and to Pietro for helping me understand some of the topics that had eluded me over the years.

To Lau, thank you for your love and support and for being with me always, through the rough and the smooth. Lastly, I must thank the Stone Daddies – Anders, Wardy and Laurens for their omnipotent friendship, support, and general awesomeness. Thanks, my dudes!

Abstract

This thesis explores a subset of hybrid perovskites that incorporate tin into their crystal lattice alongside lead. Hybrid perovskite semiconductors have gained global interest over the past decade due to their remarkable optoelectronic properties, and excellent power conversion efficiencies, which now compete with well-established commercial technologies. By incorporating tin, these materials can achieve band gaps far narrower than their pure-lead counterparts. This property makes lead-tin perovskite materials suitable for the construction of all-perovskite tandem solar cells to improve power conversion efficiencies beyond the theoretical limit for a single junction device. Although these materials are promising and have been successfully demonstrated to achieve high power conversion efficiencies, they are still far below their theoretical efficiency and comparatively few studies have been conducted on how to maximise the potential of this class of materials. The work presented in this thesis explores three topics utilising an $FA_{0.83}Cs_{0.17}Pb_{0.5}Sn_{0.5}I_3$ absorber. In the first instance a bulk passivation strategy is investigated with the aim to reduce non-radiative recombination in the absorber material, using several thiocyanate additives that are found to successfully enhance the photoluminescence quantum efficiency of the material and improve charge carrier diffusion length. Proceeding this, the influence that selective contact materials have on non-radiative recombination is explored culminating with a passivation strategy at the interface with the electron transport material. This led to enhanced

performance of resulting devices. Chapter 5 details the fabrication of 2T-monolithic tandem solar cells. The successful resolution of fabrication issues, and optimisation of the lead-tin sub-cell generated highly efficient tandem solar cells. The final experimental chapter in this thesis investigates the removal of DMSO from the lead-tin precursor ink due to its ability to oxidise Sn^{2+} to Sn^{4+}, which can cause detrimental effects within the material. This is achieved by the addition of the ammonium halide salt DMACl. It is shown that highly oriented thin films can be fabricated with enhanced grain sizes leading to a much-improved device stability, in air, of over four times that of the device utilising DMSO.

List of Publications

Open-circuit and short-circuit loss management in wide-gap perovskite p-i-n solar cells
Pietro Caprioglio, Joel A. Smith, Robert D. J. Oliver, Akash Dasgupta, Saqlain Choudhary, **Michael D. Farrar,** Alexandra J. Ramadan, Yen-Hung Lin, M. Greyson Christoforo, James M. Ball, Jonas Diekmann, Jarla Thiesbrummel, Karl-Augustin Zaininger, Xinyi Shen, Michael B. Johnston, Dieter Neher, Martin Stolterfoht & Henry J. Snaith
Nature Communications volume 14, Article number: 932 (2023)

Universal current losses in perovskite solar cells due to mobile ions
Jarla Thiesbrummel, Vincent M Le Corre, Francisco Peña-Camargo, Lorena Perdigón-Toro, Felix Lang, Fengjiu Yang, Max Grischek, Emilio Gutierrez-Partida, Jonathan Warby, **Michael D Farrar**, Suhas Mahesh, Pietro Caprioglio, Steve Albrecht, Dieter Neher, Henry J Snaith, Martin Stolterfoht
Advanced Energy Materials 11 (34), 2101447

Revealing Ultrafast Charge-Carrier Thermalization in Tin-Iodide Perovskites through Novel Pump–Push–Probe Terahertz Spectroscopy
AM Ulatowski, **MD Farrar**, HJ Snaith, MB Johnston, LM Herz
ACS photonics 8 (8), 2509-2518

Impact of Tin Fluoride Additive on the Properties of Mixed Tin-Lead Iodide Perovskite Semiconductors
KJ Savill, AM Ulatowski, **MD Farrar**, MB Johnston, HJ Snaith, LM Herz
Advanced Functional Materials 30 (52), 2005594

Metal composition influences optoelectronic quality in mixed-metal lead–tin triiodide perovskite solar absorbers
Matthew T Klug, Rebecca L Milot, Jay B Patel, Thomas Green, Harry C Sansom, **Michael D Farrar**, Alexandra J Ramadan, Samuele Martani, Zhiping Wang, Bernard Wenger, James M Ball, Liam Langshaw, Annamaria Petrozza, Michael B Johnston, Laura M Herz, Henry J Snaith
Energy & Environmental Science 13 (6), 1776-1787

Dual-Source Coevaporation of Low-Bandgap $FA_{1-x}Cs_xSn_{1-y}Pb_yI_3$ Perovskites for Photovoltaics
James M Ball, Leonardo Buizza, Harry C Sansom, **Michael D Farrar**, Matthew T Klug, Juliane Borchert, Jay Patel, Laura M Herz, Michael B Johnston, Henry J Snaith
ACS Energy Letters 4 (11), 2748-2756

Microsecond carrier lifetimes, controlled p-doping, and enhanced air stability in low-bandgap metal halide perovskites
Alan R Bowman, Matthew T Klug, Tiarnan AS Doherty, **Michael D Farrar,** Satyaprasad P Senanayak, Bernard Wenger, Giorgio Divitini, Edward P Booker, Zahra Andaji-Garmaroudi, Stuart Macpherson, Edoardo Ruggeri, Henning Sirringhaus, Henry J Snaith, Samuel D Stranks
ACS energy letters 4 (9), 2301-230

Contents

Chapter 1

Introduction

Human development and energy consumption are intimately linked[1]. In the 18th century humans exploited the combustion of hydrocarbons to facilitate the industrial revolution and improve the lives of millions of people[2]. However, the hydrocarbons used are formed of long since dead plants and animals that sequestered the carbon, now trapped within these molecules, over the course of millions of years. By burning these hydrocarbons, humans are releasing eons of carbon far quicker than it was captured in vast quantities. The release of carbon in the form of CO_2 by burning these fuels is causing the Earth's temperature to rise as infrared radiation (heat) that would otherwise escape the atmosphere is absorbed[3,4]. The Earth's average temperature has risen by 1 °C since 1900, and more than half this increase in temperature happened since 1970[5]. In 2022 the UK and several countries across Europe saw record breaking temperatures[6,7]. Sporadic weather patterns, the reduction of Arctic ice and ancient glaciers[8,9], and the displacement of millions of species of animals by the change to their habitats[10–13] - including humans have accompanied this change[14]. To protect the current climate, humans must adapt and utilise renewable, non-polluting energy sources to stall this rise in global temperature and protect life on Earth, which as Carl Sagan once said "is the only world known so far to harbour life. There is nowhere else…"[15]. A source of energy that does not

cause the release of CO_2, is from the direct conversion of sunlight into electricity via photovoltaics (PV). The Sun, the largest object in our solar system, has been providing the earth with enough energy to power its weather systems, and the growth of all life on earth for billions of years. The Sun provides the Earth with around 50,000 exajoules (EJ) of harvestable energy annually[16], the World's primary energy consumption for all sources in 2021 was 595.15 EJ[17] two orders of magnitude less than this value. Despite this, solar power accounted for less than 2% of primary power generation in 2021, with fossil fuels accounting for 77%[17].

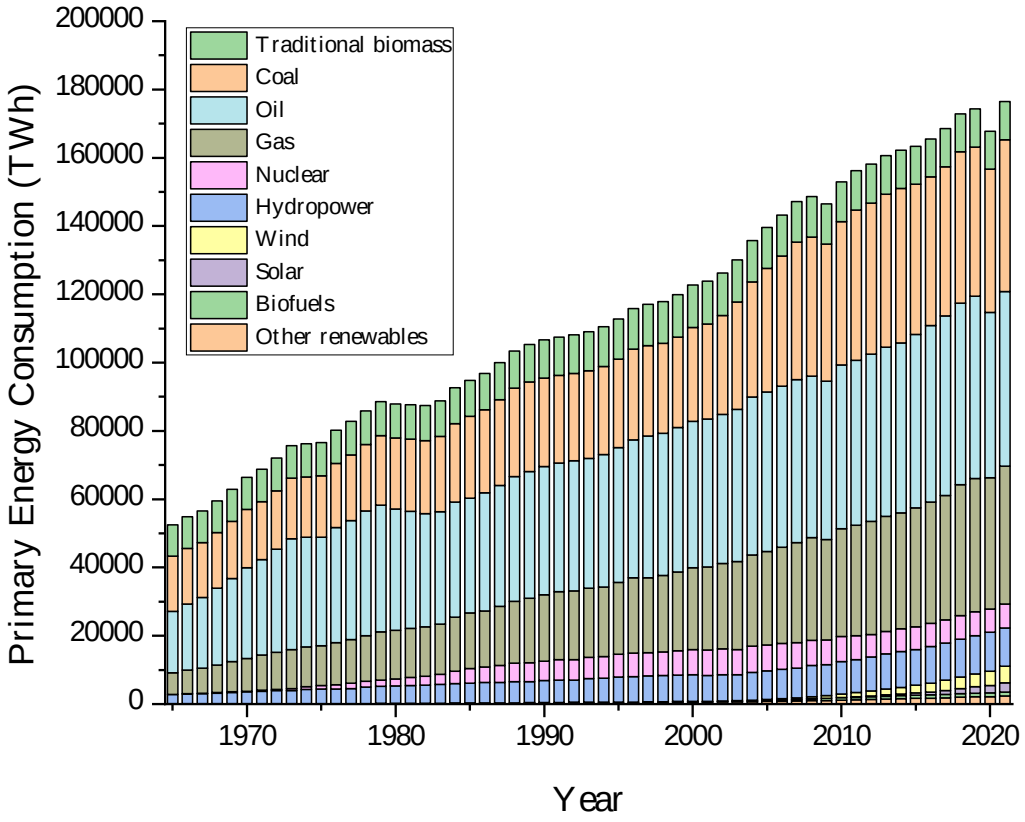

Figure 1.1 – Global primary energy consumption by source from 1965 – 2021. Plotted using data from *BP Statistical Review of World Energy 2022*[17].

By using photovoltaics, we can harvest a clean and incredibly energy dense power supply that will last billions of years[18]. The key to harvesting light from the Sun is efficient cost-effective PV. Silicon is the dominant technology in the PV space in 2022 and has been for over 60 years[19]. The decreasing cost of silicon PV has made solar power more viable than ever before, and silicon is likely to be the dominant technology in large scale power generation for years to come[19]. However, silicon does have some drawbacks, it is energy-intensive to manufacture silicon wafers and its electronic properties require wafers used in solar cells to be thick, making them heavy and brittle as a result[20]. This creates a niche for emerging thin-film, solar technologies, which are less energy intensive to produce given their facile fabrication methods, and excellent absorption properties. The reduction in weight of thin-film technologies, compared to silicon, also allows them to exploit new markets where weight is a major concern such as consumer electronics which, in most cases are portable, and vehicles such as drones[21]. Their ductility also allows for them to be used in applications where flexible solar panels are required, for example in the wearable technology market, the growing number of Internet of Things (IoT) devices and Radio Frequency Identification (RFID) tags[22]. One such thin-film material that has seen a remarkable increase in research interest and power conversion efficiency is hybrid perovskites. Since their discovery as a photovoltaic material in 2009 they have gone from 3.8% efficient[23] to 25.8% efficient[24]. Showing excellent absorption, charge carrier properties, and a vast array of possible processing methods from roll to roll,

inkjet printing and vacuum deposition[25]. These materials due to the nature of their electronic properties can be fabricated on top of silicon solar cells to make them more efficient - overcoming the efficiency limit for a single photovoltaic cell alone[26]. Hybrid perovskites can also be fabricated into multijunction cells by stacking multiple cells on top of each other and increasing their power conversion efficiency further[27].

Whilst devices made from hybrid perovskites show remarkable potential, they are still in the early stages of development and require additional research into their fundamental properties to increase power conversion efficiency. A subset of these materials that utilise two metals within their crystal lattice, lead (Pb) and tin (Sn), can form very narrow band gaps (see Chapter 2) close to that of silicon. This allows them to be deployed into all-perovskite multijunction solar cells, making them an excellent candidate for future power generation. However, due to thermodynamic instability and stricter processing conditions, these materials have received comparatively less attention than the main family of lead-based hybrid perovskites. The study of a lead-tin perovskite absorber material, toward high efficiency all-perovskite tandem devices is the topic of this thesis.

Chapter 2

Theory and Background

Solar cells utilise the properties of semiconductors for their operation. This chapter summarises the theory of semiconductors and how the photovoltaic effect arises from the band structure of solids and molecular orbitals. Proceeding this, the theory and operation of photovoltaic devices is described leading on to an overview of perovskite semiconductors as photovoltaic materials and their application in tandem solar cells.

2.1 Band theory

Whether a material behaves as a metal, an insulator or a semiconductor is dependent on the electronic structure of the material. This electronic structure is governed by the atoms within the material and how these atoms interact and bond with each other. When two atoms are in close enough proximity their atomic orbitals may overlap to form a bond. When this occurs for multiple atoms, this is deemed a molecule. The overlap of these orbitals allows for the formation of bands. Bands, and the band gap between them, are fundamental in understanding the working principles of a solar cell.

2.1.1 The Hydrogenic Atom

To build a band model, an important starting point is the hydrogenic atom. The time independent Schrödinger equation for a hydrogenic atom is[28],

$$-\frac{\hbar^2}{2m}\frac{d^2\psi(x)}{dx^2} + V\psi(x) = E\psi(x) \tag{2.1}$$

where E represent the allowed energies of an electron, ψ is the wavefunction and represents the probability distribution of the electron. $\hbar$ is the reduced Planck constant, m is the reduced mass of the electron and V is the potential energy. When electrons are within an orbital the potential energy required to leave an atom can be considered infinite (for the purpose of calculation) with this assumption the particle in the box or infinite quantum well model can be used to describe the system. First, a box must be constructed, as in Figure

2.1, with sides of infinite potential and a floor of 0 potential inside the box with an electron inside it.

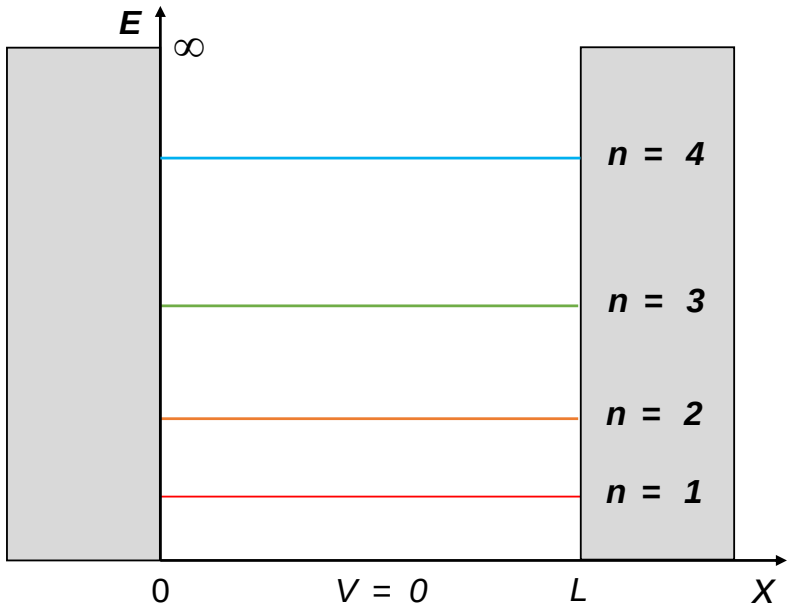

Figure 2.1 - An infinite quantum well, a model used to give solutions to the Schrödinger equation for an electron bound to an atom. *V(x) = 0* from $0 \leq x \geq L$ otherwise $V = \infty$.

For this electron within the box at *V=0* the equation becomes,

$$-\frac{\hbar^2}{2m}\frac{d^2\psi(x)}{dx^2} = E\psi(x) \tag{2.2}$$

As the free electron is of zero potential the spatial frequency of this wave can be described by,

$$k = \sqrt{\frac{2mE}{\hbar^2}} \tag{2.3}$$

Which then gives,

$$-k^2\psi = \frac{d^2\psi(x)}{dx^2} \tag{2.4}$$

Plugging in the solutions $\psi = A\sin(kx) + B\cos(kx)$ within the boundary conditions gives $k = n\pi/L$ the following relationship can then be derived[28],

$$E = \frac{\hbar^2}{2m}\left(\frac{n\pi}{L}\right)^2 \tag{2.5}$$

From equation 2.5 the energy of the electron in the well is quantised and can only take certain integer values i.e., $n = 0$, $n = 1$ etc. as shown in Figure 2.1. This solution gives the principal quantum number n. Within the one electron atomic model the potential energy is centrosymmetric (angle independent), this allows for the separation of the wavefunction into radial and angular parts[28],

$$\psi(r, \theta, \phi) = R(r)Y(\theta, \phi) \tag{2.6}$$

Solving the angular part of this equation gives the two other quantum numbers l *and* m_l which specify the angular momentum of the electron around the nucleus. These quantities can be combined to calculate the probability finding an electron around the nucleus (which is essentially what an atomic orbital is). Using the 3 quantum numbers, boundary surfaces can be constructed which represent these atomic orbitals shown in Figure 2.2. These orbital surfaces represent a 95% probability of finding an electron[29]. With multi-electron systems these orbitals can be filled obeying the Aufbau principle and Pauli exclusion principle. Electrons that occupy the outermost

orbitals (larger values of n) can participate in bonding and are called the valence electrons.

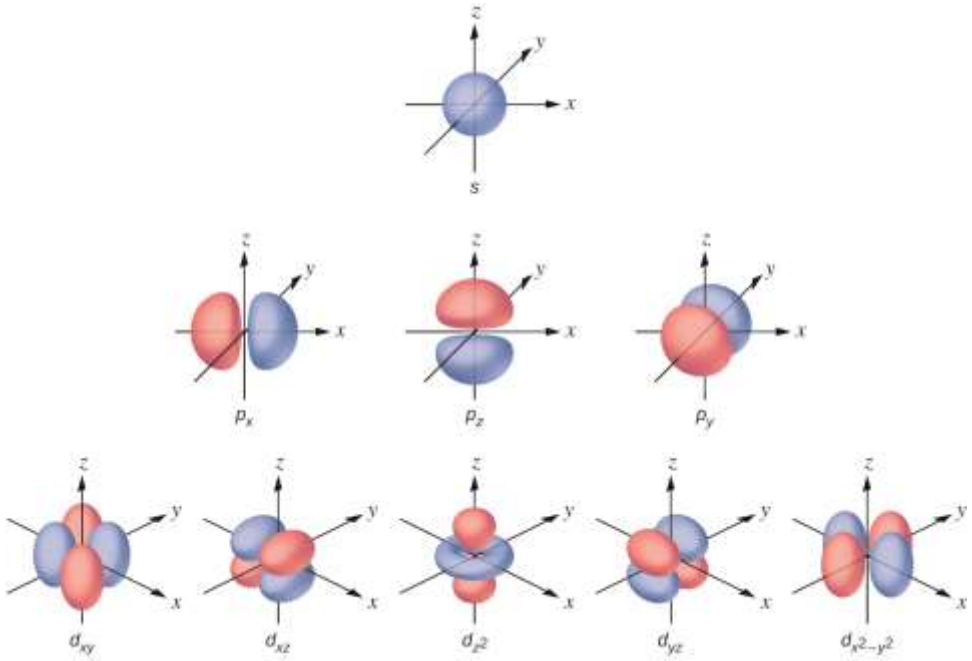

Figure 2.2 - The boundary surfaces predicted for atomic orbitals for different values of n, l and m. Boundary surface picture adapted from[30] under a creative commons license.

2.1.2 Linear Combination of Atomic Orbitals

The orbitals for an atom (A) described in the previous section can participate in bonding via a favourable overlap from a neighbouring atomic orbital (B). Now A and B have overlapped, electrons can be found in either orbital, the overall wavefunction in this condition is a super position of the two orbitals[28] such that,

$$\psi_{\pm} = N(A \pm B) \tag{2.7}$$

Where N is a normalisation factor. The term for this superposition is a linear combination of atomic orbitals (LCOA) and an approximate molecular orbital formed from LCOA is called an LCOA-MO. This superposition results in the two probability densities for the electrons one where the orbitals overlap constructively, and the density is found in the internuclear region (bonding) and one where the orbitals overlap destructively and are excluded from this region (anti-bonding). As N atoms (and orbitals) are added to this linear combination, bonding, and anti-bonding orbitals that are degenerate (the same energy) become hard to distinguish and they can then be described as band. By using LCOA-MO the electronic structure of a material such as a crystal lattice can be calculated, this is depicted in Figure 2.3. The antibonding orbitals in this case are considered empty and the bonding orbitals full. Electrons can only move through the material if promoted into empty orbitals (see conduction band further into this chapter).

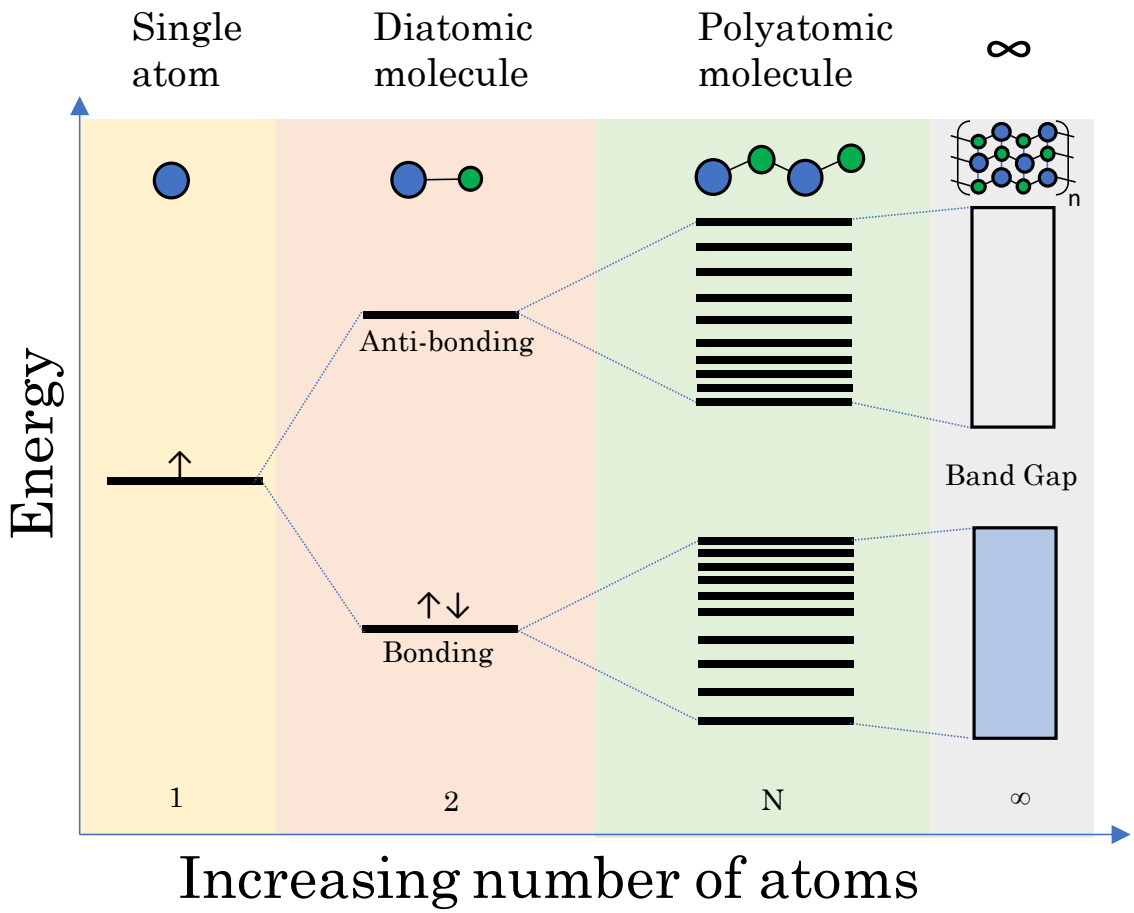

Figure 2.3 - The LCOA approximation for an increasing number of atoms. The band gap, conduction band, and valence band are shown. These are analogous to the LUMO and HOMO in organic molecules. (Highest unoccupied molecular orbital, lowest unoccupied molecular orbital respectively).

2.1.3 Predicting band structure

The LCOA-MO approach can model the structure of bands in a solid. An extension to this model, the tight binding model, is better suited to describing the structure of the bands formed in conjunction with LCOA-MO. The tight binding model is simplistic but can describe the properties of a material such as conductivity and importantly semi-conductivity.

2.1.4 The Tight-Binding Approximation

The tight binding approximation uses an infinite line of 1D, periodic potentials to represent atoms as shown in Figure 2.4.

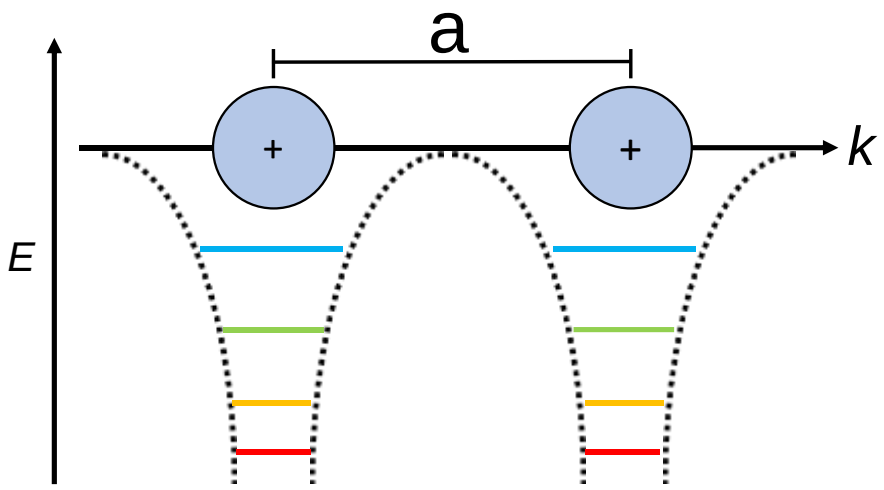

Figure 2.4 - An illustration of the tight binding approximation. A 1D-chain of atoms is spaced by a and their s-orbitals overlap. The resulting band structure for this simple model is shown above

This periodic model approximates a unit cell, which is the smallest arrangement of atoms that forms a crystal lattice if propagated infinitely in three dimensions. Using this model, a Bloch function can be constructed that provides solutions to the Schrödinger equation and satisfies the periodic potential. This can then be used to describe electronic states in this periodic structure.

$$\psi(x) = e^{ik.x}u(x) \tag{2.8}$$

Where e^{ikx} is the plane wave wavefunction of the free electron and $u(x)$ is a periodic function, representing the periodic nature of the model. Using the LCOA approximation and Bloch function in equation 2.8, the band structure can be predicted for various materials as shown in Figure 2.5. The size of the gap between the valence and conduction bands (VB,CB) dictates whether a material will have insulating, semiconducting or metallic properties. The band gap (E_g), as will be reviewed, is an incredibly important property of semiconductors and can be utilised in a range of devices such as light emitting diodes (LEDs), transistors, and photovoltaics (PV). The conduction band, formed of empty states, as previously discussed, allows for electrical conductivity when electrons are present. In a metal the states in the valence band and conduction band overlap meaning no extra energy is required to promote an electron into the conduction band.

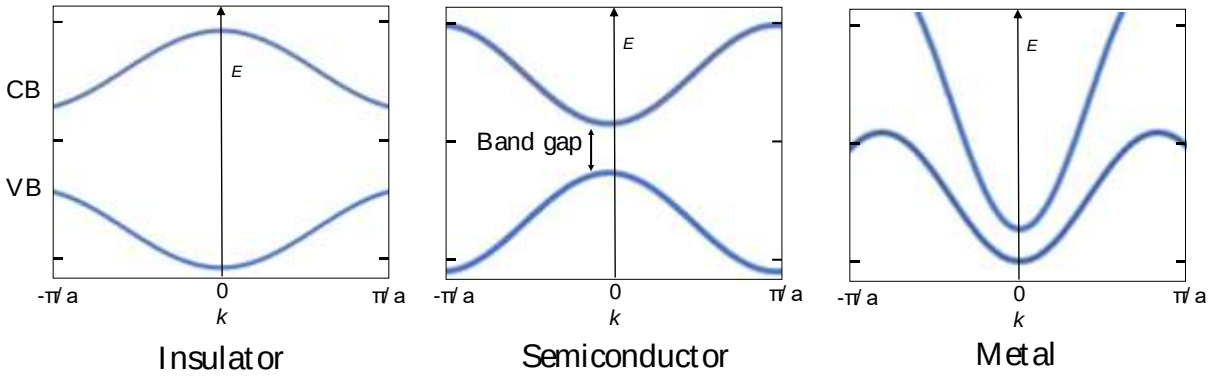

Figure 2.5 - The band structures for simplified models of an insulator, a semiconductor, and a metal. The band gap is labelled for the semiconductor in between the valence and conduction bands.

In a semiconductor an electron must be provided with an energy greater than or equal to that of the band gap for electrons to be promoted to the conduction band and contribute to electrical current. This energy can be provided by a photon as will be described later in this chapter.

2.1.5 Direct and indirect band gaps

Whether a band gap in a semiconductor is direct or indirect (Figure 2.6) depends on the relative position of the CB minimum and VB maximum in terms of *k*. When the CB minimum and VB maximum are aligned a photon of energy $hf \geq E_g$ can excite an electron from the VB into the CB, a direct transition. For an indirect band gap material such as silicon the CB and VB do not coincide at the same value of *k*. Due to conservation of momentum, the event must in include the absorption of a phonon. As a result, light absorption in indirect band gap materials is less likely, and those used in PV must be thicker (100 – 500 μm) than direct band gap materials (<1 μm).

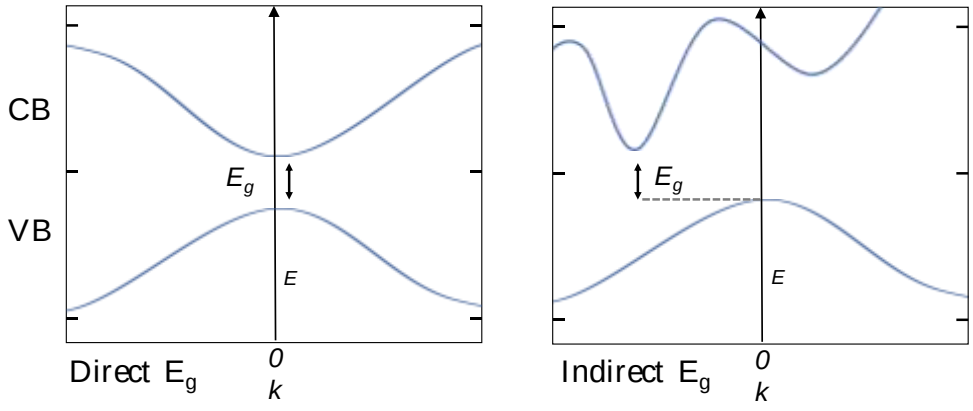

Figure 2.6 - Simple energy band diagrams for a direct and indirect semiconductor.

2.1.6 The Fermi Level

Having established background on the electronic band structure it is important to understand how the electrons are distributed within a material this can be described by the Fermi-Dirac distribution. In solids electrons obey Fermi- Dirac statistics[31]. The Fermi-Dirac distribution gives the probability that an energy level at a given temperature will be occupied by an electron,

$$f(E) = \frac{1}{1+\exp\left(\frac{E-E_f}{kT}\right)} \tag{2.9}$$

where k is the Boltzmann constant, T is the temperature, and E_F is the energy of the Fermi level. The Fermi level (E_F) is the energy at which there is a 50% probability of finding an occupied state for a given temperature. The Fermi level of an intrinsic semiconductor lies in the middle of the band gap. This can be shifted within a semiconductor by *p* or *n*-doping the material. This shifts the Fermi level towards the conduction band in the case of an *n*-type semiconductor and shifts the Fermi level downwards closer to the valence band in the case of a *p*-type semiconductor.

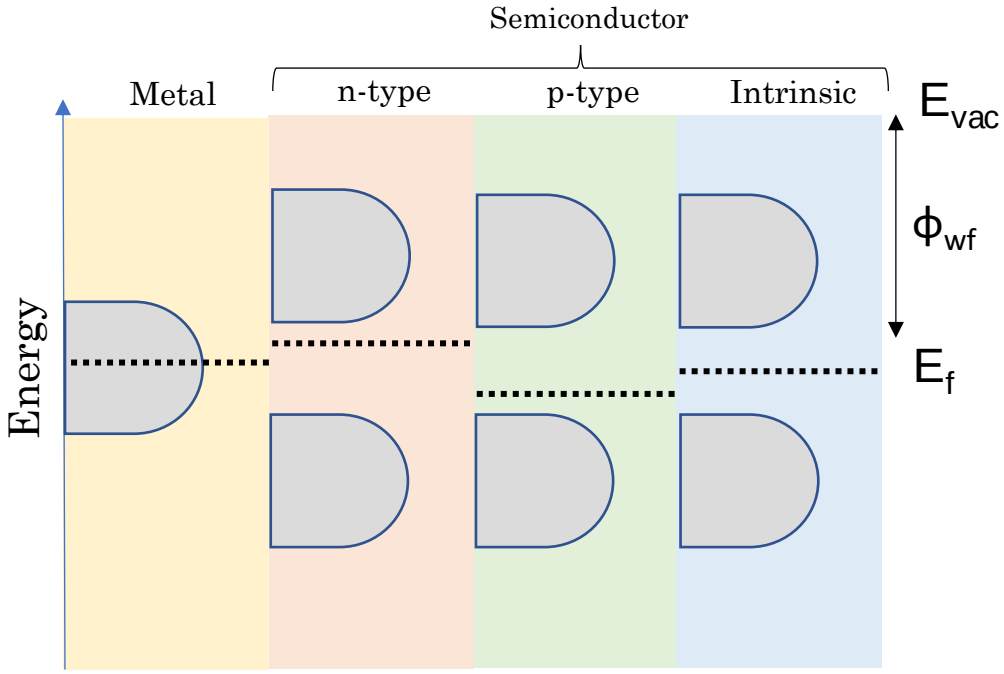

Figure 2.7 - Depicting the shift in Fermi level (E_f) for a metal and 3 types of semiconductors.

When two materials come into to contact with each other (such as in a *p*-*n* junction) their Fermi levels will move to align until an equilibrium is reached this can be taken advantage of in devices which will be discussed in detail later in this chapter.

2.2 Device fundamentals

2.2.1 Absorption, emission, and recombination

Absorption of a photon to promote an electron in semiconducting materials is fundamental to the photovoltaic effect. As previously mentioned, a direct band gap will not absorb a photon of energy less than the band gap, it will pass straight through the material. If the energy of the photon is greater than or equal to the band gap ($hf \geq E_g$) then the photon is absorbed and an electron

is promoted from the valence band to the conduction band, leaving behind a hole in the valence band. If the photon is of an energy greater than the band gap ($hv > E_g$) then the electron is promoted into an energy level higher than the conduction band edge. It will then thermalise back to the conduction band edge dissipating the extra energy as heat to the lattice and represents a loss pathway in solar cells.

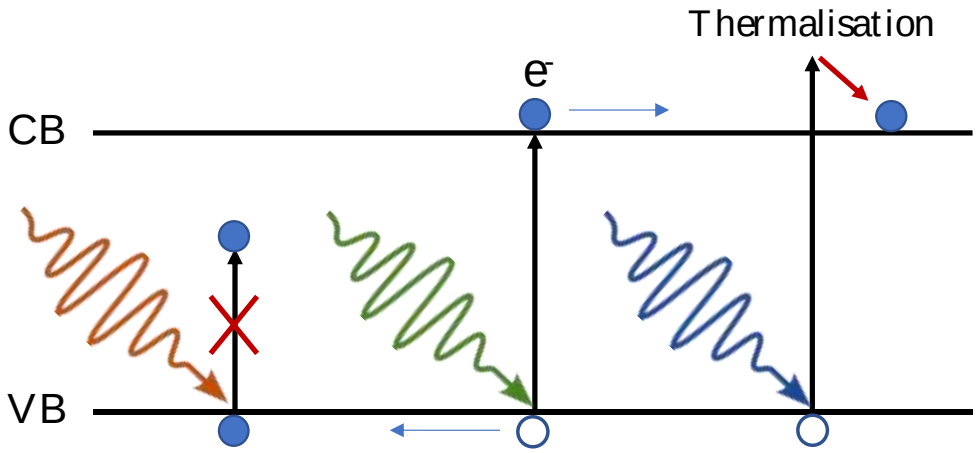

Figure 2.8 - Depicting transmission, absorption of a photon, and thermalisation of an electron back to the CB edge.

In a solar cell, once the absorption event occurs and carriers are generated, the electron hole pair, called an exciton, must be separated into holes and electrons and travel through the material to be collected by their respective electrodes. Excitons come in two types Frenkel and Wannier-Mott[32]. Frenkel excitons are tightly bound by Coulombic interaction and are usually found in organic semiconductors. In most inorganic semiconductors excitons are of the Wannier- Mott type in which the Coulomb interaction is screened by a large dielectric constant. This gives Wanner-Mott excitons a low binding energy,

around 0.01 eV for silicon[31], which means at room temperature there is sufficient energy to separate them into free electrons and holes (k_BT is roughly 0.026 eV at 300 K). Once charges have been separated, they can move within the material via two processes, drift and diffusion. The combination of which contributes to the overall current and can be described by the 1D drift-diffusion equation,

$$J = q(n\mu_n + p\mu_p)E + q(D_n\frac{dn}{dx} + D_p\frac{dp}{dx}) \tag{2.10}$$

where J is the current density, μ_n and μ_p are the mobilities of electrons and holes respectively and D_n and D_p are the diffusion coefficients for holes and electrons respectively. E is the applied field.

Before charges can be extracted, the carriers can encounter three types of recombination pathway[33]; bimolecular- radiative (band to band) recombination, and two types of non-radiative recombination, monomolecular (trap assisted) and trimolecular (Auger). Bimolecular is a radiative process (as in LEDs) where the electron recombines with a hole in the valence band and emits a photon of energy $hf = E_g$. Monomolecular recombination (Shockley-Read-Hall) occurs via various defects in the material that results in electronic states within the band gap. This process is non-radiative, and energy is lost via phonons consequently. In Auger recombination the excess energy from electron-hole recombination is passed onto another electron in the conduction band. This is electron is promoted to a higher energy level in the conduction band. In Perovskites, Auger recombination typically only

occurs for excitation densities many times greater than that of typical solar cell illumination conditions (i.e., under concentrated sunlight). The main recombination pathways relevant to this thesis are monomolecular and bimolecular. If radiative recombination occurs because of an excitation from a photon, it is called photoluminescence.

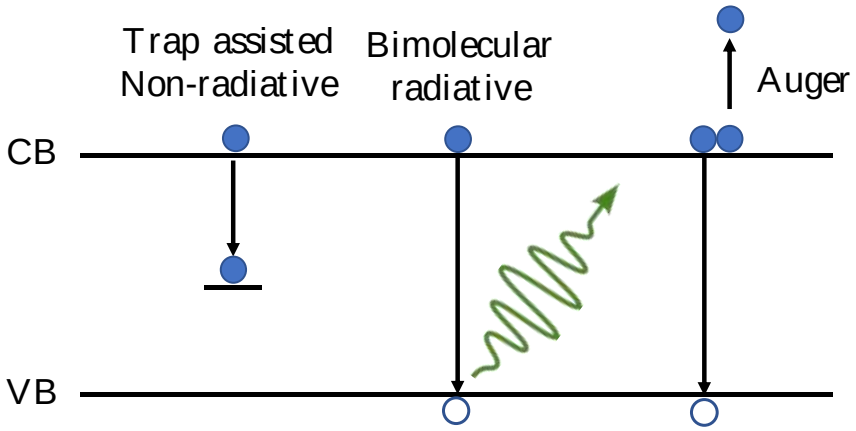

Figure 2.9 – The three recombination pathways in semiconductor materials after an excitation event.

If carriers are not extracted, they must recombine[34].The amount of time a free carrier spends before recombining is defined as the lifetime (τ). By considering only bulk recombination and the mechanisms described above, the total recombination lifetime can be calculated by,

$$\frac{1}{\tau} = \frac{1}{\tau_{trap}} + \frac{1}{\tau_{rad}} + \frac{1}{\tau_{auger}} \tag{2.11}$$

Additionally, non-radiative recombination can happen at surface defects, grain boundaries, and interfaces with charge selective layers[35]. To measure the amount of radiative recombination within a material, its

photoluminescence quantum efficiency (PLQE) can be measured. This is performed by illuminating a sample with a light source of known photon flux and measuring the number of emitted photons using a sensitive detector. PLQE is the ratio of the emitted photons (radiative recombination) to those absorbed, and the difference gives the total number of radiative events happening within a material,

$$PLQE = \frac{\varphi_E}{\varphi_A}$$

Where φ_E and φ_A are the flux of emitted and abosrbed photons respectively. More details of a PLQE measurement setup can be found in Chapter 3.

2.2.2 Photo generated carriers and the Fermi level

Under steady state conditions the Fermi level of an intrinsic semiconductor is found in the middle of the band gap and represents the distribution of intrinsic charge carriers (E_{Fi}), equidistant from the conduction band and the valence band. When exposed to light (as in a solar cell), photogenerated charges (shown in Figure 2.8) cause this intrinsic population to shift. The Fermi level is now best represented as a quasi-Fermi level for each carrier and can be calculated for both holes and electrons (E_{Fp} and E_{Fn} respectively). The difference between these levels is called the quasi-Fermi level splitting (QFLS). The QFLS represents the maximum voltage obtainable from a solar cell with perfect contact materials such that $QFLS = qV_{OC}$. Although the positions of the E_{Fp} and E_{Fn} are somewhat inaccessible the QFLS can be measured by PLQE[36].

2.2.3 Photovoltaic devices

In this section examples of a *p-i-n* junction and the working principles are discussed to give background on the types of devices fabricated in this thesis. A *p-i-n* junction is formed when an intrinsic semiconductor is placed between a p-type and an n-type semiconductor in contact, forming a junction. Electrons from the n-type material diffuse toward the p-type through the intrinsic semiconductor until a steady-state is reached and each of their Fermi levels align with one another. This results in an electric field across the intrinsic semiconductor generated by the space charge region. The built-in field results in the formation of a diode. Under forward bias conditions (V_f) , the width of the space charge region contracts, and charge carriers can flow across it, causing an exponential rise in current. Under reverse bias (V_r) the space charge region expands, causing a larger barrier to extract charge carriers inhibiting current flow. This is called rectifying behaviour.

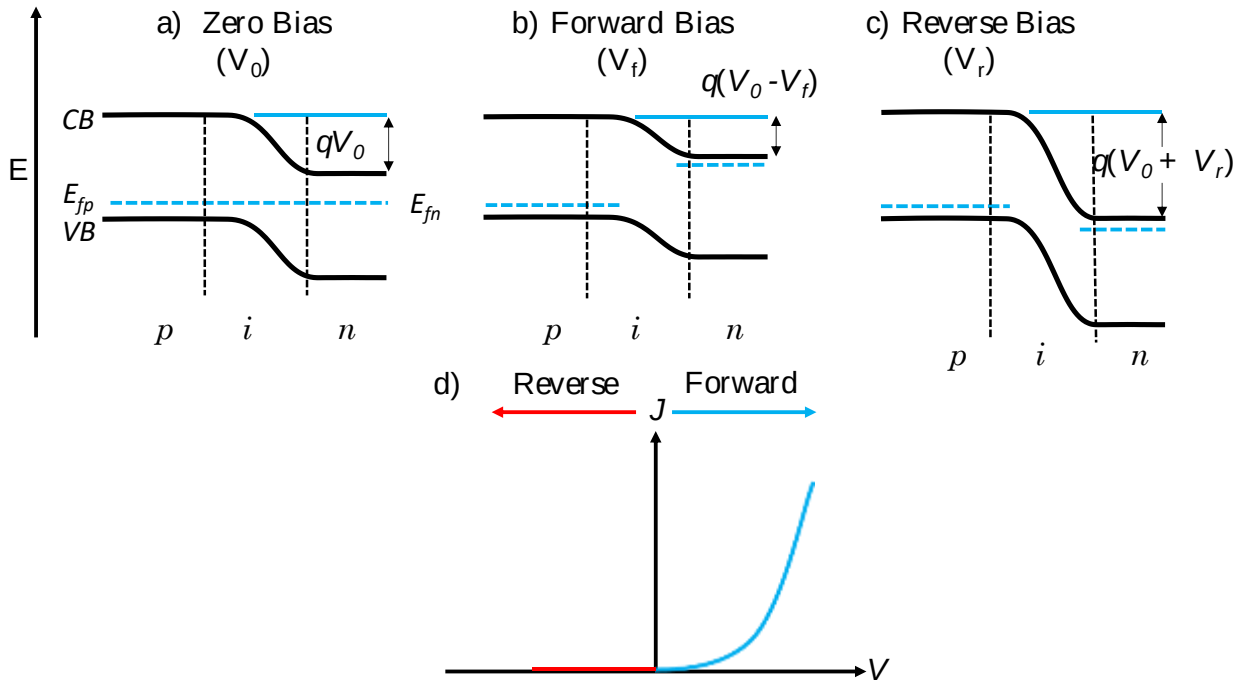

Figure 2.10 - Band energy schematics of a *p-i-n* diode under a) zero bias b) forward bias c) reverse bias. d) shows a typical I-V curve for a rectifying diode.

2.2.4 Solar cell operation

The current that flows through the diode in the dark, under forward bias, is called the dark current (J_{dark}). The device in this regime can be expressed using,

$$J_{dark}(V) = J_o\left(e^{\frac{qV}{k_BT}} - 1\right) \tag{2.12}$$

here J_o represents the dark saturation (leakage) current. When exposed to light and carriers are generated, resulting in a photocurrent that flows in the opposite direction to J_{dark}. When the diode's contacts are connected, without load or bias (short-circuit) all the light generated carriers can be extracted

and is the short-circuit current (J_{SC}). Including this term, the equation then becomes,

$$J(V) = J_{sc} - J_o \left(e^{\frac{qV}{k_B T}} - 1\right) \tag{2.13}$$

Conversely, when the contacts are disconnected, or in open circuit, no carriers can be extracted and therefore no current. In this regime the voltage measured at the contacts will be the maximum voltage the solar cell can produce under light and is called the open circuit voltage (V_{OC}). Given $J = 0$ the diode equation can be rearranged to give,

$$V_{oc} = \frac{k_B T}{q}\left(ln\frac{J_{sc}}{J_o} + 1\right) \tag{2.14}$$

With these values measured it is commonplace to then measure the current-voltage (*J- V)* characteristics of the diode by sweeping the voltage (under both dark and illuminated conditions) and measuring the current at each voltage step. This produces a diode or *J-V* curve. The maximum power achievable for the solar cell is where the product of the voltage and current is greatest ($P = J$ x V). This can also be referred to as the maximum power point (MPP) and can be given in terms of power density (mW/cm^2) or as a power conversion efficiency (PCE) in percent.

Two key parameters that can affect the power output of a PV device are series and shunt resistance. Series resistance (R_S) is the resistance that charges encounter while being extracted and can occur in any part of the device (including the wires in the measurement setup). Its impacts can be seen on a

J-V curve from V_{OC} to MPP for this reason series resistance must be kept as low as possible. Shunt resistance (R_{SH}) is the resistance to leakage current across the diode. Shunt pathways provide the ability for charge carriers to bypass the diode reducing V_{OC} and current through the diode. Shunt pathways can arise from defects in the device's layers such as pinholes. The effect of shunts can be seen in the *J-V* curve from J_{SC} to MPP. To maximise power output, the R_{SH} must be as high as possible. If R_{SH} is very low this can give an effective short-circuit. These effects are shown in Figure 2.11.

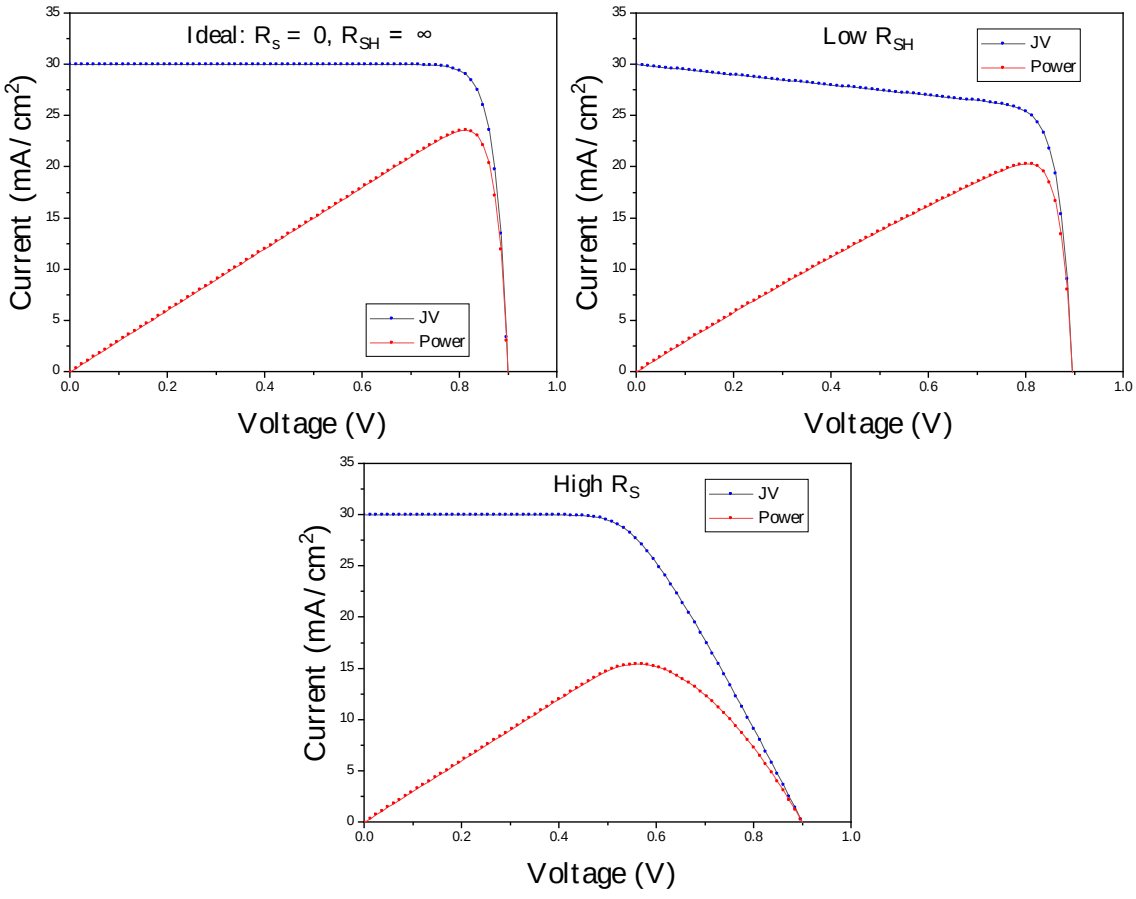

Figure 2.11 – An ideal J-V and power curve and the effect of low R_{SH} (R_{SH}) and high series resistance (R_S) on the J-V and power curves.

The fill factor (*FF*) is another parameter important to solar cell characterisation which can be affected by series and R_{SH}. The fill factor is the ratio of maximum power output (P_{MPP}) versus the product of J_{SC} and V_{OC} and gives a unitless measure of the "squareness" of the diode curve (shown in Figure 2.12).

$$FF = \frac{P_{MPP}}{J_{SC} \cdot V_{OC}} \tag{2.15}$$

By combining J_{SC}, V_{OC} and *FF* into one equation we can arrive at the power conversion efficiency for a solar cell,

$$PCE = JSC \cdot VOC \cdot FF \tag{2.16}$$

Where P_{in} is the incident power (light) irradiating the solar cell. Taking all these factors into account, an equivalent circuit that models a photovoltaic diode can be obtained as seen in Figure 2.12.

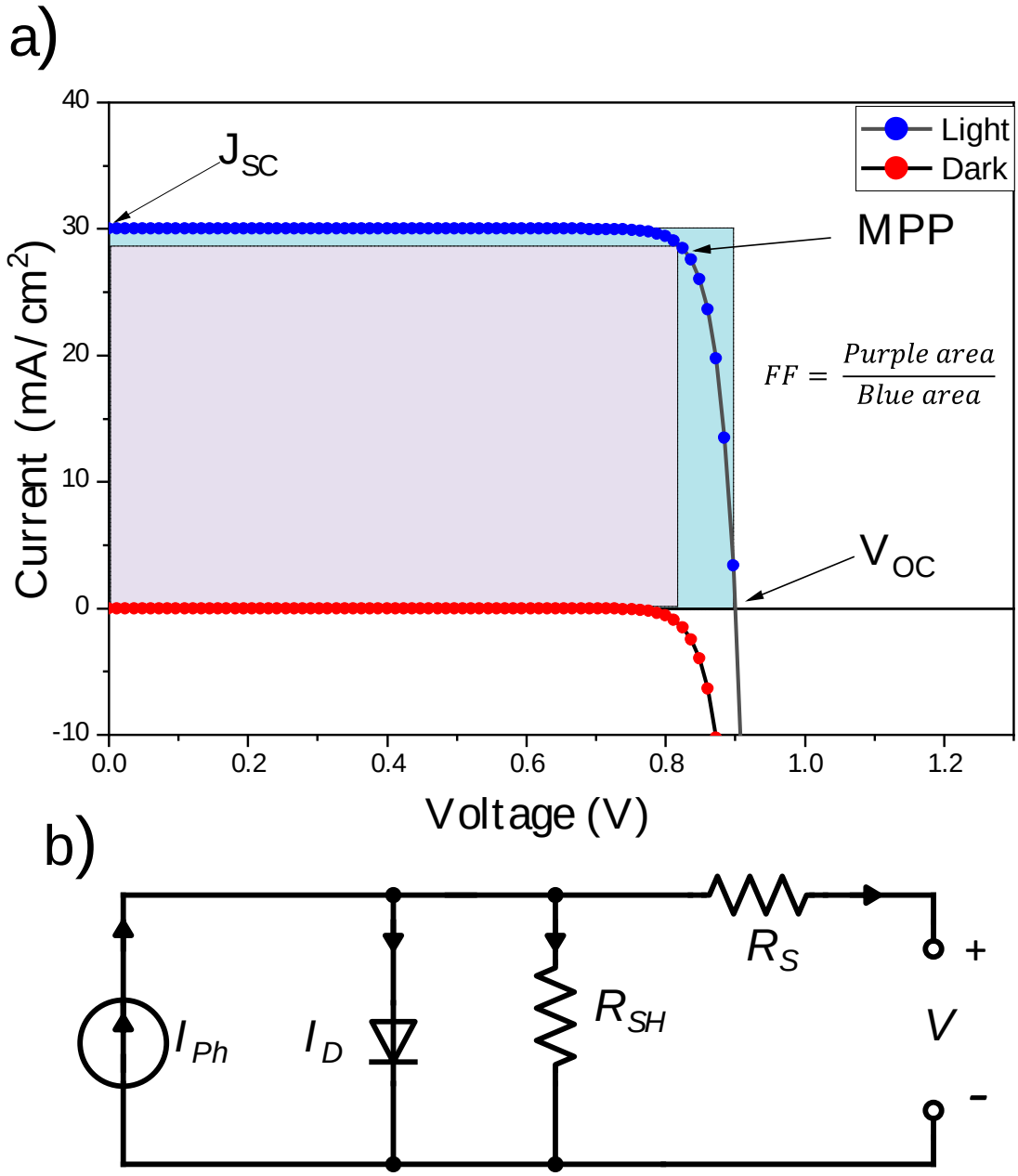

Figure 2.12 - An ideal J-V curve with all parameters indicated and the equivalent circuit model for a photovoltaic cell. Here FF is shown as a ratio between two highlighted areas for clarity. The correct formula is shown in equation 2.15.

2.3 Perovskite Photovoltaics

Perovskites were first discovered in 1839 and are a class of materials with the general stoichiometry ABX_3[37], where the A-site is occupied by a monovalent cation, the B-site a divalent cation, and the X-site a monovalent anion. The first reported perovskite was the naturally occurring $CaTiO_3$ (calcium titanate) and the structure was named after Count Lev Perovski[38]. The subset of hybrid perovskites (having both inorganic and organic components) were first synthesised and reported in 1978[39]. However, it was not until 2009 when Kojima *et al.* created the first solar cell utilising the hybrid-perovskite materials, methylammonium lead iodide (MAPI) and methylammonium lead bromide (MAPBr) that the light harvesting properties of these materials were realised. Kojima *et al.* used them as absorbers in a dye-sensitised solar cell (DSSC) architecture, replacing organic dyes with perovskite nanocrystals, resulting in a PCE of 3.8%[21]. These first cells, however, made use of liquid electrolyte as the hole transporter, comprised of I^-/I_3^- dissolved in an organic solvent, which also rapidly dissolved the perovskite crystals[23]. A step change in efficiency came in 2012 from Lee et *al.* and Kim *et al.* Using a solid-state architecture and the organic, small molecule, hole transporter 2,2′-7,7′-tetrakis(N,N- di-p-methoxyphenylamine)-9,9'-spirobifluorene (Spiro-OMeTAD), Lee *et al.* achieved a PCE of 10.9%[40] and Kim *et al.* 9%[41]. Further work by Stranks *et al.* in 2013 showed that these materials had diffusion lengths exceeding 1 μm, far greater than the absorber layer's thickness[42], displaying their excellent charge carrier properties. Perovskite solar cells

have since shown an incredible rise in efficiency and interest in the research community. They have now achieved a certified efficiency of 25.2%[43] and over the last decade have nearly overtaken the power conversion efficiency of crystalline silicon materials that have been studied for almost 70 years[44].

2.3.1 Structure

Hybrid perovskites adopt the same crystal structure as $CaTiO_3$. The ideal structure is cubic with the A-site cations in cubo-octahederal sites and BX_6 corner sharing octahedra[45].

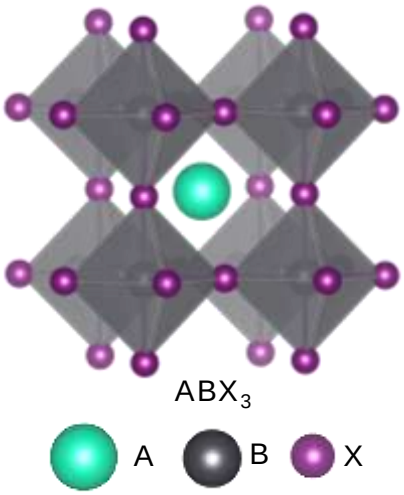

Figure 2.13 - The general cubic perovskite structure.

The hybrid perovskites used in solar cells commonly use caesium, methylammonium or formamidinium at the A-site, usually in a multi-cation configuration. This is achieved by taking advantage of the tolerance factor in perovskites so that cations and anions with similar ionic radii can be interchanged at various sites within the ABX_3 structure[46],

$$t = \frac{r_A + r_X}{\sqrt{2(r_B + r_X)}} \tag{2.17}$$

where r_A, r_B and r_X is the effective radius of either ion and t the tolerance factor. The tolerance factor allows for the prediction of a stable structure formed from a set of chosen ions. Along with the A-site being dynamic in composition, the B-site can also be occupied by lead or tin cations (Pb^{2+} or Sn^{2+}) (or and blend of the two), which will be discussed in the next section.

2.3.2 Tuneable band gaps and lead-tin perovskites

By altering the composition of hybrid perovskites, the optoelectronic and structural properties can also be modified[47]. One such property of particular interest to this thesis is the modification of the band gap. The ability to create materials with different band gaps is of distinct importance when constructing multijunction photovoltaics which as discussed in the next section of this chapter. Early work by Noh *et al.* investigated the variation of the X_3 halide site by incorporating various ratios of I^- and Br^- cations[48]. This resulted in a range of materials with varying band gaps and increased humidity resistance. The inclusion of increasing amounts of bromide caused the band gap to increase from 1.58 eV to 2.28 eV[48]. Eperon *et al.* showed that the bandgap could also be modified by altering the composition of cations at the A-site[49]. Using the cations caesium (Cs^+), and formamidinium (FA^+) to replace methylammonium (MA^+), they were able to measure band gap shifts from 1.73 eV to a narrow band gap of 1.48 eV[49]. This was the first instance of the narrow gap absorber $FAPbI_3$, which among the neat Pb-based perovskites

produces the narrowest band gap. It wasn't until Noel *et al.* in 2014 reported a material with a significantly narrow band gap of 1.23 eV for an $MASnI_3$ material that used Sn^{2+} as the B-site cation in place of Pb^{2+} [50]. This was largely motivated by the known toxicity of lead and attempts to replace it by the less toxic Sn. Despite achieving an impressive V_{OC} of 0.88 V and a PCE of 6%, the same work reported a shorter diffusion length than the Pb-based materials, which they attributed to self-doping as Sn^{2+} rapidly oxidises to Sn^{4+} upon exposure to ambient atmosphere, causing the material to be heavily p-doped[50]. As a result of this thermodynamic instability, pure-Sn materials are incredibly hard to manufacture and require strict processing conditions, choice of solvent, and must be measured in an inert atmosphere[51]. By alloying the B-site with both Pb and Sn, the stability of the resulting perovskite is greatly enhanced due to an altered degradation mechanism, such that less thermodynamically favourable products are formed[52]. However, Lanzetta *et al.* showed that once degradation has started, even in mixed PbSn film, there is a cyclic degradation mechanism caused by free iodine (I_2) that causes rapid degradation in air. These properties make even PbSn materials extremely challenging to work with.

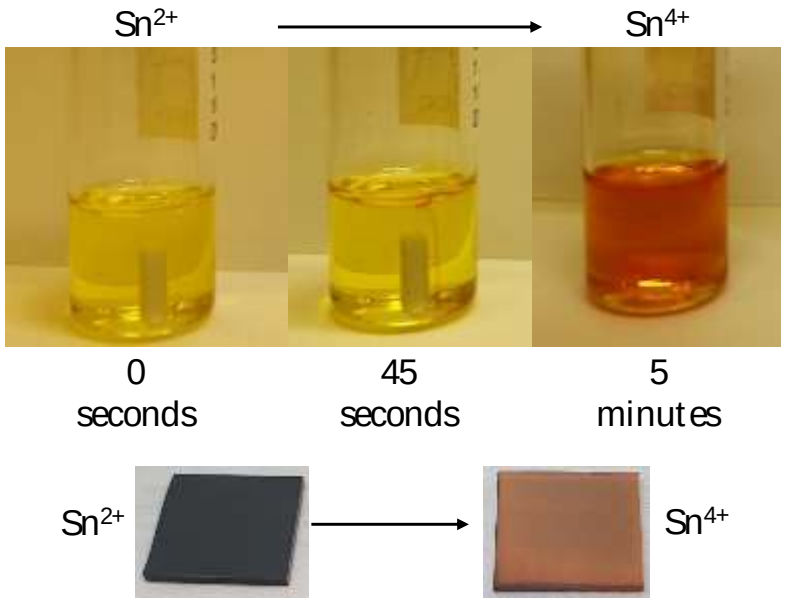

$$APb_{0.5}Sn_{0.5}I_3 + O_2 \rightarrow AI\ (g) + SnO_2 + PbI_2 + I_2(g)$$

Figure 2.14 – Top: An $FA_{0.83}Cs_{0.17}Pb_{0.5}Sn_{0.5}I_3$ ink exposed to air over 5 minutes. Middle: A film of $FA_{0.83}Cs_{0.17}Pb_{0.5}Sn_{0.5}I_3$ before and after 5 hours of air exposure. Bottom: The degradation pathway of Sn-containing perovskites. Mechanism adapted from[52].

Despite their instability when exposed to ambient conditions, a key property of this class of materials is that the band gap can be reduced even further than the neat-Sn and Pb materials. Im *et al.* achieved band gaps as low as 1.1 eV for a material with a PbSn ratio of 50:50 and displayed a band gap bowing effect as the ratio of Pb to Sn was altered[53]. The bowing effect shows a non-linear dependence of band gap with increasing amounts of Sn, where the band gap is wider in the pure Sn and Pb materials than it is for those of mixed composition. This band gap bowing effect has since been attributed by Goyal *et al.* to the energetic mismatch in *s* and *p* atomic orbitals[54] of Pb and

Sn whereby Pb *p*-orbitals contribute to the formation of the conduction band and Sn *s*-orbitals form the valence band, This cannot happen in the neat materials, as depicted in Figure 2.15.

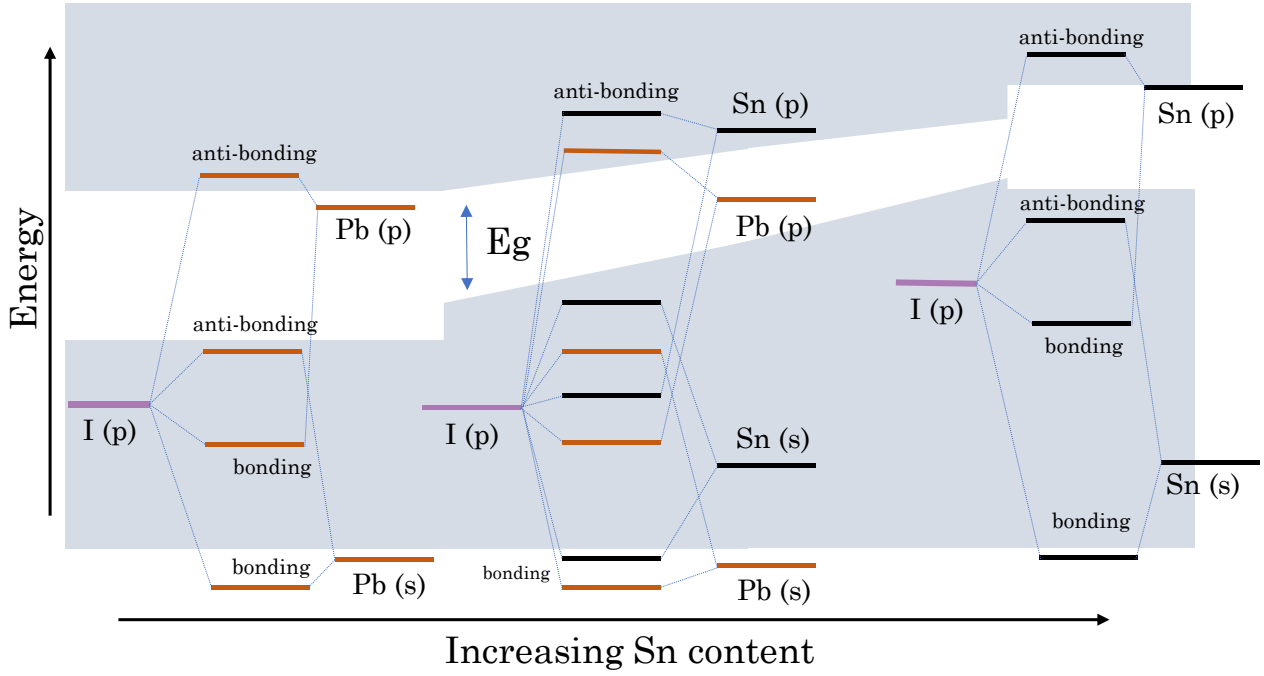

Figure 2.15 - The band gap bowing effect due to a mismatch in *s* and *p*-orbital energy levels across a range of Sn content, gradually widening again for pure Sn. Adapted from[54].

The highest performing absorbers utilising PbSn at the B-site also use MA at the A-site[55] However, Lietjens *et al.* showed that MA at the A-site has been shown to decrease stability further due to the volatility of MA, which causes it to outgas from the perovskite structure under normal working conditions rapidly diminishing performance[56]. They instead replaced MA with FACs at the A-site to give an $FA_{0.75}Cs_{0.25}Pb_{0.5}Sn_{0.5}I_3$ composition with enhanced stability in comparison to an MA containing blend. Despite the challenges

highlighted, high performing devices based on PbSn absorbers can be found throughout the literature[55,57,58], which has led to their successful deployment in multijunction solar cells[59–63].

2.3.3 Multijunction PV

The cost of silicon based photovoltaic (PV) cells contributes to less than 25% of the cost of an installed PV system. As the cost of installation and the balance of system (all equipment extra to the module) are depreciated over the life of the setup, this means that increasing cell efficiency has a direct impact on reducing the cost of power generation in terms of the levelised cost of electricity (LCOE) for the entire system over a typical 25 year lifetime[64,65]. Therefore, a direct route to providing large scale power generation, that can provide competitive LCOEs and displace existing power sources such as fossil fuels, is to increase cell efficiency per unit area[64]. After a brief discussion on efficiency limit to solar cells, multi junction PV will be discussed.

2.3.4 Limits to efficiency

Single junction solar cells are limited to a theoretical maximum efficiency as presented by Shockley and Queisser in 1961[66]. Their detailed balance limit predicted a maximum efficiency of ~34% for an ideal band gap of 1.34 eV. Several assumptions were made in this predictive model[67]:

1. All photons with $hf > E_g$ absorbed - whilst absorption can be improved by creating sufficiently thick absorbers (with long diffusion lengths L_D), losses from reflection and parasitic absorption from multiple layers must be

considered in working devices. There are also losses due to thermalisation as discussed previously in this chapter.

2. Each absorption event creates an electron hole-pair – this has been demonstrated and exceeded in quantum dot solar cells[68].

3. All carriers recombine radiatively – as previously discussed non-radiative recombination can occur at defects and interfaces and it is extremely difficulty to eliminate all non-radiative processes.

4. All carriers generated are extracted – this does not account for losses due to R_S and R_{SH} both described previously.

5. The Sun's spectrum is equal to that of a blackbody at 6000 K – while this may be a good approximation for radiation outside the Earth's atmosphere, at sea level the Sun's spectrum deviates from this due to absorption of photons by various gases in the atmosphere. Solar cells are commonly tested under light sources that simulate the air mass 1.5 (AM1.5) spectrum that approximates sunlight at sea level. Both AM0 (sunlight in space) and AM1.5 are shown in Figure 2.16.

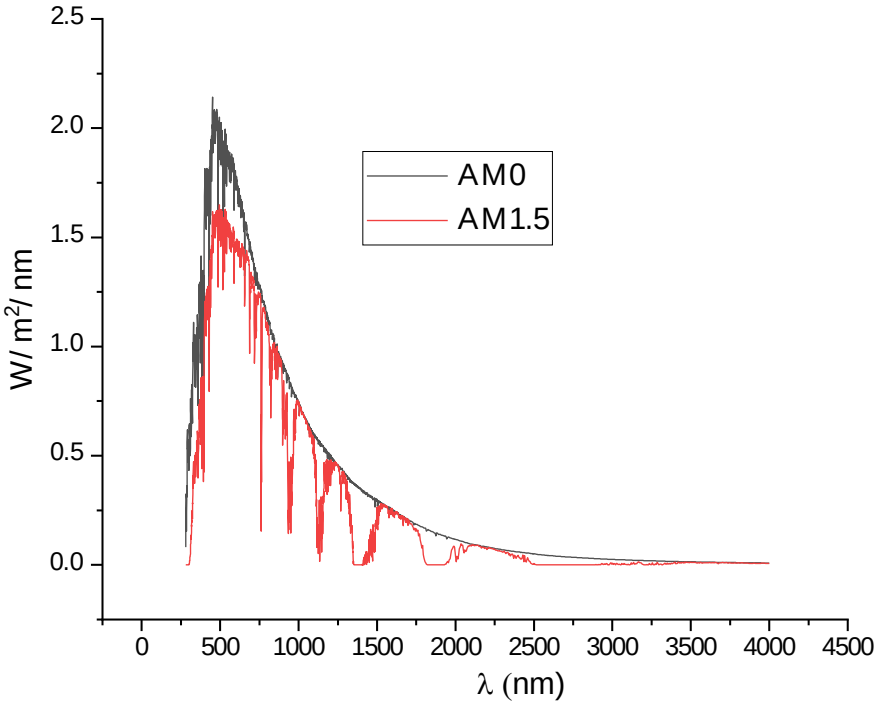

Figure 2.16 - The AM0 spectrum of sunlight outside the Earth's atmosphere (black) and the AM1.5 spectrum measured at sea level (red) and typically used for solar cell characterisation.

2.3.5 Overcoming the single junction limit

One approach to overcoming the theoretical maximum is to use multiple solar cells or absorbers stacked on top of one another. This simple concept allows for materials with two different band gaps to absorb photons of different frequencies. This reduces losses associated with thermalisation and allows the PCE to move beyond the value set by the detailed balance limit. When stacked in this way, cells are referred to as multijunction or tandem (for only two) solar cells.

Multijunction or tandem solar cells are usually constructed using two main types of architecture: a two terminal (2T), where layers in the stack are

fabricated directly on top of each other and connected via two electrical contacts as in a single junction, and four terminals (4T), where two single junctions are fabricated separately and then mechanically stacked on top of each other. Both are shown in Figure 2.17.

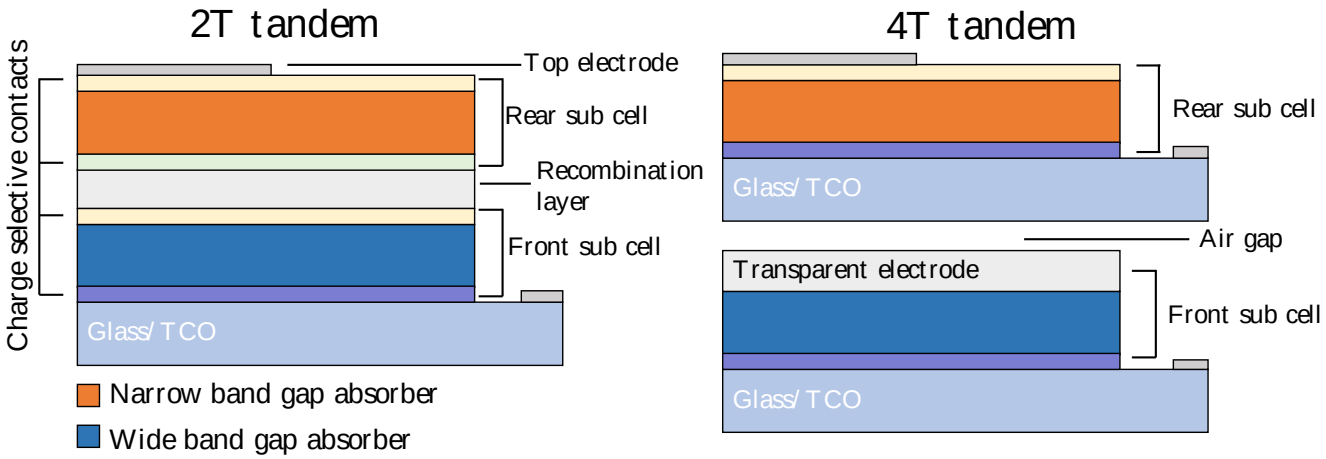

Figure 2.17 -Schematics of 2T and 4T tandem architecures.

Both types of architecture have their advantages and disadvantages. Four terminal architectures are easier to fabricate - two separate junctions are created and mechanically fixed together. This requires a transparent top electrode to be conductive enough to not incur series resistance (R_S) penalties and transparent enough to avoid optical losses. Four terminal cells require twice the transparent conductive oxide (TCO) substrates and terminals adding to the balance of systems. Two terminal-monolithic tandems are connected in series, requiring two contacts and fewer layers in order achieve complete fabrication. However, when fabricating from solution processed methods, they require the use of orthogonal solvents to ensure layers deposited sequentially do not dissolve the previous layer, which can be

challenging due to limited solvent choice. They also require current matching, where the current output from both sub-cells must match otherwise the tandem will be current limited by the sub-cell with the lower current output[26].

Tandem cells fabricated using III-V semiconductors, including gallium arsenide (GaAs) or indium gallium phosphide (InGaP), achieve very high efficiencies of over 40%[69]. However, these materials require expensive deposition methods such as molecular beam epitaxy (MBE), resulting in costs in excess of $20,000/m[70]. Perovskites by contrast can be made from inexpensive starting materials and by simple and cost-effective fabrications routes such as, roll-to-roll processing, ink-jet, slot-die, spin coating and vacuum deposition giving a high degree of flexibility[71].

A study by Hörantner *et al.* modelled monolithically stacked 2T cells, considering optical losses and location dependent data for the AM1.5 spectrum. They calculated the optimum band gaps required to deliver the highest efficiency, concluding that all perovskite tandems could reach efficiencies close to 32%[64]. To date, perovskite solar cells have achieved 2T tandem efficiencies of 26.4%[72].

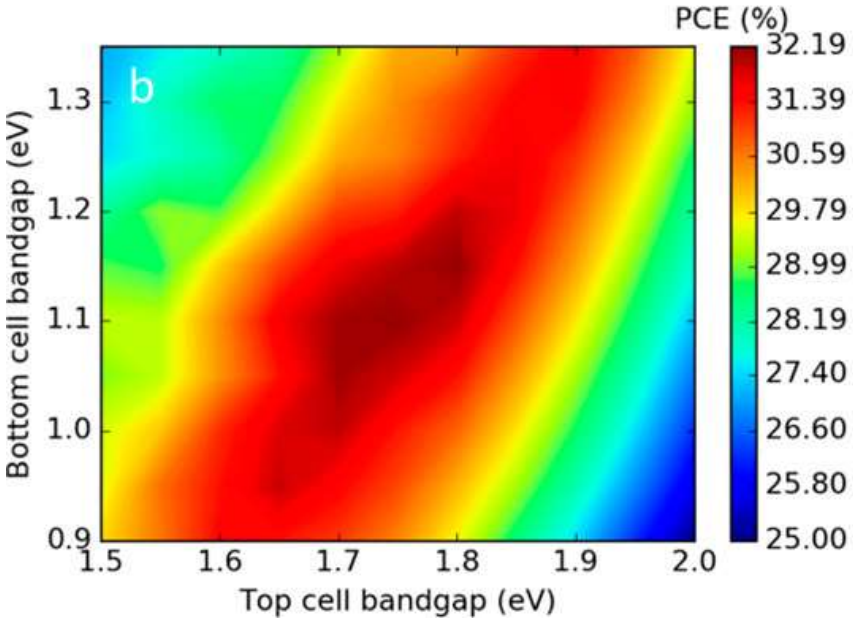

Figure 2.18 – Band gap matching and resulting efficiencies. Adapted with permission from[64].

Chapter 3

Experimental Methods

The following chapter details the experimental techniques used for the studies presented in this thesis. Including thin film and device fabrication, as well as the techniques used to characterise them.

3.1 Thin film and device fabrication

3.1 Spin coating

Most thin films in this thesis were prepared by spin coating using a Laurell Technologies spin coater and the anti-solvent or gas quenching method. The technique relies on depositing an ink or precursor solution onto a substrate then spinning the substrate a high speed in revolutions per minute (RPM). This pushes the liquid out from the centre forming a thin and highly uniform liquid film. For perovskite containing inks , whilst spinning a liquid termed the antisolvent, which is miscible with the precursor solvent but not the precursor solute[73], is dropped into the centre of the film. This causes supersaturation of the film and spontaneous nucleation of the perovskite layer. Further annealing helps the film to crystalise. For the gas quenching, the antisolvent is replaced by a stream of nitrogen. This method is widely used in perovskite research.

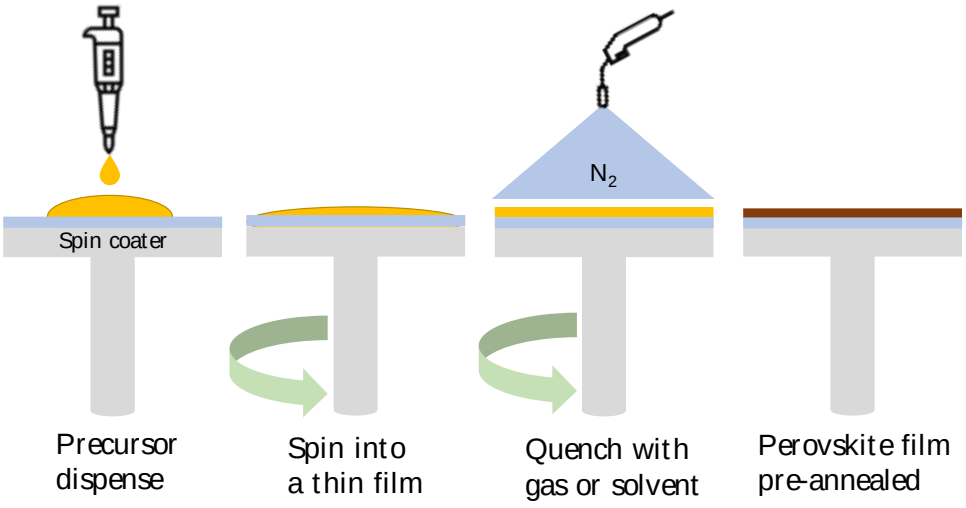

Figure 3.19 - a general schematic of the spin coating procedure used in this thesis.

3.1.1 Substrate preparation

All substrates whether bare glass, ITO, FTO, glass or quartz were cleaned and prepared via the same method unless otherwise stated. Substrates were cleaned by sonicating sequentially for 15 minutes in a beaker filled with Decon 90 detergent (1 % vol. in deionised (DI) water), DI water, Acetone and IPA followed by UV-Ozone (UVO) treatment for 15 minutes prior to deposition.

3.1.2 Perovskite precursor preparation

It is important to note that all stoichiometries and weights discussed are as calculated and nominal. Error associated with weighing should always be accounted for. In this section all weights were weighed to within 1 mg of error on the mass balance used (Kern ABJ 80-4NM)

$FA_{0.83}Cs_{0.17}Pb_{0.5}Sn_{0.5}I_3$ - Precursor solutions were prepared by dissolving 171.28 mg of formamidinium iodide (FAI, Greatcell solar) 53 mg of caesium iodide (CsI, Alfa Aesar), 276.61 mg of lead (II) iodide (PbI_2, Alfa Aesar, 99.999% mesh beads), 223.51 mg of tin (II) iodide (SnI_2, Alfa Aesar, 99.999% mesh beads), 9.4 mg of tin (II) fluoride (SnF_2, Sigma Aldrich,) corresponding to 10 mol% of the tin content in the precursor. These masses correspond to a 1.2 M solution in 1 mL of DMF:DMSO (4:1) which was kept constant throughout for both devices and film formation. Other concentrations were multiplications of these masses to achieve more concentrated solutions.

$FA_{0.83}Cs_{0.17}Pb_{0.5}Sn_{0.5}I_3$ with excess DMACl Solutions were prepared by dissolving 171.28 mg of formamidinium iodide (FAI, Greatcell solar) 53 mg of Caesium Iodide (CsI, Alfa Aesar), 276.61 mg of lead (II) iodide (PbI_2, Alfa Aesar, 99.999% mesh beads), 223.51 mg of tin (II) iodide (SnI_2, Alfa Aesar, 99.999% mesh beads), 9.4 mg of tin (II) fluoride (SnF_2, Sigma Aldrich,) corresponding to 10 mol% of the tin content in the precursor. These masses correspond to a 1.2 M solution in 1 mL of DMF only. This solution was stirred overnight then added to the correct amount of DMACl (dimethylammonium chloride, Sigma Aldrich 98%) powder and stirred for a further 2 hours before use.

3.1.3 DMACl dilutions

Two stock solutions of 100% DMACl added to 1.8 M of $FA_{0.83}Cs_{0.17}Pb_{0.5}Sn_{0.5}I_3$ and 0% DMACl (control solution) were made and mixed to prepare various concentrations of DMACl. DMACl is a power and DMF is the only solvent.

#	DMACl content (%)	0% solution(µL)	100% solution (µL)	Total (µL)
1	100	0	500	500
2	80	100	400	500
3	70	150	350	500
4	60	200	300	500
5	50	250	250	500
6	40	300	200	500
7	30	350	150	500
8	20	400	100	500
9	10	450	50	500
10	0	500	0	500

Table 3.1 - Serial dilutions to achieve a range of DMACl containing solutions.

3.1.4 Thiocyanate precursor solutions

Seven 3 mL 1.3 M stock solutions were prepared and stirred overnight. The following day 3 mL of each solution was added in a separate vial containing the amount of thiocyanate additive required for 3 mL solutions. These were stirred for a further 3 hours prior to use and then filtered with a 0.45 µm PTFE filter. The amount used was 5 mol% of the tin content (0.5) which equates to 2.5% of the thiocyanate (2.5% x 1 M).

Thiocyanate	2.5 % (1 M), 1mL (mg)	1.3 M, 1 mL (mg)

Pb(SCN)2	8.08	10.51
Sn(SCN)2	5.87	7.63
GUASCN	2.95	3.84
MASCN	2.25	2.93
FASCN	2.57	3.35
NH4SCN	1.90	2.47

Table 3.2 – The amount of thiocyanate additive used in each solution.

3.1.5 Perovskite deposition

Solvent quenched method 1.8M DMSO containing films – A schematic of the spin coating process is shown in **Figure 3.19**. Films were fabricated by spin coating and the anti-solvent quenching method.. In a nitrogen filled glovebox 100 μL of precursor solution was dynamically dispensed onto the substrate whilst spinning the substrate at 1000 rpm for a total of 10 s. At 10 s the substrate was then spun at 6000 rpm (4000 for 1.3M solutions) for a total of 59 seconds. At 20 seconds into the second step 200 μL of anisole was dispensed at a rate of 200 μL/s onto the middle of the spinning substrate which caused the perovskite film to turn from yellow to a light brown. The films were then immediately transferred to a hotplate and annealed at 120 °C for 10 minutes.

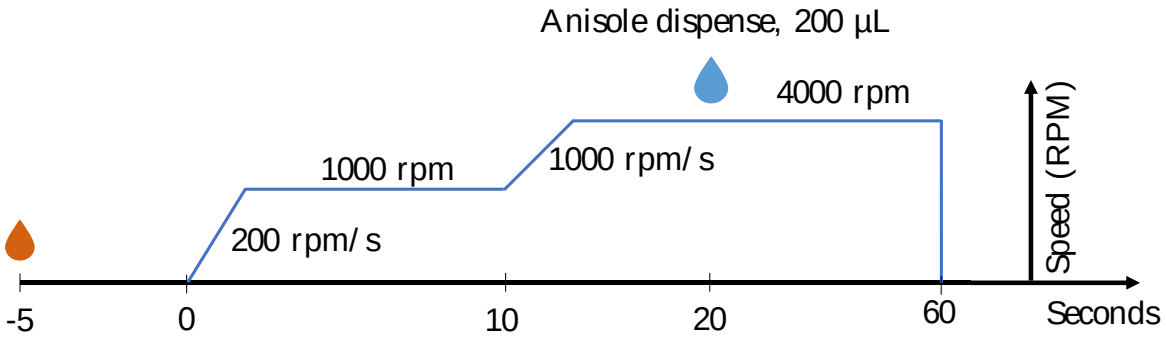

Figure 3.20 - A schematic of the general optimised spin coating recipe used in this thesis.

Gas quenched method 1.8M DMACl containing films – In a nitrogen filled glovebox 100 µL of precursor solution was statically dispensed onto the substrate before spinning the substrate at 1000 rpm for a total of 10 s. At 10 s the substrate was then spun at 6000 rpm (4000 for 1.3M solutions) for a total of 30 s. At 7 s into the second step a nitrogen positioned in the middle of the spinning substrate was opened fully releasing a stream of N_2 which caused the perovskite film to turn from yellow to a light colour depending on the composition. The films were then immediately transferred to a hotplate and annealed at 150 °C for 15 minutes.

Wide band gap absorber deposition (1.8 eV) - 1.2 M, $FA_{0.83}Cs_{0.17}Pb(I_{0.6}Br_{0.4})_3$ was prepared by weighing stoichiometric amounts of the precursor salts: CsI (Alfa Aesar), PbI_2 (TCI), FAI (Greatcell Solar), $PbBr_2$ (Alfa Aesar) and dissolved in DMF:DMSO (4:1 by volume). It was stirred for 1 hr and filtered (0.45 µm, PTFE) before use. 170 µl of the solution was dropped dynamically. The spin was conducted by 2 steps: 1000 rpm for 10s

(acc. 500 rpm/s) and 5000 rpm for 35s (acc. 1000 rpm/s). Then 325 µL of anisole was used for the solvent quenching at 5 seconds before end of the spin and then annealed for 100 °C for 30 mins.

3.1.6 Device architecture

All devices reported in this thesis were constructed using a *p-i-n* (sometimes referred to as "inverted") architecture with the general structure below

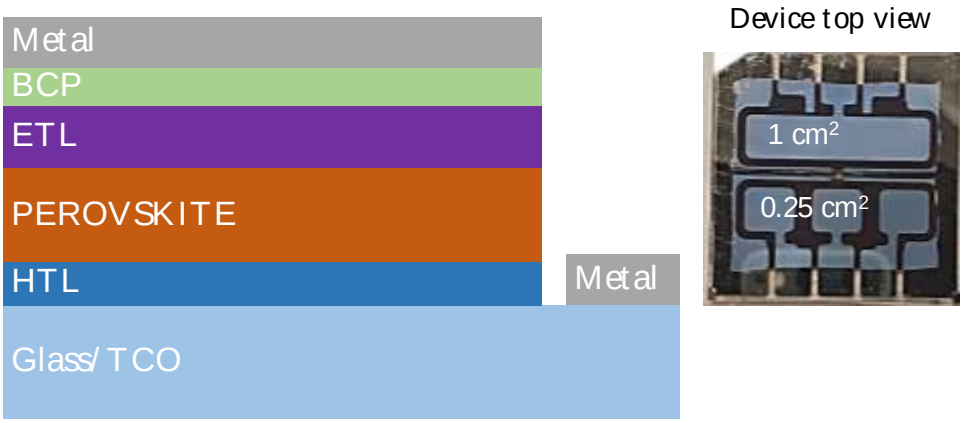

Figure 3.21 - a device stack with the *p-i-n* architecture used in this thesis and an example device.

3.1.7 Hole transporting layer (HTL) deposition

PEDOT:PSS - Poly(3,4-ethylenedioxythiophene) polystyrene sulfonate (Heraeus Clevios™, Al4083) diluted 1:2 by volume in methanol was filtered using a 0.45 µm glass microfiber (GMF) or polyvinylidene difluoride filter (PVDF). Directly after UVO treatment of a given substrate, 250 µL of the PEDOT:PSS solution was statically dispensed into the centre of the substrate then spin coated for 40 s at 4000 rpm with a 4000 (1 second) acceleration. After spin coating films were annealed at 150 °C for 10 minutes in ambient.

After annealing films were transferred into a nitrogen glovebox, films were heated on a hotplate at 100 °C for a further ~30 mins to remove any adsorbed moisture from ambient.

PTAA – Poly(triaryl amine),Poly[bis(4-phenyl)(2,4,6-trimethylphenyl)amine] (Flexink) solutions were prepared by dissolving 15 mg in 15 mL of toluene to give a 1 mg/mL concentration which was stirred overnight. This solution was filtered with a 0.2 μm PTFE filter once, prior to initial use.

Self-assembled monolayers (SAM) – All SAM molecules were purchased from Tokyo Chemical Industry apart from V1036 which was synthesised by the Department of Organic Chemistry, Kaunas University of Technology. 2-{3,6-bis[bis(4-methoxyphenyl)amino]-9H-carbazol-9-yl}ethyl)phosphonic acid (V1036), [2-(3,6-dimethoxy-9H-carbazol-9-yl)ethyl]phosphonic acid (MeO-2PACz), 2-(9H-carbazol-9-yl)ethyl]phosphonic acid (2PACz), (4-(3,6-Dimethyl-9H-carbazol-9-yl)butyl)phosphonic acid (Me4PACz) were all deposited via the same method. 10 mg of each powder was dissolved in 10 mL anhydrous ethanol (to give 10 mg/mL) in an N_2 glovebox and stirred overnight, this solution was filtered with a 0.22 μm PTFE filter. Each solution was then diluted down to give a concentration of 0.33 mg/mL. Substrates were cleaned via UVO for 30 minutes then transferred immediately to an N_2 glovebox. 250 μL of SAM solution was statically dispensed onto the clean substrate and then left to spread for 10 seconds and then spun for 30 s at 3000 rpm with a 600 (5 seconds) acceleration. Films were annealed at 100 °C for 10 minutes.

Al_2O_3 wetting layer – Aluminium oxide (nanoparticles, <50 nm particle size (DLS), 20 wt. % in isopropanol, Sigma Aldrich) this wetting layer was deposited on top of SAM coated substrates as they exhibit a very hydrophobic surface. The neat solution was diluted in IPA (1:150) then deposited by dynamically spin coating 80 µL of this solution onto SAM layers at 5000 rpm for 20 seconds. Subsequent films were not annealed.

3.1.8 Electron transporting layer deposition

PCBM - ([6,6]-Phenyl C61 butyric acid methyl ester, Solenne BV) solutions were prepared to a concentration of 20 mg/mL in a 3:1 mixture of chlorobenzene to dichlorobenzene. Once made solutions were left for at least 24 h at room temperature before filtering with a 0.2 µm PTFE filter.

C_{60} – (Alfa Aesar, sublimed, 99.9+%) Buckminsterfullerene or C_{60} layers were deposited by thermal sublimation under vacuum using an Angstrom engineering cluster system. Various thicknesses were deposited at a rate of 0.2 Å/s at pressures typically below 1 x 10^{-6} Torr.

BCP – (bathocuproine, Sigma Aldrich,) solutions prepared to a concentration of 0.5 mg/ml in isopropanol. Solutions were stirred overnight at 70 °C and then filtered a 0.2 µm PTFE filter prior to use. For vacuum deposited BCP a 5 nm layer of BCP was deposited using an Angstrom engineering cluster system at a rate of 0.2 Å/s at pressures typically below 1 x 10^{-7} mbar.

ALD-SnO_2 – SnO_2 films were deposited at 100 °C from a Tetrakis dimethylamino tin (TDMASn, Pegasus Chemicals) ALD source, using a

Picosun ALD system. Inert gas (Ar or N_2) was used as a carrier and purging gas. The vessels for TDMASn and DI water were maintained at 80 and 20 °C, respectively. 20 nm thick SnO2 films were achieved by 140 cycles consisting of 1.6s of TDMASn pulse/8.4s purging/1s of water pulse/9s of purging for a single cycle.

3.1.9 Passivation layers

All passivation's were deposited via dynamic spin coating 80 μL at 5000 rpm for 20 seconds and dispensing 5 seconds into the spin program.

FASCN – (formamidinium thiocyante, Greatcell Solar) passivation was prepared by dissolving 5 mg in 10 mL of IPA. and stirring overnight.

PEACl - (phenylethylammonium chloride, Sigma Aldrich) passivation was prepared by dissolving 5 mg in 10 mL of IPA and stirring overnight.

LiF – Lithium fluoride was deposited using a Kurt J. Lesker glovebox evaporator. A 1 nm layer of LiF was deposited at a rate of 0.2 Å/s at a pressure of 1 x 10^{-6} mbar.

Al_2O_3-np /EDA layer – (aluminium oxide nano particles, ethylene diamine) A solution of EDA (Sigma Aldrich) was prepared to a concentration of 5 mmol in IPA which was then was used to dilute a stock solution of Al_2O_3 nano particles in IPA (Sigma Aldrich, nanoparticles, <50 nm particle size (DLS), 20 wt. % in isopropanol) to a dilution factor of 50:1 (EDA stock:Al_2O_3 stock)

3.1.10 Electrode deposition

All electrodes for devices were deposited using a shadow mask to give an electrode pattern complimentary to our solar simulator. The pattern resulted in 4 pixels per substrate each with an active area of 0.25 cm^2 for 3 of the pixels and 1 cm^2 for 1 pixel. A Kurt J. Lesker Nano 36 evaporator was used to deposit silver (Ag), gold (Au) and chromium/gold (Cr/Au) electrodes. An example device can be seen in **Figure 3.21** - a device stack with the *p-i-n* architecture used in this thesis and an example device Figure 3.21.

3.1.11 Encapsulation

Encapsulation of samples was carried out by first removing all perovskite material outside the perimeter of the glass cover slips used so that the glue was in contact with glass. A UV curable epoxy (Dymax OP29) was used and a glass coverslip (AMG, Korea). Curing time was approximately 5 minutes.

3.2 Characterisation

3.2.1 Current density-voltage characterisation

Devices were tested under simulated AM1.5 solar irradiation at 100 mW/cm^2 irradiance with a Wavelabs Sinus-220 (light-emitting diode array) solar simulator. The Wavelabs simulator was calibrated with an Si reference cell (Fraunhofer ISE). Current -Voltage characterisation was performed in air using a Keithley 2400 source meter, with a scan rate of 0.3 V/s.

3.2.2 Ambient stability testing

Devices for ambient stability tests were placed vertically into a laser cut jig which was placed inside a re-sealable plastic box made by Lock and Lock. At the bottom of the box was a ~5 mm layer of silica desiccant from VWR (Silica gel, granules, Chameleon® C 2 - 6 mm drying agent). The temperature and humidity were tracked using a Blue Maestro, Tempo disc blue tooth sensor. Devices were removed from the box and measured in ambient conditions for ~1 hour per measurement.

3.2.2 1D-XRD

X-ray diffraction patterns were obtained using a Panalytical X'Pert Pro X-ray diffractometer, with a copper K-α source at (λ = 1.54 Å). The generator setting was 40 kV and 40 mA. Scans were 45 minutes each.

3.2.4 2D – XRD

2D-XRD patterns were conducted in nitrogen at room temperature using a Rigaku SmartLab X-ray diffractometer with a copper K-α source (λ = 1.54 Å) and a HyPix-3000 2D hybrid pixel array detector, operated at 40 kV.

3.2.5 GIWAXS

In situ grazing-incidence wide-angle X-ray scattering data was acquired at the I07 undulator beamline at Diamond Light Source. Solutions were deposited using an in-situ blade coater contained in an N2 environment incorporating a syringe driver, coating surface, motorised blade, integrated hotplate and an N2 outlet directed at the sample acting as an air knife. Prior

to data acquisition, solutions were deposited onto cleaned glass substrates, and coated with a blade with a shim height of 100 um and coating speed of 9 mms-1, with gas quenching applied continuously from 30 s. Monochromatic X-rays with energy 10 keV were incident on the sample at a grazing angle of 1°, with scattering collected by a Pilatus 2M (DECTRIS) hybrid photon-counting detector at a distance of 365 mm, calibrated using an LaB6 standard. 2D detector images were acquired every 0.2 s. Data reduction was performed using scripts based on the pyFAI and pygix libraries[74].

3.2.6 SEM

All images were taken using an FEI Quanta 600 microscope with a spot size of 3, a working distance of 10-15 mm and an acceleration voltage of 5 kV. Samples were prepared on conductive substrate and held in place with conductive carbon tape.

3.2.7 Time-Resolved Photoluminescence Measurements (TRPL)

Time-correlated single photon counting measurements were carried out using a 398 nm centre wavelength laser (PicoHarp, LDH-D-C-405M) to photoexcite the perovskite thin films with pulsed excitation mode with a repetition rate of 0.125 MHz. The samples were excited at two fluences of 1300 nJ/cm2 and 150 nJ/cm2. The photoluminescence was collected using a Princeton Instruments SP-2558 monochromator, with a photon-counting detector (PDM series from MPD). Timing is controlled electronically using a PicoHarp300

event timer. PL decays were measured at the peak wavelengths of the PL spectra. Measurements were carried out in ambient air; however, the samples were encapsulated. TRPL. To calculate the average decay lifetime a least-squares fit was carried out on the lowest-fluence PL decays using the stretched exponential equation,

$$I(t) = I_0 e^{-\left(\frac{t}{\tau_{char}}\right)^{\beta}} \tag{3.1}$$

Where *I(t)* is the PL intensity a time t, I_0 is the initial PL intensity and β is the stretching factor. The average lifetime was then calculated from,

$$\tau_{av} = \left(\frac{\tau_{char}}{\beta}\right) \Gamma\left(\frac{1}{\beta}\right) \tag{3.2}$$

Where τ_{av} is the average decay lifetime Γ is the gamma function. The stretched exponential function has been used in throughout the literature to fit TRPL decays[49,75].

3.2.8 Photoluminescence quantum efficiency (PLQE)

Samples were suspended inside an integrating sphere and illuminated via 532 nm CW laser (ThorLabs DJ532-10) coupled to an optical fibre feedthrough the laser spot size on the sample was 0.15 cm2. The laser power was adjusted to 1 sun equivalent for a 1.25 eV band gap based on values publish by Kirchartz *et al.*[76] which was 87.5 mW/cm2. A second fibre was used for light collection from the sphere which connected to a Maya2000 Pro

spectrometer. The determination of PLQE found via the method published by DeMello et al.[77] and was computed by a python program written by Dr Bernard Wenger, University of Oxford. A diagram for the PLQE setup is shown in Figure 3.22.

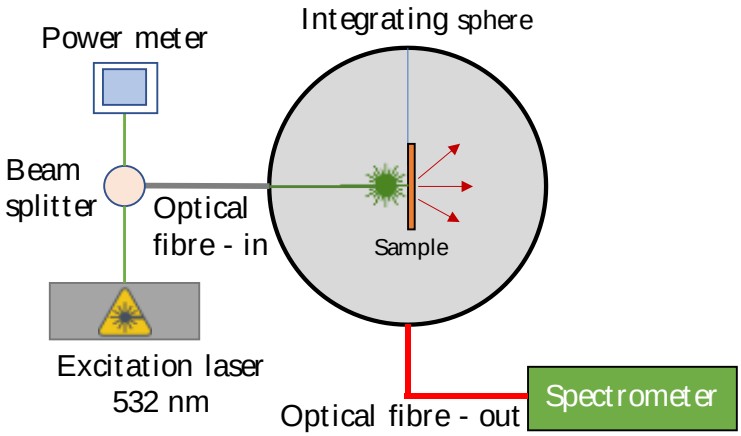

Figure 3.22 - A diagram of the PLQE setup used to collect PLQE data in this thesis.

3.2.9 External Quantum Efficiency (EQE)

External quantum efficiency measurements were performed using a custom-built system. The monochromatic illumination source was provided using a 250 W halogen lamp and monochromator (Princeton Instruments Acton SP2150, with FA2448 filter wheel), which was chopped (Thorlabs MC2000B-EC) at 280 Hz and focused to a spot size on the sample that was smaller than the pixel defined by the evaporated rear electrode. The pixel was selected using a home-built multiplexer, and its AC current signal due to the chopped monochromatic illumination was converted to a voltage using a 50 Ω resistor. The amplitude of this voltage signal was measured using a lock-in amplifier

(Stanford Research Systems SR830). The absolute value of EQE was calculated based on the ratio of this voltage signal to that of a signal generated by a reference Si photodiode of known EQE (Newport 818-UV/DB or Thorlabs FDS100-CAL) under the same illumination conditions as the test device.

3.2.10 Luminescence Imaging

The spatially resolved data were taken using an in house-built photoluminescence measurement setup as detailed in the recent publication by Akash Dasgupta, University of Oxford - *Visualizing Macroscopic Inhomogeneities in Perovskite Solar Cells*[78].

3.2.11 Spectral mismatch

To accurately measure a solar cell spectral mismatch of the solar similar and the AM1.5 spectrum must be accounted for[79]. Due to the nature of the light sources used in research and testing to approximate the Sun's spectrum (AM1.5) , spikes and dips in the spectrum can arise which cause the spectrum of the simulator to deviate from AM1.5. The spectral mismatch is also dependant on the band gap of the material within the device being tested. The spectral mismatch for the Wavelabs Sinus-220 light source and the bandgap for the material in this study was calculated and found to be negligible meaning the testing setup extremely accurate.

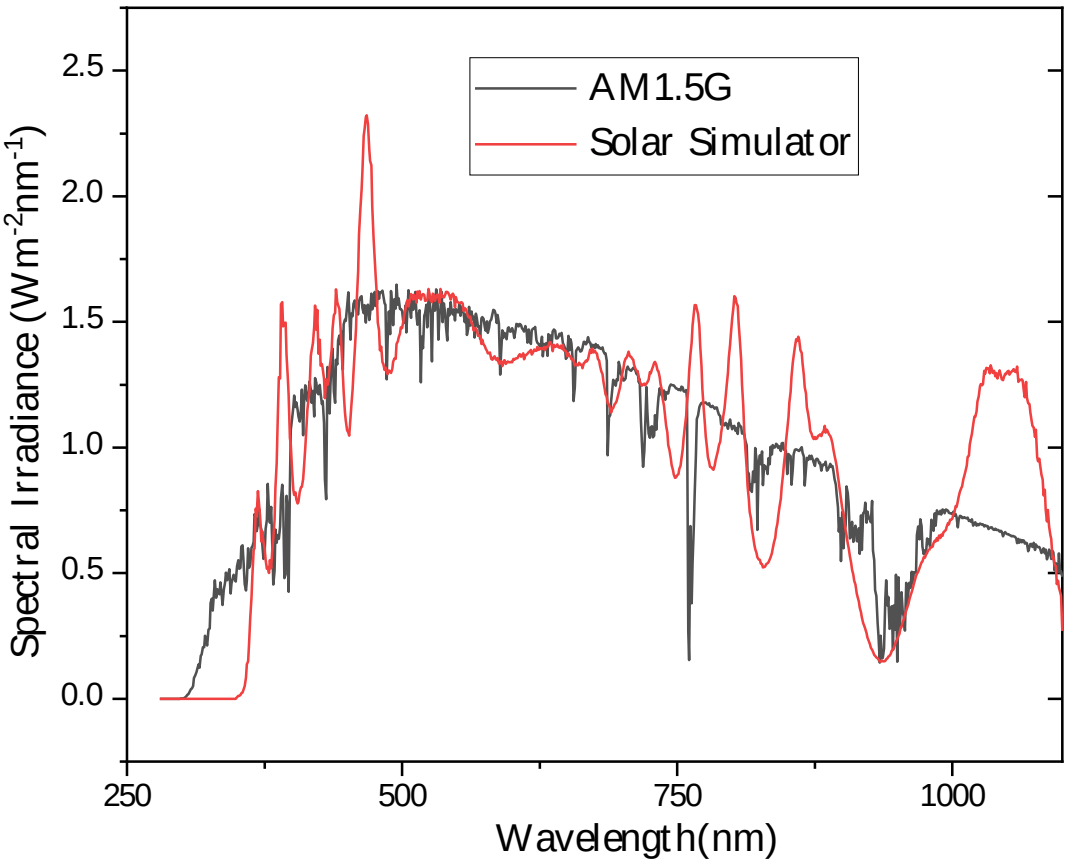

Figure 3.23 – Showing the spectral irradiance versus wavelength of AM1.5 and the Wavelabs solar simulator used to test the solar cells in this thesis.

Chapter 4.

Bulk and Interface Engineering of Narrow Band Gap Perovskite Solar Absorbers

In this chapter various strategies to improve the optoelectronic properties of an $FA_{0.83}Cs_{0.17}Pb_{0.5}Sn_{0.5}I_3$ absorber are investigated including, passivation of the bulk absorber and interfaces, and how the charge selective contacts influence non-radiative losses. The bulk passivation strategy utilises a range of popular salts that all have the common thiocyanate anion (SCN^-). It is shown that all the thiocyanates studied improve the grain size, morphology and enhance the radiative efficiency and carrier lifetimes for $FA_{0.83}Cs_{0.17}Pb_{0.5}Sn_{0.5}I_3$ thin films but at high loadings introduce unfavourable phases into the films which hinder device performance. Further into the chapter it is found through photoluminescence quantum efficiency (PLQE) measurements, that significant non-radiative recombination occurs at both interfaces between an $FA_{0.83}Cs_{0.17}Pb_{0.5}Sn_{0.5}I_3$ absorber from common charge selective layers. Finally, a strategy to passivate the interfaces is investigated via PLQE and deployed into photovoltaic devices resulting in an enhanced performance.

4.1 Introduction

Defects in metal halide perovskites can have dramatic effects on the performance of devices and their resultant stability[80]. Being able to passivate these defects, whether physical or electronic, is incredibly important to maximise solar cell performance and stability and remains an important challenge to commercialisation. Many of these defects can occur in the bulk, at grain boundaries, and at the interface with charge selective layers, reducing photoluminescence quantum efficiency (PLQE) and carrier diffusion lengths[81]. Much focus in the perovskite field has been on how to maximise the bulk optoelectronic properties of lead-based (Pb) perovskite absorbers[82] and the losses associated with charge selective layers[83–85] but comparatively, lead-tin (PbSn) perovskites have received negligible attention. Whilst there has been some effort to use various additives for formamidinium/methylammonium (FAMA) lead-tin perovskite blends[62,86–88], at present, there have been no studies conducted on formamidinium/caesium (FACs) based lead-tin materials. The work presented in this chapter investigates both bulk recombination and interfacial recombination via stepwise thin film engineering. For the bulk passivation study, several thiocyanate salts, used frequently in perovskite literature, are deployed including a previously unreported $Sn(SCN)_2$. Many have been used in high-performing Pb and PbSn devices[57,60,61,89] however, there have been no side-by-side comparisons of these additives, and only lead thiocyanate $(PbSCN)_2$ has been used for lead-tin devices with FACs as the A-site cation blend[89,90]. This

range of additives was chosen to assess whether the cation plays a role in performance enhancement. A series of films were fabricated on glass to minimise the effects of interface recombination and were analysed using PLQE, PL imaging and TRPL. In this study 5 mol % of each thiocyanate, relative to the Sn content, is used as the additive. This is less than what is typically used in literature and was chosen to observe the effect on the final absorber without the need for rigorous optimisation. The second half of this chapter utilises PLQE to probe the non-radiative recombination occurring at the interfaces of the $FA_{0.83}Cs_{0.17}Pb_{0.5}Sn_{0.5}I_3$ material in contact with charge selective layers. The choice of transport layers for PbSn, *p-i-n* devices is mainly limited to PEDOT:PSS as the hole transporting material and Phenyl-C61-butyric acid methyl ester (PCBM) or fullerene (C_{60}) as the electron transporting materials. To date PEDOT:PSS still dominates the literature for PbSn devices although many publications cite the need to move away from it due to unfavourable acidic properties, lack of ambient stability, and inferior long term device stability[91]. Whilst there have been countless studies on interfacial losses for Pb-only devices[85,92–95], there has been very little focus on this for PbSn devices. In this chapter several hole transporting layers (HTL) and electron transporting layers (ETL) materials in contact with an $FA_{0.83}Cs_{0.17}Pb_{0.5}Sn_{0.5}I_3$ absorber are studied via PLQE and in devices. Following this, there is a brief study on the effect inserting a passivation layer at the ETL interface. It is found that PEDOT:PSS introduces a high degree of non-radiative recombination such that PLQE cannot be measured. Poly[bis(4-

phenyl)(2,4,6-trimethylphenyl)amine (PTAA) and several popular self-assembled monolayer (SAM) type hole transporters[96–99] are able to preserve the PLQE of the neat absorber on glass and reduce the amount of non-radiative recombination at this interface. However, they are unable to be successfully deployed into devices due to poor charge extraction. It is also found that PCBM and C_{60} introduce significant losses to the perovskite indicating issues at both interfaces and that using an appropriate passivation can mitigate this.

4.2 Results and Discussion

4.2.1 Bulk passivation via thiocyanates

Initially, the morphology of SCN modified films was analysed with scanning electron microscopy (SEM). The formation of compact, pinhole free absorber layers is essential for fabricating functional devices[100]. A 5 mol % excess relative to the Sn content of the films was used for each SCN additive.

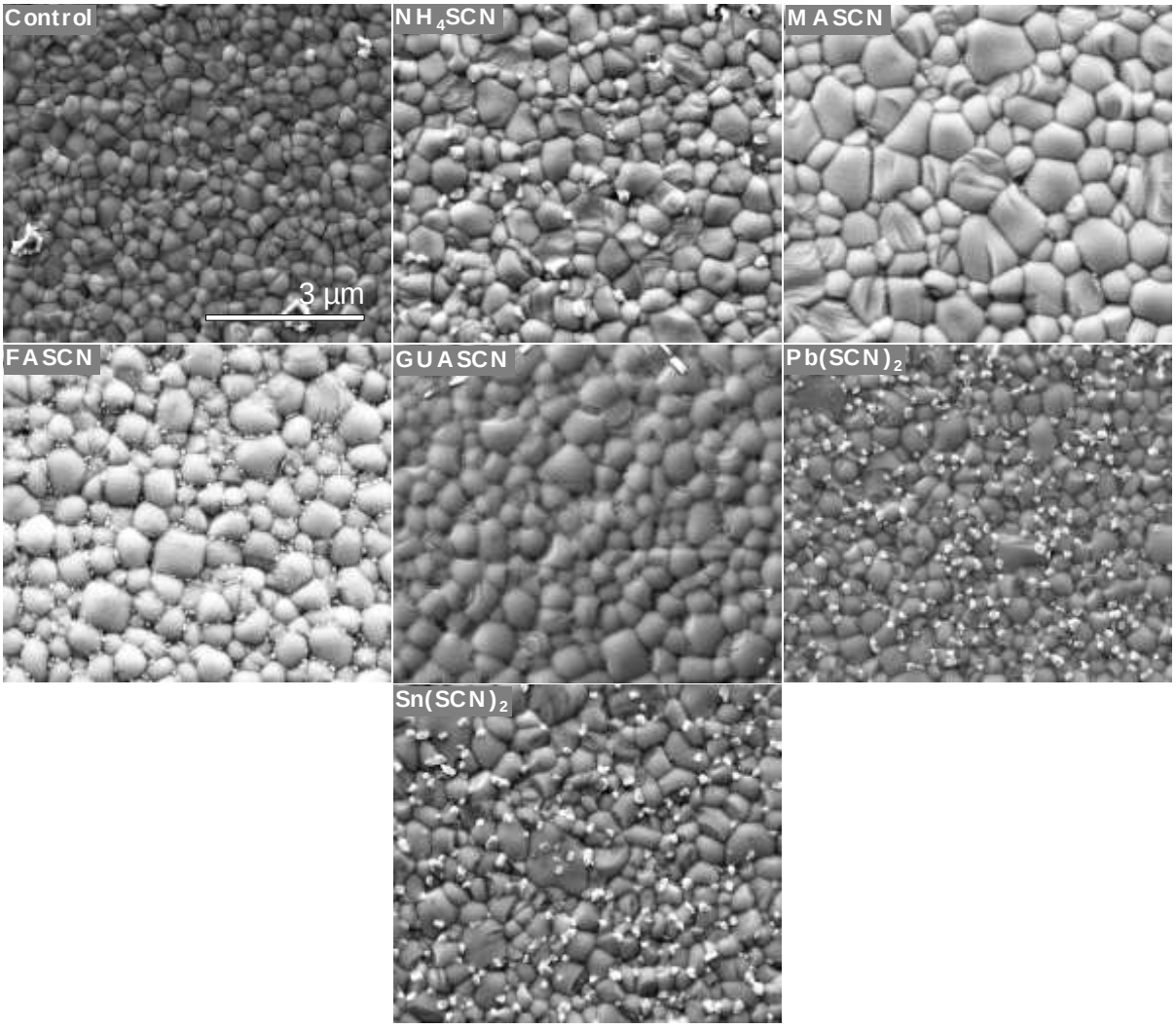

Figure 4.24 – SEM images showing that the addition of all SCN additives enhances the apparent grain size of resulting films. Those with organic cations show a large

increase in apparent average grain size with methylammonium thiocyanate (MASCN) sample showing the greatest increase going from an average grain size of 289 nm in the control film to 657 nm. A summary for all average grain sizes is given in Table 4.3. Thiocyanates containing the metal cations Pb and Sn show a more modest enhancement, signifying the importance of the organic cation's role in increasing grain size in these polycrystalline films. Scale bars are 3 μm. Additionally, GUA and FA represent guanidinium and formamidinium, respectively. The very small bright white particles seen on each film are assigned to SnF_2.

SEM analysis whilst excellent for determining morphology gives only apparent grain size due to the fact only the top surface of the sample is being imaged. However, apparent increase in grain size is consistent with literature assessments[61,101]. This is perhaps why most high performing devices use an organic thiocyanate salts instead of those containing metals[57,61,102]. It is postulated that the more volatile organic compounds can complex with solutes in the precursor inks and evaporate during annealing slowing down crystallisation in the process[101]. The heavier metal cations cannot evaporate and may act as nucleation centres, causing more rapid crystallisation. Various studies have shown grain boundaries to be the sites of defects and dangling bonds that can introduce non-radiative recombination (reducing open circuit voltage) and increase hysteresis.[103,104] Grain boundaries have also been shown as sites of ingress for moisture and oxygen, therefore accelerating degradation[105–107]. By increasing the apparent average grain size of the film, the optoelectronic properties of resulting films and the long-term operation of resultant devices should be improved. Based on the results from

SEM analysis alone, thiocyanates with organic cations show promise for $FA_{0.83}Cs_{0.17}Pb_{0.5}Sn_{0.5}I_3$ based absorbers.

Sample	Average grain size (nm)
Control	289
NH_4SCN	440
MASCN	657
FASCN	579
GUASCN	537
$Pb(SCN)_2$	399
$Sn(SCN)_2$	362

Table 4.3 – Calculated average grain sizes for each thin film. Average grain sizes were calculated by drawing 3 lines of equal length over each image, counting the frequency of grain boundaries that bisect the lines, then averaging the resulting frequencies and converting into nanometres using the length scale with Image J image analyser[108].

Having shown drastic grain size enhancement, the PLQE of a set of companion films were measured as shown in Figure 4.25. To maximise efficiency and operate closer to a device's theoretical limit, it must be able to extract carriers efficiently[109]. At open circuit, which is the case for films fabricated on glass, carriers cannot be extracted by an external circuit, as in an operational solar cell in the power generating quadrant. Therefore, carriers must recombine via radiative recombination (emitting a photon) or non-radiative recombination via phonon emission where energy is lost as heat. The latter pathway results in a loss of open-circuit voltage under illumination from an increased dark injection current in working devices. As mentioned in Chapter 2, this can be directly measured by PLQE, which is the ratio of emitted and absorbed photon flux or, equivalently, the ratio between the total radiative recombination current density (J_{rad}) and the generation current density (J_G) described by the following equation,

$$PLQE = \frac{\varphi_E}{\varphi_A} = \frac{J_{rad}}{J_G} = \frac{J_{rad}}{J_{rad} + J_{non-rad}} \quad (4.1)$$

where φ_E and φ_A are the flux of emitted and abosrbed photons, respectively. J_{rad} and $J_{non\text{-}rad}$ are the radiative and non-radiative current densities, repsectively. When calculating quasi-Fermi level splitting (QFLS) for a working device, J_G can be subsituted by J_{SC} as will be shown. This assumes that at J_{SC} conditions, all generated charge carriers are extracted.

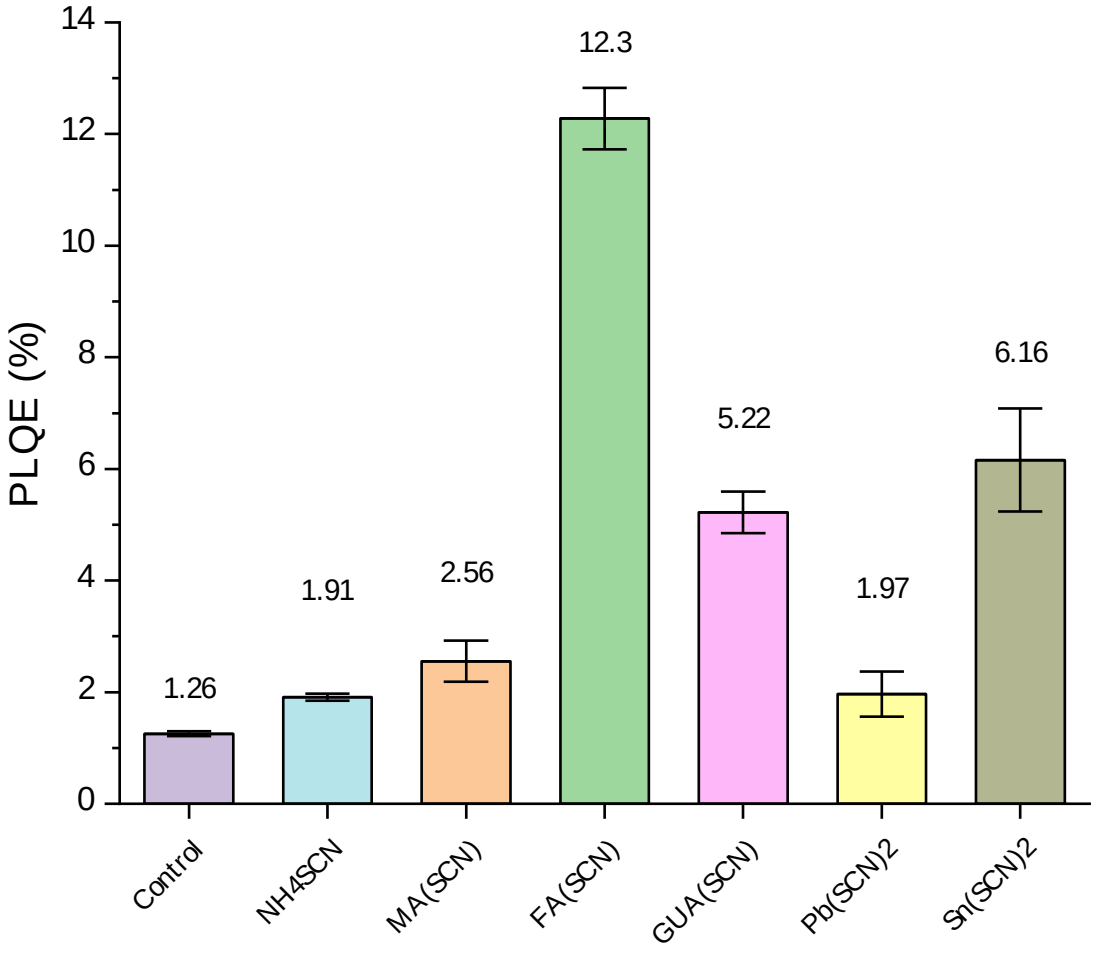

Figure 4.25 - The measured PLQE of 2 companion films containing various thiocyanate additives. Samples were illuminated with a 532 nm laser with a power density equal to 1 sun for a band gap of 1.25 eV. More details on the PLQE setup and measurements can be found in Chapter 3.

The spectra from which the values were calculated are shown in Figure 4.26.

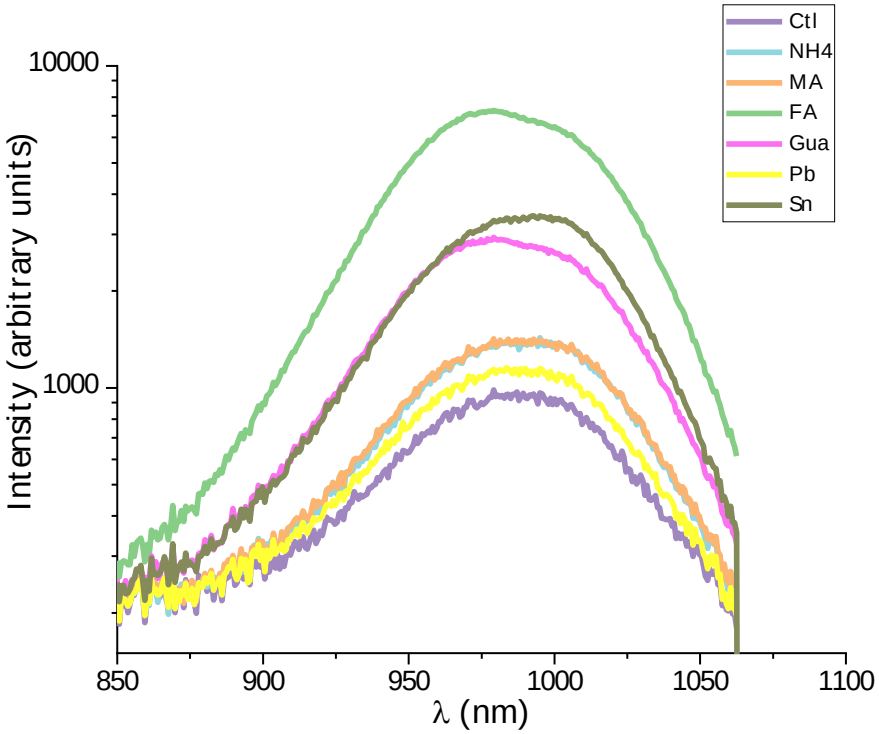

Figure 4.26 - The photoluminescence spectra for all samples in the study. Ctl represents the control film.

After measuring the PLQE, the resultant QFLS for each sample was calculated by using the following relationship,

$$QFLS = kT\ln\left(\mathrm{PLQE}\frac{Jsc}{Jo,rad}\right) \tag{4.2}$$

where QFLS is the quasi-fermi level splitting (hence maximum achievable *Voc* for the given material as discussed in Chapter 2, k is the Boltzmann constant, T the temperature, J_{SC} the short-circuit current, $J_{0,rad}$ the dark radiative recombination current, and PLQE the measured photoluminescence quantum yield. To calculate the QFLS, J_{SC} and $J_{0,rad}$ must be calculated using the following expressions[85],

$$J_{SC} = q \int EQE(E)_{\varphi AM1.5}(E)dE \tag{4.3}$$

and

$$J_{0,rad} = q \int EQE_{PV}(E)\varphi_{BB}(E)dE \tag{4.4}$$

where φ_{BB} is the black body spectrum at room temperature. From equation 4.3, J_{Sc} is given by calculating the overlap integral of the AM1.5 photon flux ($\varphi_{AM1.5}$) with the measured external quantum efficiency (EQE) for a control device. This becomes useful in approximating the maximum QFLS for a real solar cell. By measuring the EQE of a control PbSn device and using equation 3, $J_{0,rad}$ was calculated to be 1.03 x10^{-14} mA/cm^2. The equivalent J_{SC} for the same cell as measured was 26.3 mA/cm^2. Using these values, the PLQE measured for each sample and equation 4.2, the QFLS was calculated for each film as shown in Table 4.4. Table 4.4 shows that although $Pb(SCN)_2$ has a negligible effect on PLQE, all other thiocyanate additives enhance the PLQE and therefore reduce non-radiative recombination within the material. Using equation 4.2 a QFLS of 0.98 eV can be calculated using 100% PLQE, representing the maximum PLQE and QFLS the material can achieve. Interestingly the FASCN sample shows a difference of only 0.05 eV from this limit. If this could be extracted as V_{OC}, it would represent the highest reported V_{OC} for PbSn devices at the time of writing[57].

Sample	PLQE (%)	QFLS (eV)
Control	1.3	0.87
NH_4SCN	1.97	0.88
MASCN	2.19	0.88
FASCN	12.83	0.93
GUASCN	4.85	0.90
$Pb(SCN)_2$	1.56	0.87
$Sn(SCN)_2$	5.24	0.90

Table 4.4 – PLQE and corresponding calculated QFLS values for all films.

Table 4.4 and Figure 4.25 show that all thiocyanate additives reduce non-radiative recombination of the neat $FA_{0.83}Cs_{0.17}Pb_{0.5}Sn_{0.5}I_3$ absorber material (with FASCN, GUASCN and $Sn(SCN)_2$ showing a dramatic decrease), increasing the QFLS and resultant *Voc* in photovoltaic devices.

Whilst PLQE is an important parameter to assess material quality, an equally important parameter is diffusion length. Diffusion length gives the average length for which a charge-carrier can travel in a semiconductor before it recombines[110]. It is especially important in PbSn, narrow band gap absorbers due to the drop off in absorption coefficient in the near-infrared

region (NIR)[62]. To maximise absorption, and therefore current density, in a device, the thickness of the absorber layer must be increased. However, if the diffusion length of a charge carrier is shorter than the thickness of the absorber layer, charges will recombine before they can be extracted, resulting in a loss of current at the maximum power point of an operating device, counteracting the gain from increased absorption. To assess the impact of the thiocyanate additives on the diffusion length within each material, TRPL measurements were conducted. This was performed on the same set of films used for PLQE measurements. Stretched exponential functions were fitted to the resulting data to extract lifetimes (τ) by Robert D. Oliver, University of Oxford.

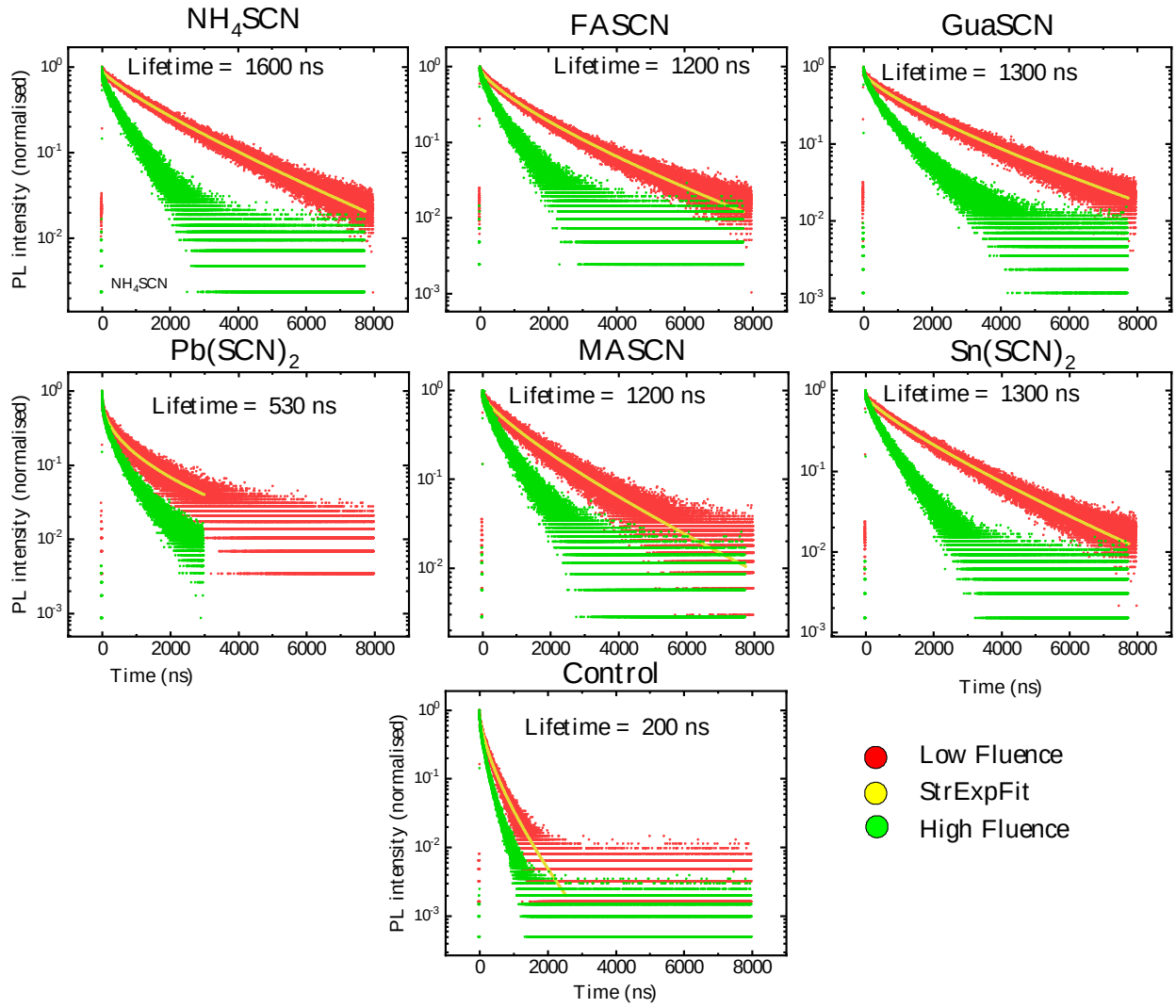

Figure 4.27 - Time resolved photoluminescence plots of the control and thiocyanate modified films. Plots are labelled individually. Measurements and stretched exponential fits to find the lifetime (τ) for each film were performed by Robert D. Oliver, University of Oxford. Further experimental details can be found in Chapter 3.

To calculate the diffusion length from the lifetime of each film the following relationship was used,

$$L_D = \sqrt{D\tau} \tag{4.5}$$

where L_D is the diffusion length (m), D the diffusivity (m^2/s) and τ the lifetime (s) extracted from TRPL. First, the diffusivity was calculated by using the Einstein relationship,

$$D = \frac{\mu.kT}{q} \tag{4.6}$$

where μ is the mobility (m^2/Vs) and q is the electronic charge. The mobility of a control film was measured by Alexander Ulatowski, University of Oxford to be 27 cm^2/Vs via terahertz conductivity[111]. Under the assumption that the mobility does not change between these samples, the diffusion lengths were calculated as shown in Table 4.5.

Sample	**μ (cm^2/Vs)**	**D (cm^2/s)**	**τ (ns)**	**L_D (μm)**
Control	27	0.69	200	3.74
NH4SCN	-	0.69	1600	10.6
MASCN	-	0.69	1200	9.15
FASCN	-	0.69	1200	9.15
GUASCN	-	0.69	1300	9.52
Pb(SCN)2	-	0.69	530	6.08
Sn(SCN)2	-	0.69	1300	9.51

Table 4.5 – Mobility, diffusivity, and calculated diffusion length for each sample.

Table 4.5 shows that the addition of all the thiocyanate salts vastly improves the charge-carrier diffusion length within the $FA_{0.83}Cs_{0.17}Pb_{0.5}Sn_{0.5}I_3$ thin films. The average thickness for these films was determined to be 369 nm. At this thickness charge collection should not be an issue, even in the control samples. It is important to note that mobility may change between samples and may deviate from the control value due to the influence of additives but it is expected to increase due to the increase in measured carrier lifetime, hence this would represent a worst-case scenario. A summary of the measured parameters is presented in Table 4.6. It is clear that samples with a larger apparent grain size, compared to the control, have a longer calculated diffusion length in general but this is not a linear trend as can be seen with the ammonium thiocyanate additive.

Sample	Average grain size (nm	PLQE (%)	L_D (μm)
Control	289	1.3	3.74
NH4SCN	440	1.97	10.6
MASCN	657	2.19	9.15
FASCN	579	12.83	9.15
GUASCN	537	4.85	9.52
Pb(SCN)2	399	1.56	6.08
Sn(SCN)2	362	5.24	9.51

Table 4.6 – Summarising all of the measurements taken on each film.

4.2.2 Assessing film uniformity

Another important aspect in fabricating thin film devices, especially in the *p- i-n* architecture, is the ability to form a smooth, homogenous film of every layer over areas compatible with research-scale device areas (0.25 cm^2 and 1 cm^2). Many layers in a device stack are amorphous, organic molecules or polymers comprised of a single material, which makes fabrication of these layers facile compared to the perovskite layer. It is clear from Figure 4.24 that the thiocyanates have a dramatic impact on film formation. What is unclear from the measurements shown, is how uniform each film is in terms of its optoelectronic properties on a long length scale. To probe this, PL-imaging of each film was performed, and the resulting images analysed. The resulting PL maps are shown in Figure 4.28.

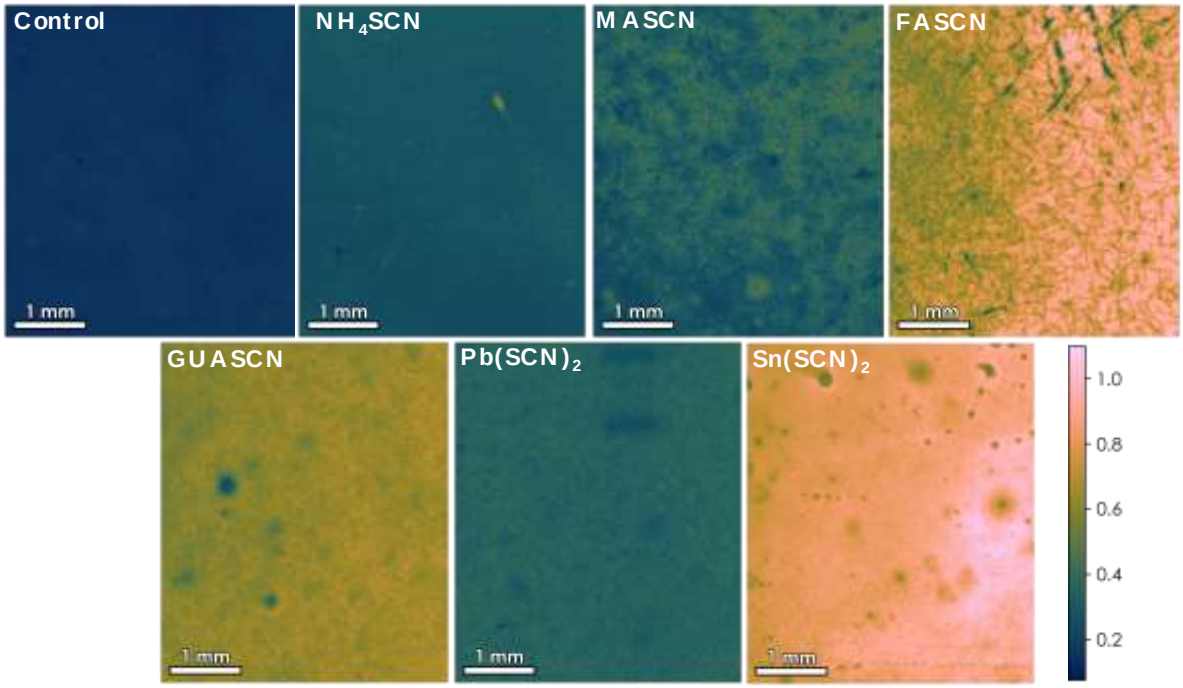

Figure 4.28 - PL images of films on glass substrates of a control film and those with thiocyanate additives. Measurements and plots by Akash Dasgupta, University of Oxford. The scale bar represents the relative PL of each sample versus a calibration standard. Further experimental details are available in Chapter 3.

From Figure 4.28 all films appear to be uniform apart from the FASCN sample which shows a high degree of heterogeneity and dendritic features that extend over a long-length scale (greater than 1 mm) which could introduce a high degree of roughness over the active area for a solar cell. This could imply that despite its high PLQE value it may be unsuitable for large area devices. All other additives showed good candidacy for thin film devices with significant enhancement in grain size, PLQE, and TRPL coupled with a similar degree of homogeneity in film morphology.

4.2.3 SCN additives - device performance

To investigate whether these improvements in absorber quality could be realised in devices, devices were fabricated using each additive utilising the *p-i-n* architecture. The device architecture and device performance metrics are shown in Figure 4.29.

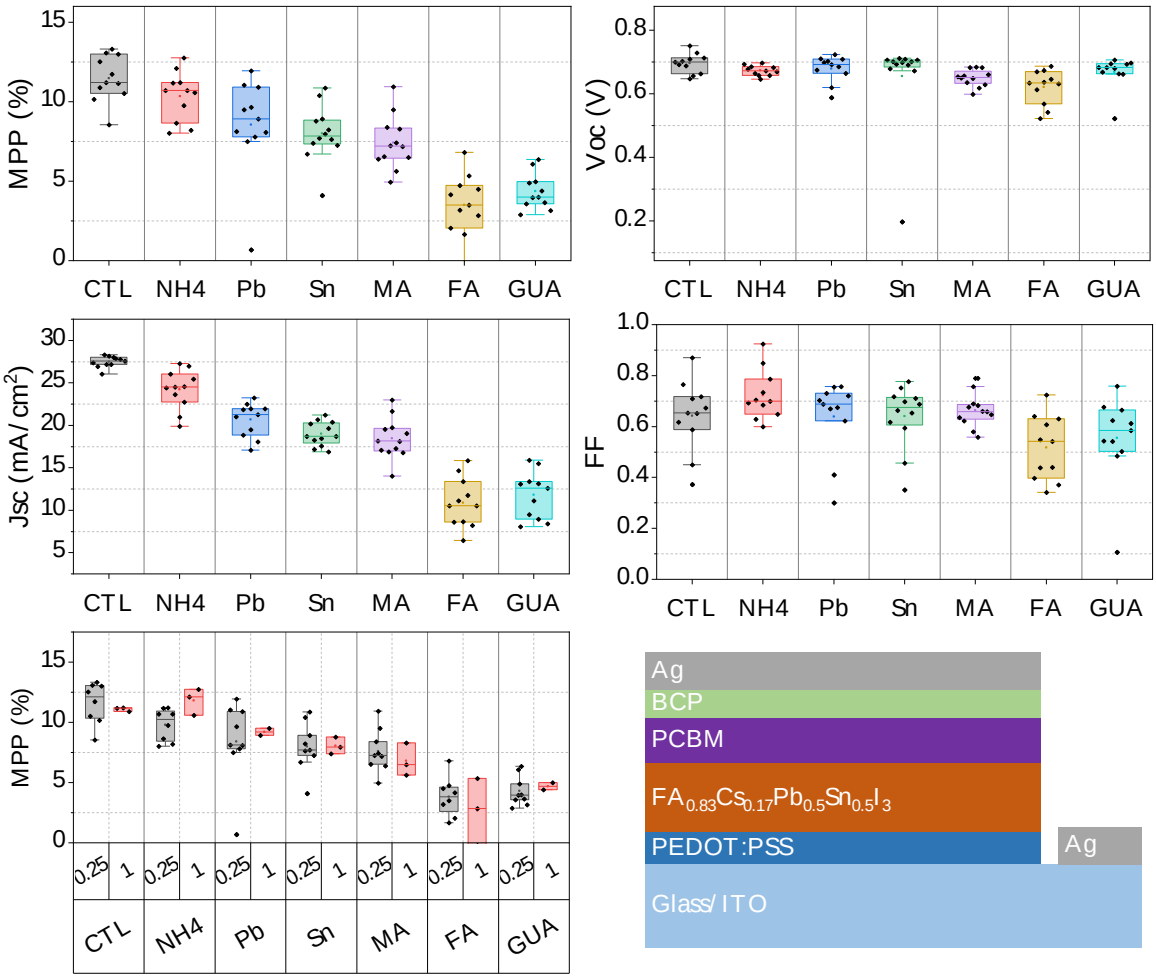

Figure 4.29 - All device metrics and device stack for devices consisting of a control and thiocyanate modified absorber layers. Respective device metrics are individually labelled. In the bottom left panel 0.25 and 1 represent device areas of 0.25 cm² and 1 cm² and were plotted to demonstrate layer uniformity. MPP represents the max

power point tracked efficiency over 60 seconds with the value being the final measurement point.

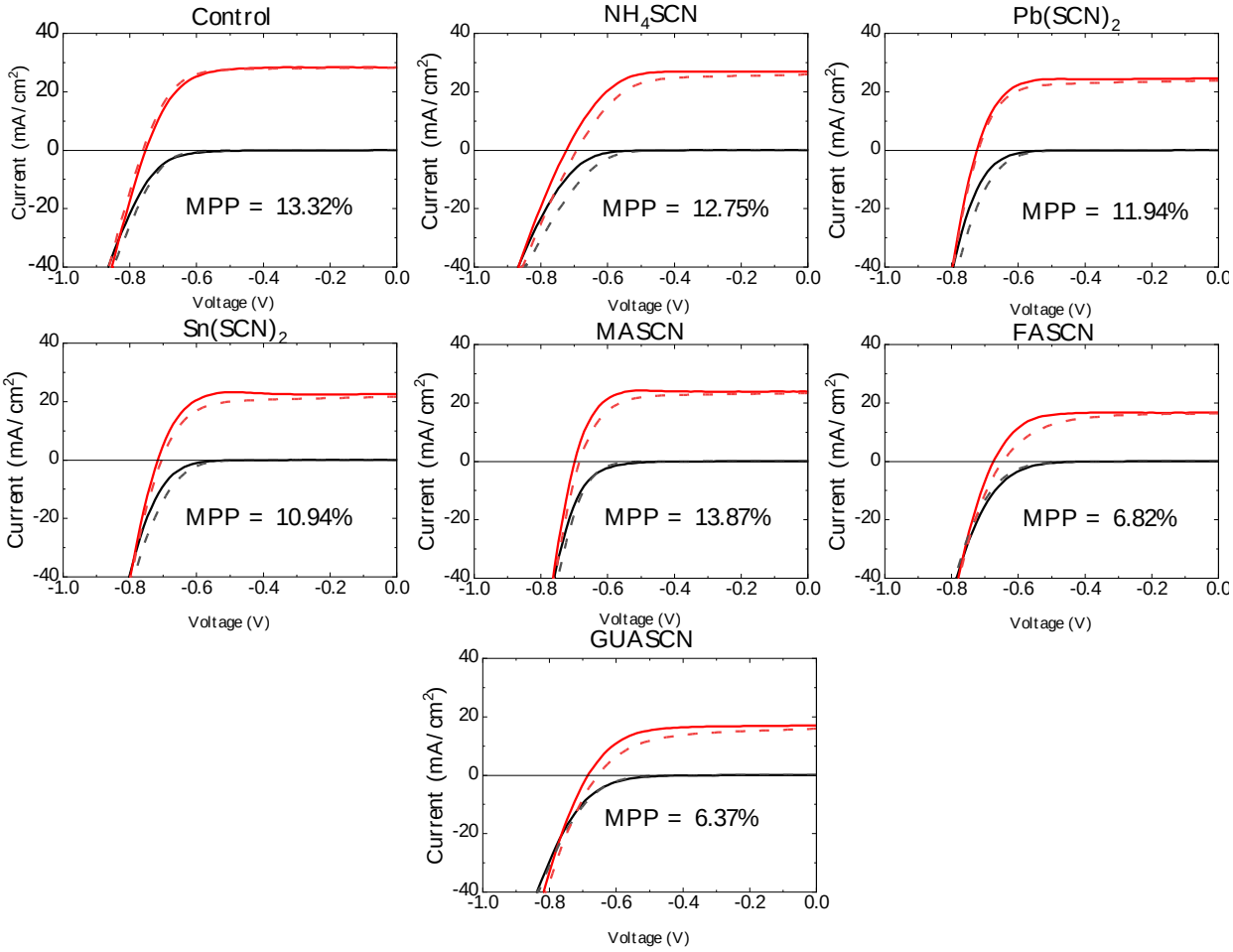

Figure 4.30 – The J-V curves for the champion device of each condition used in this study. It is noted that all SCN additives introduce a small amount of hysteresis, but it appears negligible. Devices are otherwise behaving as expected. The drop in current is clear from these J-V curves. Red traces are the J-V curves under light and the black traces the dark J-V. Solid lines are forward scans and dashed, reversed scans. The max power point tracked values after 60 seconds are given on each J-V plot.

The device metrics shown in Figure 4.29 show a drop off in max power point (MPP) for all additives, with the control having the highest performance of the batch. The main reason for this is the drop-off in current for SCN additives despite excellent calculated diffusion lengths. Surprisingly, there is also no *Voc* gain for any additives despite the very high PLQE values measured and the fact that non-radiative recombination has been reduced. One explanation for this could be due to an extraction barrier or significant recombination being introduced by the interfaces in a full device stack. What is more surprising is that all these additives have shown vast improvements for other PbSn perovskite blends that do not contain caesium[60]. Further detail on the choice of A-cation for this absorber can be found in Chapter 2.

4.2.4 XRD measurement

To elucidate why SCN containing devices do not show an improvement over the controls, X-ray diffraction was performed on witness films to see if any differences could be measured in the SCN-modified films composition despite previous reports indicating no change unless larger excesses (>50 mol%) were used in FAMAPbSn blends[61]. The resultant X-ray diffraction patterns are shown in Figure 4.31.

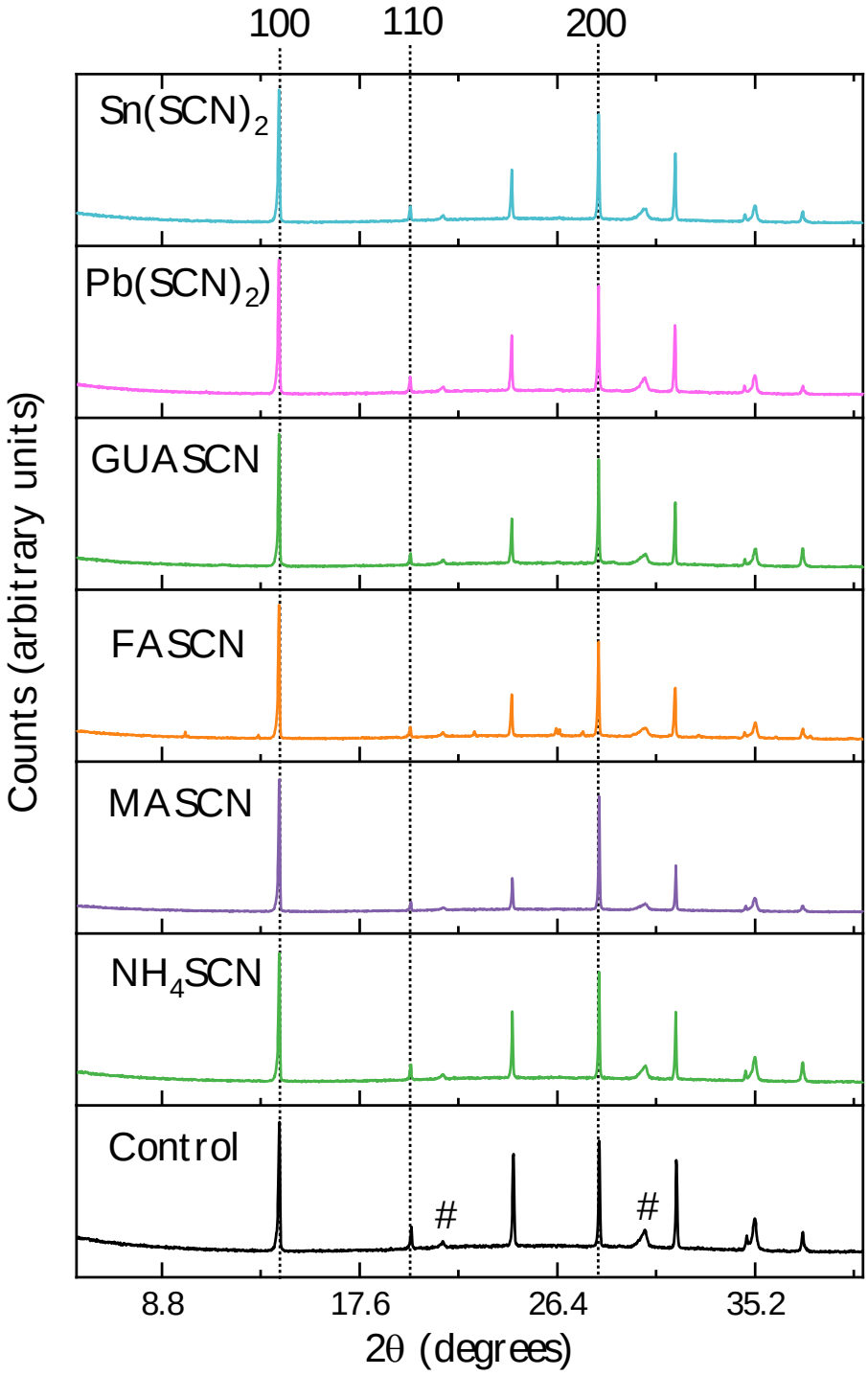

Figure 4.31 - XRD diffraction patterns of SCN modified films. ITO peaks are labelled with #. Intensity on the y-axis is scaled individually in each panel so (100) peaks can be clearly identified in each sample. The characteristic (100), (110), and (200) cubic peaks are highlighted with dashed lines.

From the scale shown, no differences are immediately clear. However, when the XRD patterns are magnified, distinct new peaks in the GUASCN and FASCN modified films can be seen (Figure 4.32). These can be assigned to the layered hexagonal polytype $GUASnI_3$ and δ-$CsPbI_3$, respectively, as reported by Stoumpos *et al.*[112] and Straus *et al.*[113]. It is postulated that these lower dimensional, wider gap[114] materials sit at the interfaces of these films giving high PLQEs while creating a barrier to charge extraction. It is also speculated that these lower dimensional phases occur in all samples but in very small quantities not detectable by 1D-XRD.

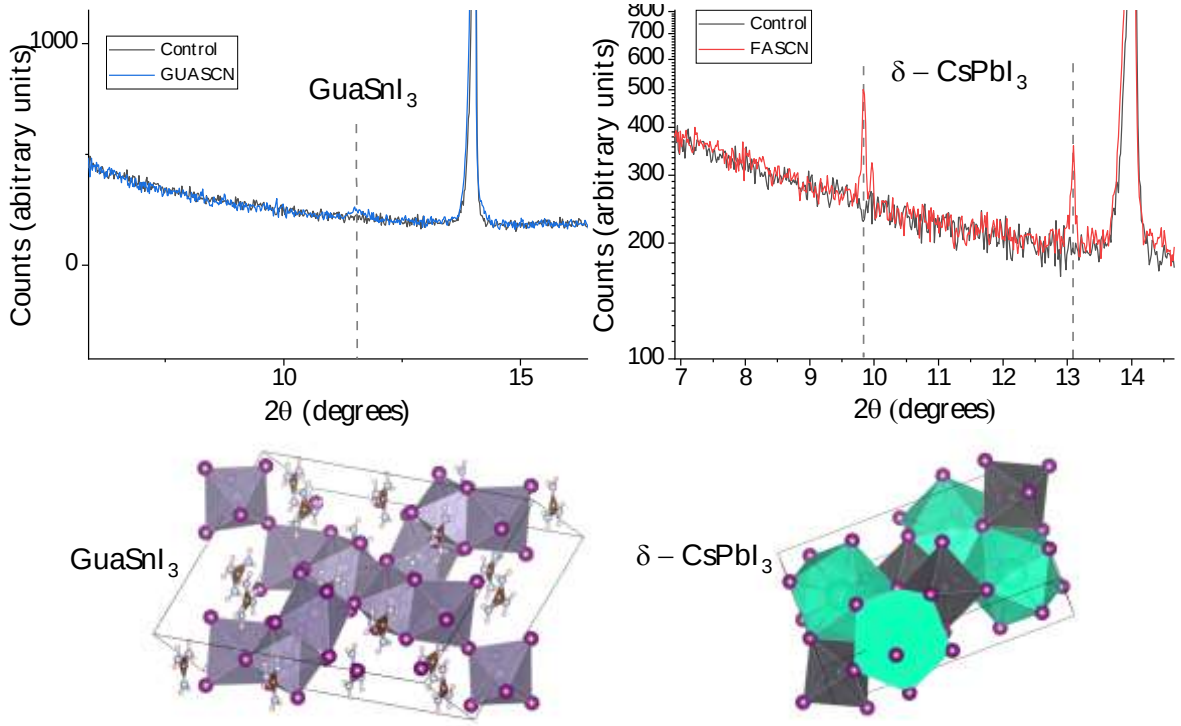

Figure 4.32 - XRD patterns of GUASCN and FASCN modified films magnified to show the appearance of new peaks assigned to $GUASnI_3$ and δ-$CsPbI_3$. Crystal structures generated using VESTA 3[115] and .cif files from references[112,113].

4.2.5 Interfaces and Passivation

Figure 4.34 shows the work function for indium tin oxide (ITO) and the highest occupied molecular orbital (HOMO) level energies for the hole transporters selected for this study. The value of -5.1 eV for the valence band of the perovskite absorber is as reported by Eperon *et al.* for an $FACsPbSnI_3$ absorber blend[59] similar to the one used in this study ($FA_{0.75}Cs_{0.25}Pb_{0.5}Sn_{0.5}I_3$ versus $FA_{0.83}Cs_{0.17}Pb_{0.5}Sn_{0.5}I_3$). The hole transporting materials studied in this section were chosen for their ability to perform well for the Pb-based materials, their ease of processing, and the range of HOMO levels, as it has been reported that careful alignment of the HOMO level to the valence band of the perovskite is desirable to maximise Voc[96]. They comprise of the ubiquitous PEDOT:PSS (Al4083), polytriarylamine (PTAA), and several self-assembled monolayers (SAMs); V1036, MeO-2PACz, 2PACz and Me-4PACz. The self-assembled monolayers used in this study are unlikely to be hole transporting layers when compared to PTAA or PEDOT:PSS due to the fact they are single molecules. It is more likely that they provide a favourable surface modification at the ITO/perovskite interface to facilitate hole transfer. These were synthesised and provided by Kaunas University of Technology, Lithuania[96].

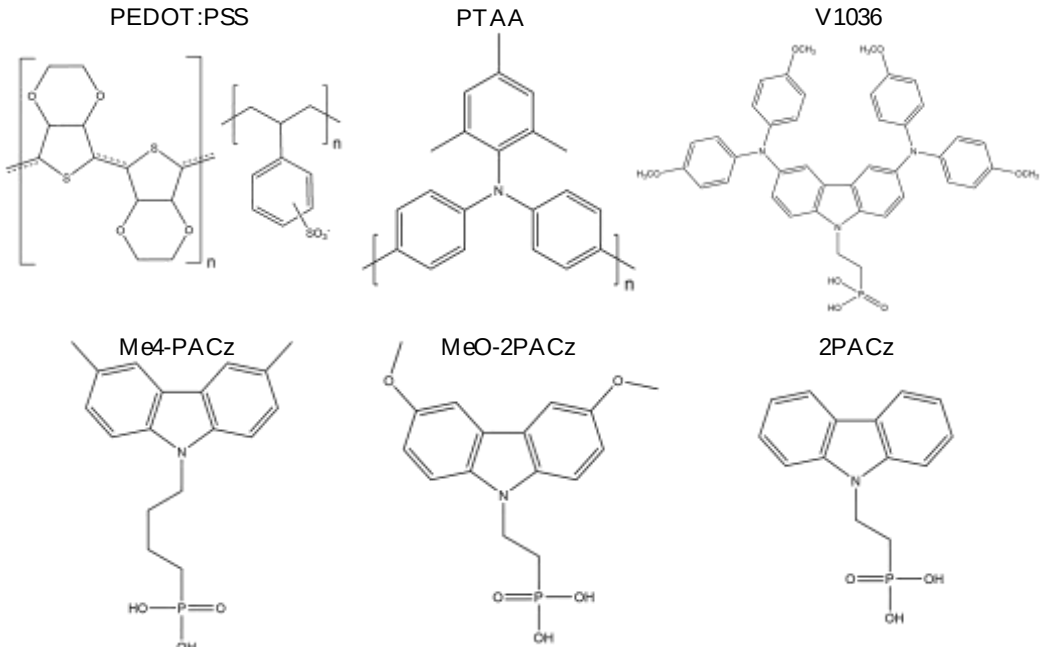

Figure 4.33 – The structure of all the HTLs used in this study. PEDOT:PSS and PTAA are polymers.

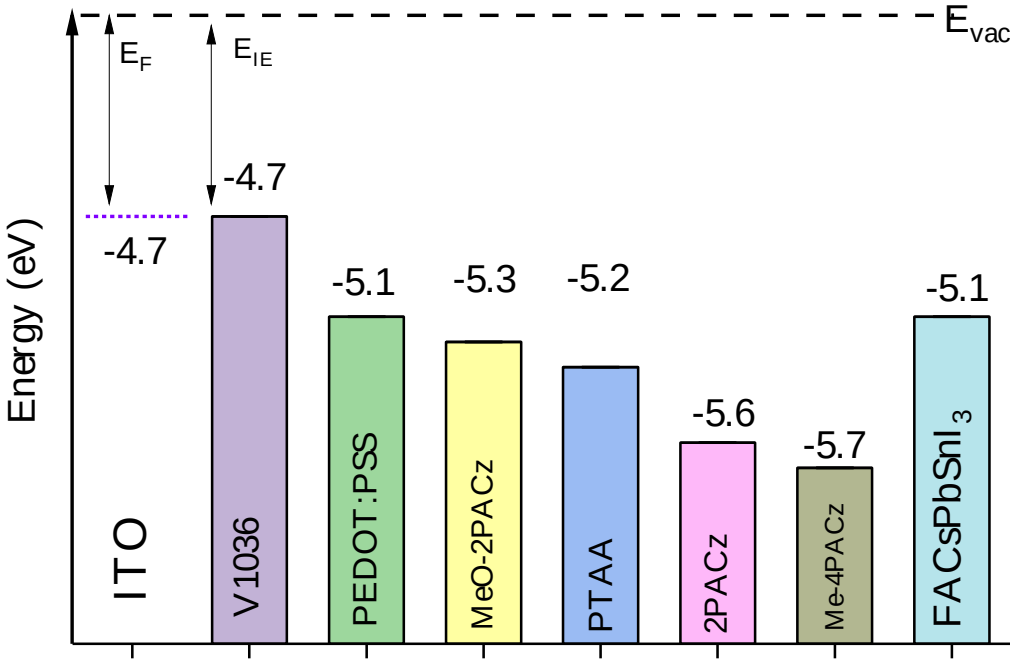

Figure 4.34 – Reported values for the Fermi level of ITO[116], the HOMO levels of the hole transporters used in this study[96] and the valence band onset for

$FA_{0.75}Cs_{0.25}Pb_{0.5}Sn_{0.5}I_3$ with respect to vacuum[59]. The values were taken from literature reports.

4.2.6 PLQE at the HTL interface

PLQE was used to quantify the amount of non-radiative recombination introduced by each HTL. The method used earlier in this chapter is used to calculate the quasi-Fermi level splitting (QFLS) with identical values of $J_{0,rad}$ and J_{SC}. Half stacks were fabricated consisting of glass/ITO/HTL/perovskite and glass/perovskite samples as a reference. Figure 4.35 shows the PL emission spectra used to calculate the PLQE values and Figure 4.36 shows the calculated QFLS values, which are summarised in Table 4.. The maximum QFLS value for this absorber is also displayed to highlight the losses introduced even when in contact with glass. A signal for PEDOT:PSS could not be detected in the PLQE apparatus used due to the amount of non-radiative recombination introduced by the HTL, as the setup used has low signal to noise sensitivity. Another consequence of this low signal to noise sensitivity of the setup is that resulting plots in Figure 4.35 appear as rough lines rather than smooth gaussians, commonly seen in for PL data taken for perovskites that emit within the visible range.

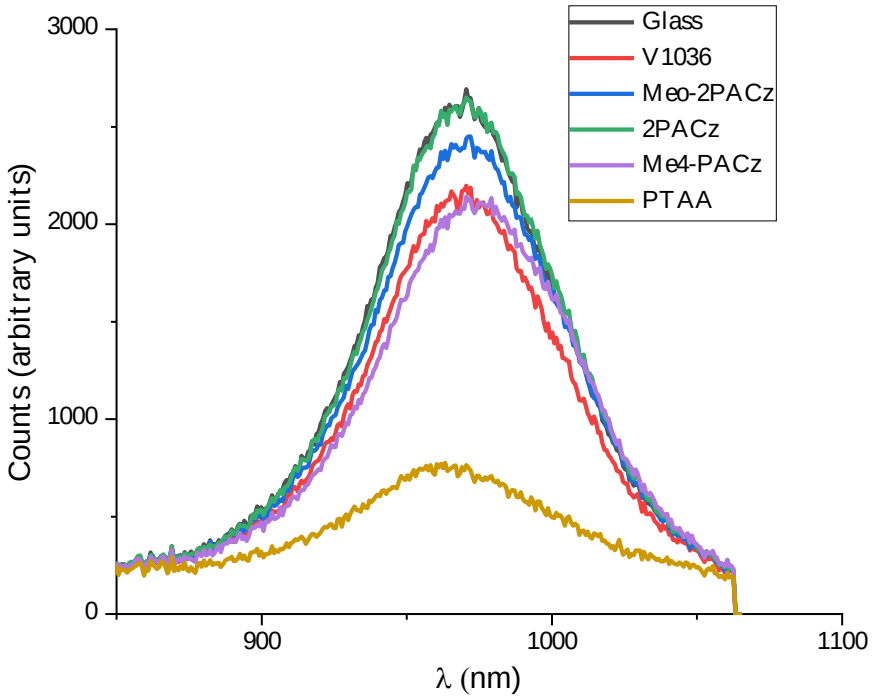

Figure 4.35 – The measured PL used to calculate the PLQE.

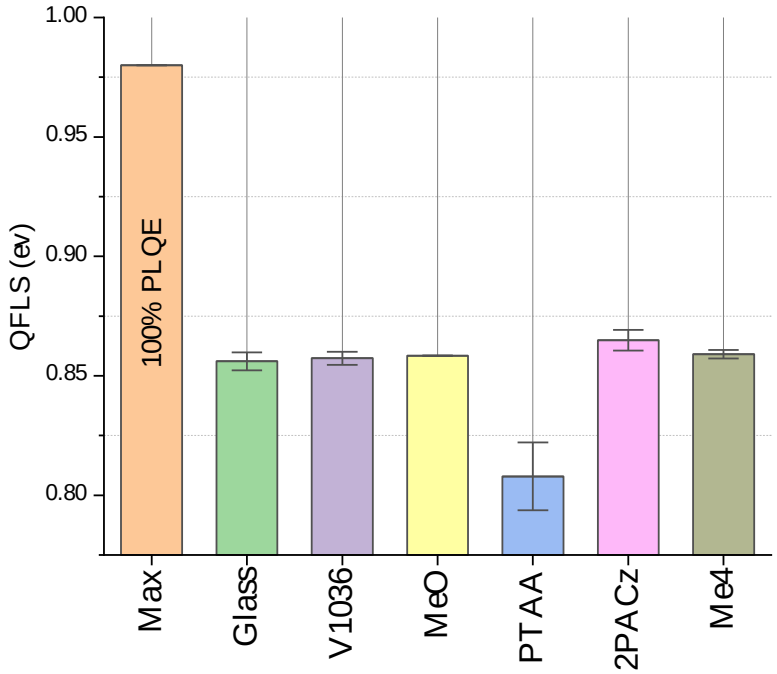

Figure 4.36 - Calculated QFLS values for the maximum acheivelable PLQE for this absorber, perovskite on glass and ITO/hole transporter half stacks. The stacks

utilising self-assembled monolayers (SAMs) introduce no additional non-radiative recombination relatvie to the glass sample.

Surprisingly, the SAM layers show QFLS values similar to those of the neat absorber on glass, and in most cases, enhance the PLQE (and the QFLS). This indicates that the SAM/perovskite interface suffers from no additional non-radiative recombination compared to the glass/perovskite interface. PTAA introduces a significant amount by comparison but still has detectable values versus PEDOT:PSS.

Condition	**PLQE A (%)**	**PLQE B (%)**	**QFLS A(eV)**	**QFLS B (eV)**
100% PLQE	100	-	0.98	
Glass	0.71	1.03	0.85	0.86
PTAA	0.24	0.08	0.82	0.79
Me4	0.93	1.07	0.86	0.86
2PACz	1.06	1.48	0.86	0.87
MeO-2PACz	0.97	0.98	0.86	0.86
V1036	1.04	0.84	0.86	0.85

Table 4.7 - The measured PLQE for 2 samples of each condition labelled A and B and the calculated QFLS values of each.

Next, the effect of the ETLs on the PLQE was investigated by fabricating samples with two further configurations: glass/perovskite/ETL to show the effect of the ETLs alone and glass/ITO/HTL/perovskite/ETL to study the

combined effects and approximate a complete device stack. The resultant QFLS values are displayed in Figure 4.38. It is clear from Figure 4.38 that the ETL side of the stack also introduces significant non-radiative recombination to the interface regardless of the ETL choice.

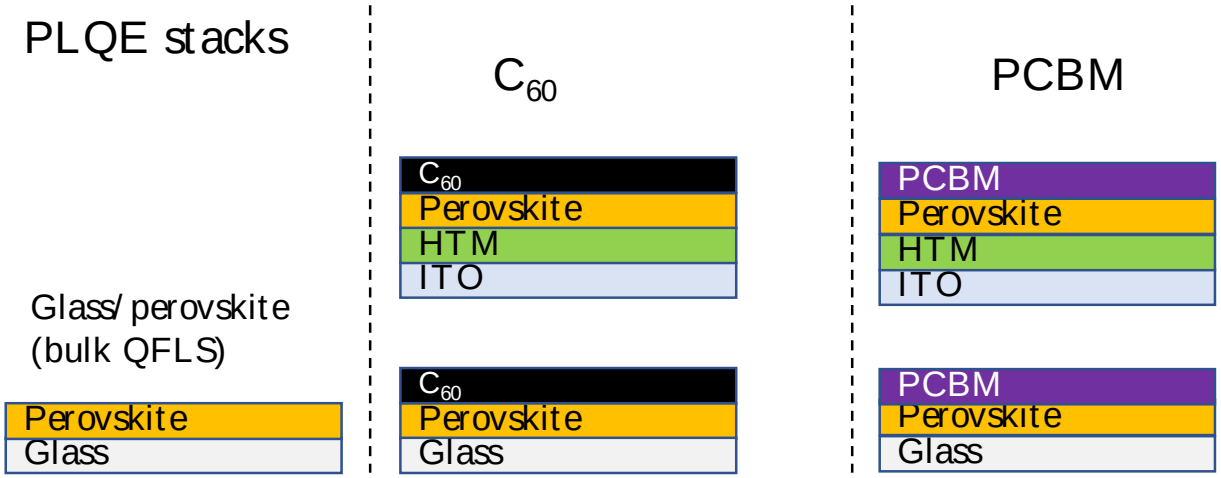

Figure 4.37 – the configurations used to measure the PLQE of the samples shown in Figure 4.38. Samples were illuminated through the glass or ITO side to be consistent with device illumination.

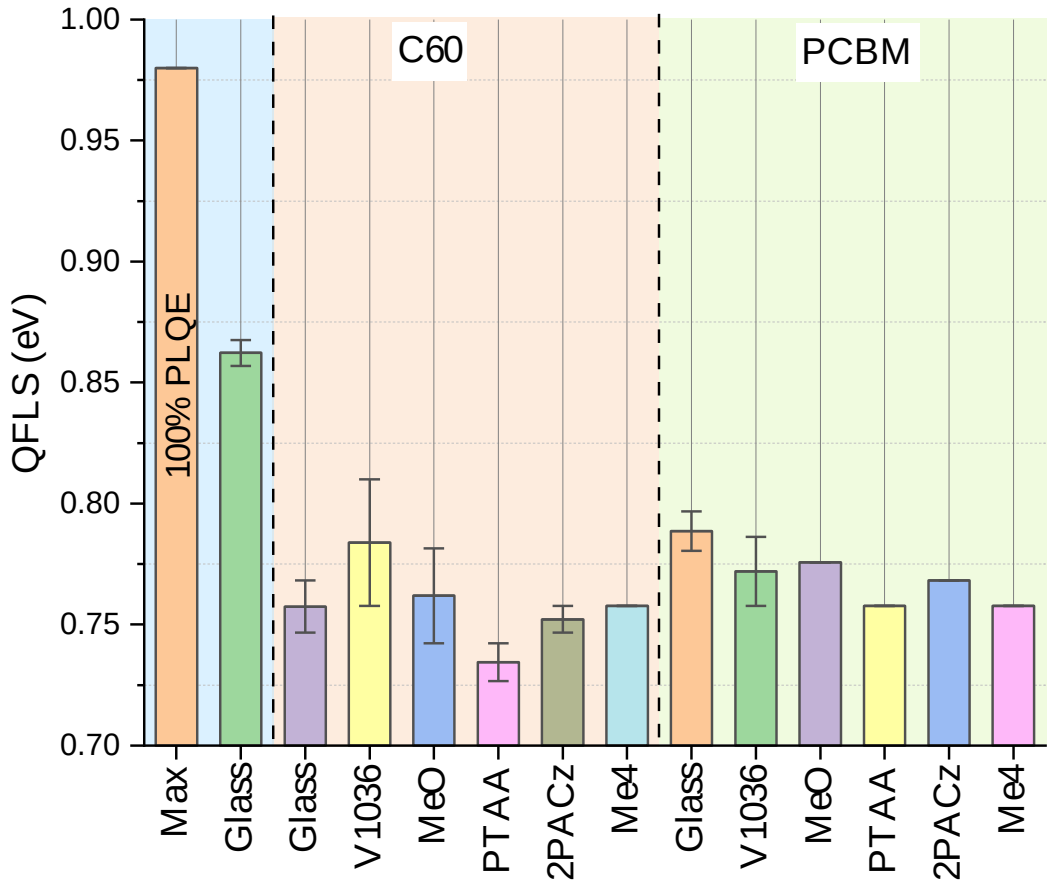

Figure 4.38 - The calculated QFLS values for two stack configurations - glass/perovskite/ETL and glass/ITO/HTL/perovskite/ETL to observe the losses introduced by the ETL interface.

After assessing the loss in QFLS of the ETL, companion devices using PCBM were fabricated to assess the impact the HTLs had on devices. C_{60} was not used in devices as evaporated BCP (crucial for devices in this configuration) was not available during this study.

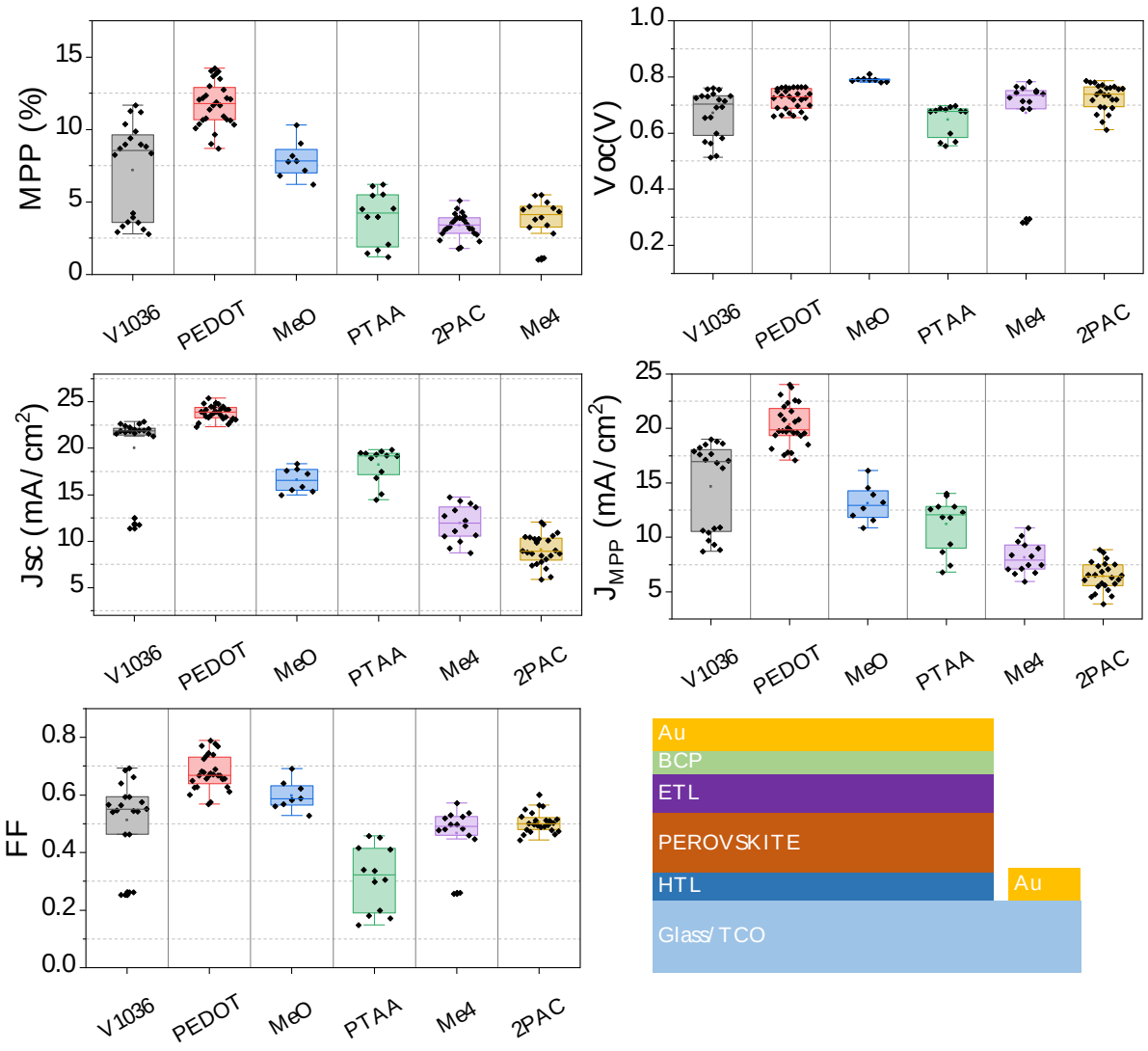

Figure 4.39 - Full statistics for devices fabricated using all HTLs and the general device structure used for fabrication.

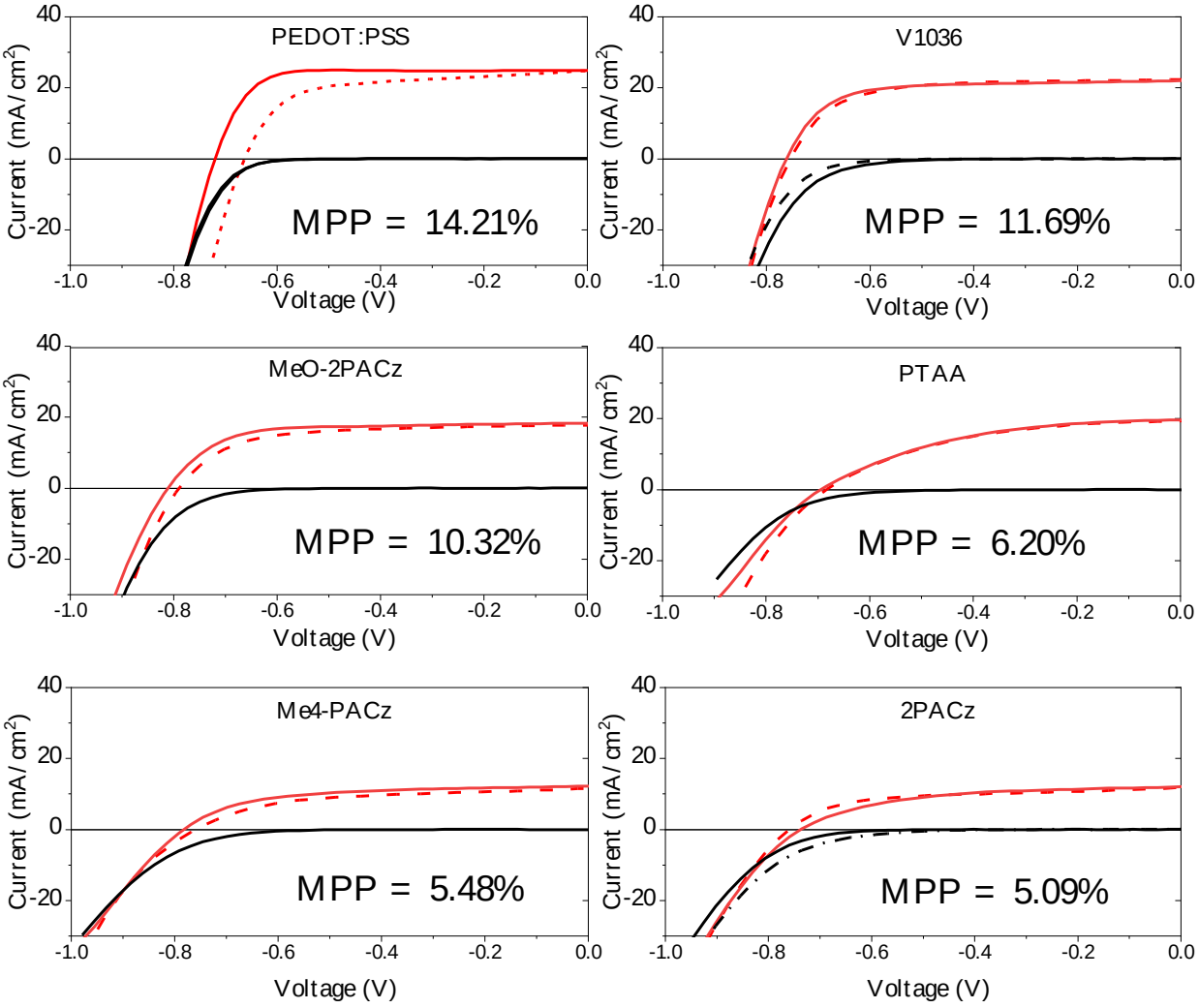

Figure 4.40 - The J-V curves for the champion device of each HTL used in this study. Interestingly, hysteresis seems most severe in the PEDOT:PSS device but the MPP appears largely unaffected. Red traces are the J-V curves under light and the black traces the dark J-V. Solid lines are forward scans and dashed, reversed scans. The max power point tracked values after 60 seconds are given on each J-V plot.

Figure 4.39 shows the device statistics for devices fabricated with the respective HTLs. The V_{OC} in each device correlates well with the QFLS values calculated for HTL/perovskite/PCBM stacks confirming the reduction in non-radiative recombination at this interface. The MPP, however, drops off across the series, which is clearly due to the drop in current and appears to be an issue with charge extraction. As all of these materials have been studied in *p- i-n* cells previously[96,117], parasitic absorption was ruled out. There are two postulates for this loss of current (schematics for both postulates are shown in Figure 4.41) :

1. The valence band offset for each hole transporter causes an energy level mismatch that could cause a barrier to current extraction. This would account for the drop in current for the HTLs with HOMOs lower than that of the value taken for the perovskite's valence band. This, however, does not hold for the shallower HOMO in V1036. If the HOMO level is shallower with respect to vacuum, this should provide a more favourable charge extraction for holes. It would be expected in the case of a shallower HOMO level that the V_{OC} would be reduced due to the impact on Fermi level splitting across the perovskite, but not J_{SC} [85].
2. A recent study by Thiesbrummel *et al.* highlighted a "Universal Current Loss" due to mobile ions present in PbSn devices[118]. At open-circuit, ions much like charge carriers move via diffusion due to no net internal field at open-circuit. When devices are held at short-circuit, the built-in field is at a maximum (further details can be found in Chapter 2). The built-in

field causes ions to drift to the contacts, these ions screen the built-in field resulting in a reduction in charge carrier drift and therefore less carriers are extracted. This happens over very short time scales and can be measured by an increase in photoluminescence as carriers recombine at short-circuit. It is speculated that PEDOT:PSS-based devices may not suffer as strongly from this effect due to its heavily doped nature and that this doping level can change under an applied bias[119].

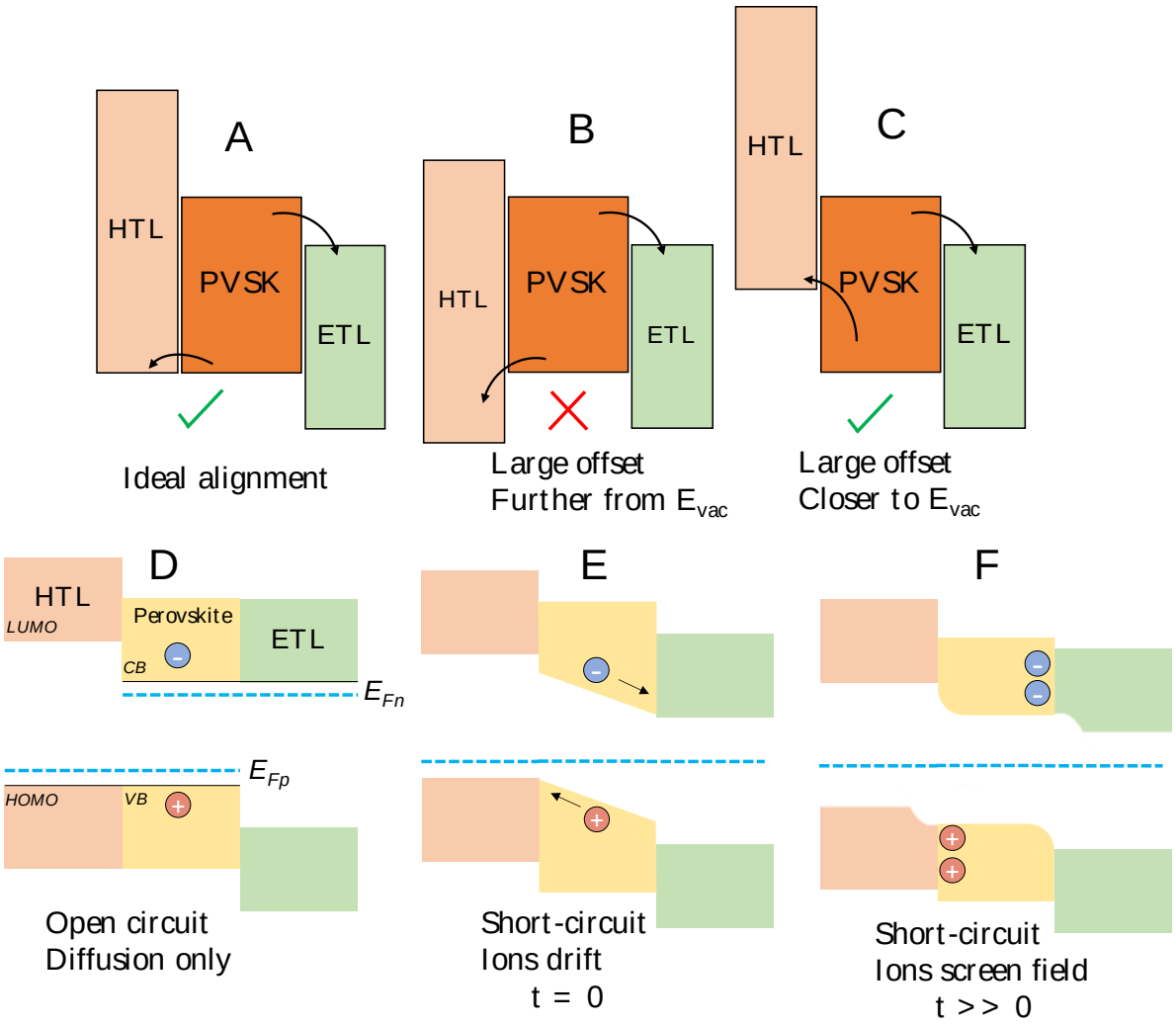

Figure 4.41 – Illustrations showing the mechanism in each postulation. A) represents ideal alignment of the HTL HOMO level and the perovskite valence band

(VB), showing favourable charge extraction B) shows the case of poor alignment with the HTL HOMO lying further from vacuum than the perovskite VB and a barrier to charge extraction as a result C) shows a large offset in HOMO level of the HTL but closer to vacuum still favouring charge extraction – the case for V1036. D) shows energy band diagrams for a device at open circuit with no carrier diffusion E) shows a device at short-circuit where mobile ions drift in the field F) shows the effect ions have on reducing the internal field once drifted.

Even though PEDOT:PSS induces a substantial amount of non-radiative recombination, device performance is still higher than those with high PLQEs, and its current extraction is the most efficient across the HTLs studied. Despite this, it would still be desirable to replace PEDOT:PSS with an HTL than can deliver high PLQEs (and QFLS) but allow charge extraction. To confirm the screening effect across the HTLs, PLQE measurements of full devices could be measured to see if the effect of increased PL seen by Thiesbrummel *et al.* occurs[118].

With all new HTLs performing poorly the focus was switched to the ETL side, which showed significant quenching of the PLQE. To try to address this, three passivations were chosen to see if the losses at the ETL could be mitigated. Lithium fluoride (LiF), phenylethylammonium chloride (PEACl), and formamidinium thiocyanate (FASCN) have all been shown as effective passivators[120–122]. Half stacks of glass/perovskite/passivation/ETL were fabricated and the resulting QFLS values calculated from PLQE measurements are shown in Figure 4.43.

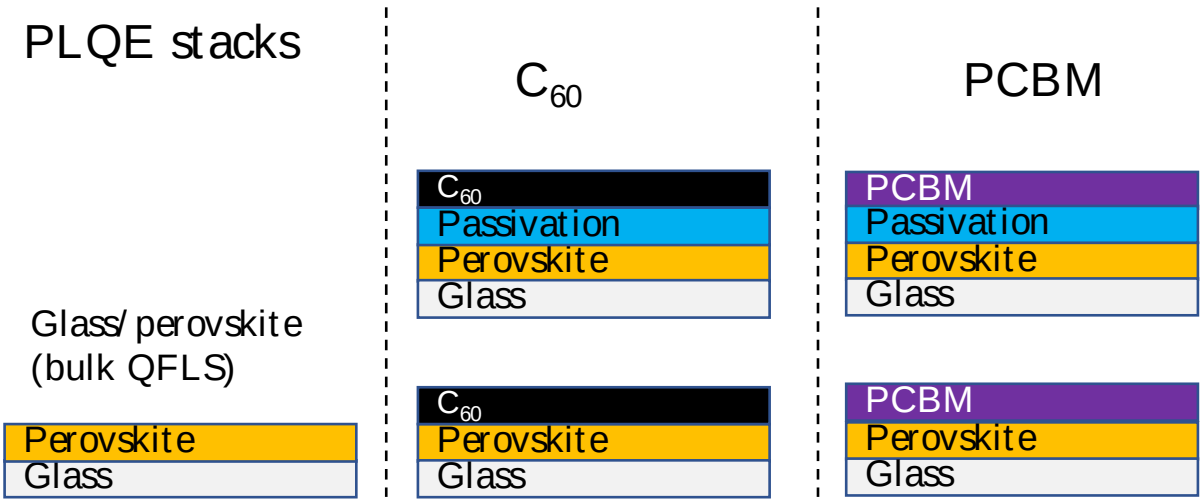

Figure 4.42 - the configurations used to measure the PLQE of the samples shown in Figure 4.43. Samples were illuminated through the glass or ITO side to be consistent with device illumination. .

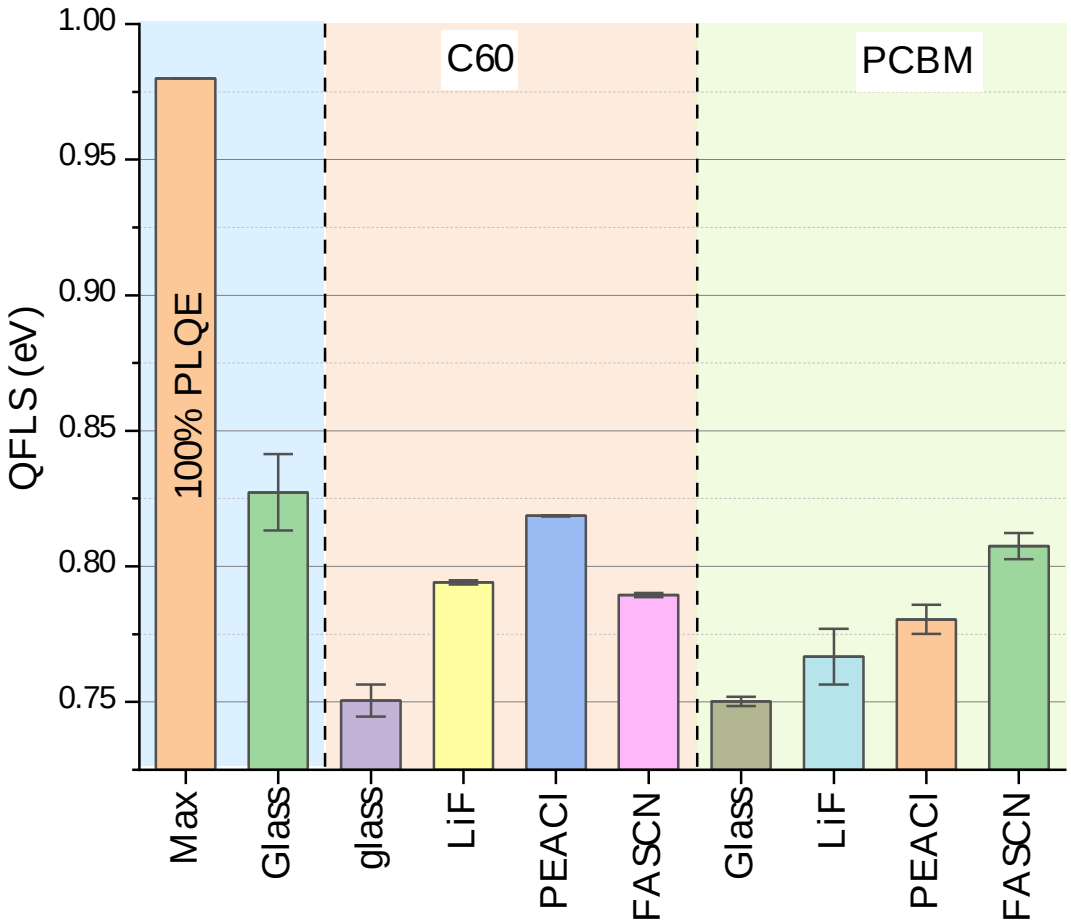

Figure 4.43 - QFLS values for half stacks comprised of glass/perovskite/electron transport layer and the same stack with 3 types of passivation layer deposited before the ETLs (C_{60} and PCBM) Lithium fluoride (LiF), phenylethylammonium chloride, and formamidinium thiocyanate were used as passivations in this study.

It is clear from Figure 4.43 that the effectiveness of the passivation layer also depends on the choice of passivation molecule and more likely the deposition method. As PCBM is solution processed from a mixture of chlorobenzene and dichlorobenzene, it is possible that certain types of passivation may be partially washed off by these polar solvents. As previously mentioned, limited to PCBM as the ETL for device fabrication, devices were constructed using FASCN as the passivator, as this achieved the highest QFLS in the set when combined with PCBM. Devices were fabricated using PEDOT:PSS due to the loss of current experienced in the other HTLs. As the FASCN was dissolved in isopropyl alcohol (IPA), an IPA rinse was also included into this device set along with FAI to decouple the roles of the FA^+ and SCN^-. The resulting device metrics are displayed in Figure 4.44. From the device metrics, the IPA rinse alone has a negative effect on MPP and whilst the FAI shows some improvement in champion cells, its median MPP is lower than the control set. The negative effect of the neat IPA rinse could be due to IPAs ability to dissolve Sn perovskites[123]. The FASCN samples, however, show an enhanced V_{OC} of almost 100 mV and, as a result, an increase in the MPP to champion value of 14.09% versus the control champion of 11.76%. This showed that the top surface could be effectively passivated by FASCN in devices as well as in

PLQE measurements by effectively reducing non-radiative recombination introduced by PCBM. In the future, several concentrations of FASCN should be trialled to find an optimum and to maximise device performance. The J-V curves for champion devices of the control and FASCN samples are shown in Figure 4.45, clearly showing the V_{OC} enhancement in the latter.

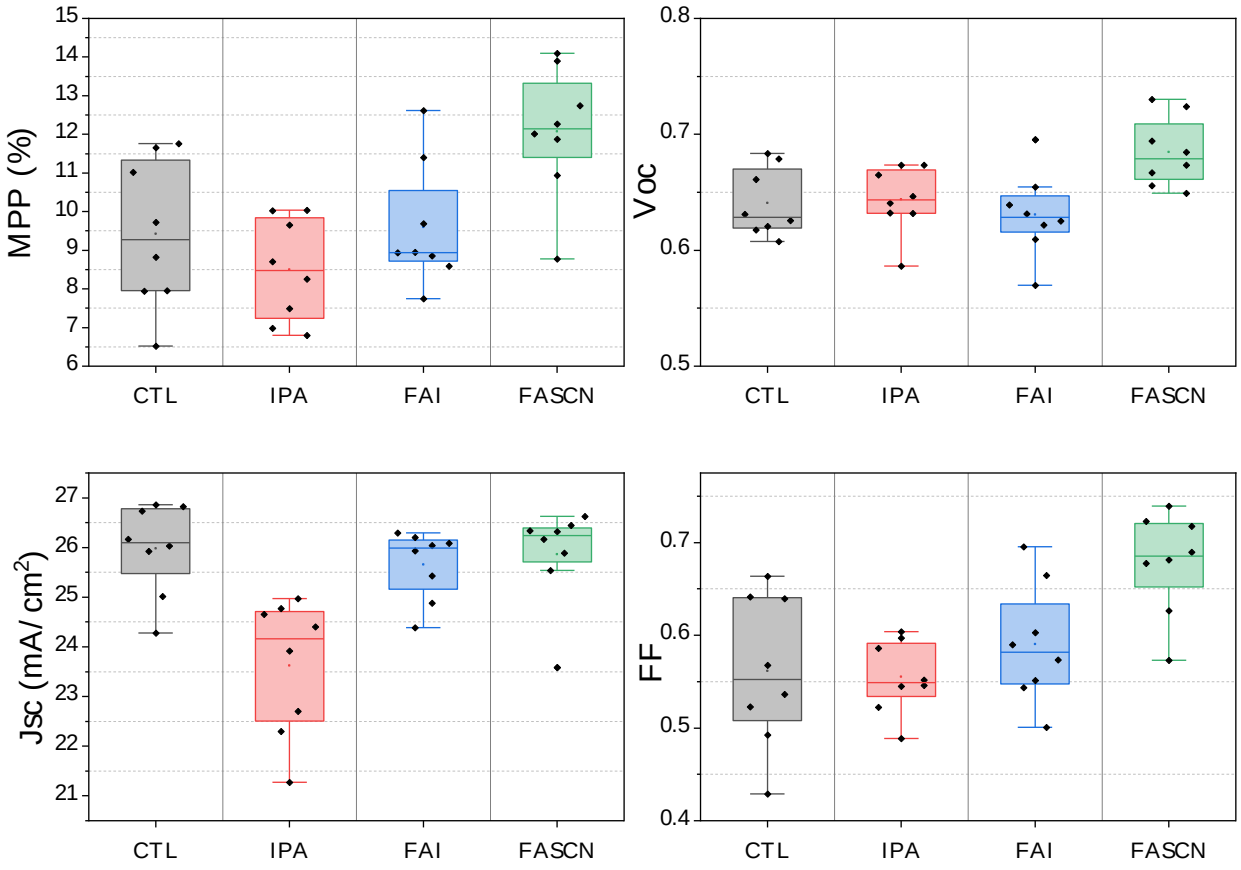

Figure 4.44 - Device metrics for control devices, treated with IPA and passivated with FASCN or FAI.

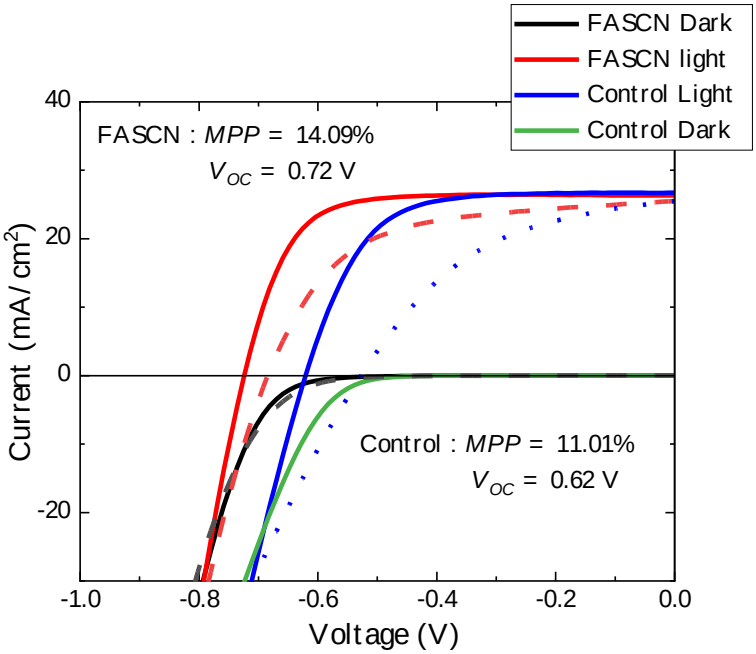

Figure 4.45 – J-V curves for the champion FASCN and Control samples showing the clear V_{OC} improvement from the FASCN passivation.

4.3 Summary and Outlook

In summary, several approaches to improving the performance of an $FA_{0.83}Cs_{0.17}Pb_{0.5}Sn_{0.5}I_3$ lead-tin absorber have been investigated. The passivation of the bulk via thiocyanate additives proved successful in enhancing the grain size, PLQE and diffusion lengths of resulting films. However, when these materials are incorporated into devices, they suffer from a loss in current density. This is postulated to be the result of unwanted lower dimensional phases being formed at the interface, hindering charge extraction. These materials do show promise in the neat films, and it may be that tailoring the concentrations by careful optimisation can enhance performance without creating unwanted bioproducts. In the second section of this chapter the influence of HTLs and ETLs on the QFLS of an $FA_{0.83}Cs_{0.17}Pb_{0.5}Sn_{0.5}I_3$ was investigated finding significant quenching occurring at both interfaces when the common HTL, PEDOT:PSS, and the ETLs, PCBM and C_{60}. Despite several alternative HTLs showing promise and preserving the QFLS of the neat material, resulting devices suffer from poor performance due to a loss in current density and therefore MPP. It is shown that whilst PEDOT:PSS introduces significant non-radiative recombination at the HTL interface (so much so that a PLQE value cannot be measured), it still outperforms HTLs that show very little PLQE quenching. Similarly to the observations by Thiesbrummel e*t al.*[118], it is postulated that due to mobile ions screening the field at short-circuit, the field within the device is reduced, decreasing charge-carrier drift in the device. This severely diminishes charge

extraction in devices fabricated using the alternative HTLs lowering current. Due to its highly doped nature, it is speculated that devices using PEDOT:PSS are less affected by the screening caused by mobile ions, allowing for better current extraction and performance compared to the other HTLs. Finally, a successful passivation agent is found in FASCN that can effectively reduce non-radiative recombination at the ETL interface, boosting overall device performance largely due to a V_{OC} enhancement. This work highlights the need for more hole transporting layers that are compatible with $FA_{0.83}Cs_{0.17}Pb_{0.5}Sn_{0.5}I_3$ perovskites to improve device performance and contacting materials that can preserve the PLQE of an absorber but still allow charge extraction, such as FASCN. It also shows that PLQE as a tool can be used to screen passivation and contacting layers for PbSn perovskites, but devices must always be fabricated in parallel. As a final thought, the processing of PbSn absorbers remains extremely challenging, especially the $FA_{0.83}Cs_{0.17}Pb_{0.5}Sn_{0.5}I_3$ perovskite. Despite this, these materials show great promise for their application in single junction and tandem solar cells if the high PLQE values and long lifetimes can be translated to high efficiency devices.

Chapter 5.

Optimisation and Integration of Lead-Tin Solar Cells for Tandem Solar Cells

In this chapter several tandem solar cells utilising an $FA_{0.83}Cs_{0.17}Pb_{0.5}Sn_{0.5}I_3$ absorber are constructed experimenting with different architectures and configurations. It is found that careful optimisation of the narrow band gap sub-cell is crucial for performance as well as an appropriate recombination layer design. The culmination of the work in this chapter results in the first working *p-i-n* tandems constructed in the Oxford, Photovoltaic and Optoelectronic Device group and a record for a 1 cm^2 all-FACs based tandem of 20.63% power conversion efficiency (PCE).

5.1 Introduction

The Shockley-Queisser, power conversion efficiency limit for a single junction photovoltaic is approximately 34% for an absorber with a band gap of around 1.34 eV[124]. To overcome this limit and increase the power density (W/m^2) of photovoltaic modules, multijunction or tandem solar cells that utilise two or more sub cells can be stacked on top of each other to extract more charge carriers efficiently, mitigating energy loss due to thermalisation. There are two main types of architecture studied in the perovskite field, two terminal (2T) monolithic and four terminal (4T) mechanically stacked cells. The latter is considered easier to fabricate when using solution processed all-perovskite tandems due to the need for orthogonal solvents when processing each layer in a 2T stack (as similar solvents will dissolve the previously deposited layer)[125].. Eperon *et al.* published the first 2T all-perovskite tandem utilising a superstrate architecture where the wider band gap material is processed on the TCO substrate first, followed by the narrow gap absorber. They achieved a power conversion efficiency of 17% and a V_{OC} of 1.65 V for a device with an active area of 0.12 cm^2 [126].

The main body of this chapter focusses on device optimisation and fabrication. 2T superstrate tandems are constructed in parallel to form a basis of understanding with fabrication issues addressed. The initial batches utilise a non-ideal wide gap perovskite of 1.63 eV as a proof of concept and trial fabrication. The final section of this chapter focusses on the fabrication of 2T

tandems using a 1.8 eV absorber as the wide gap material combined with an optimised 1.27 eV lead-tin (PbSn) junction with improved diode characteristics and high efficiency. A PCE of over 20% is achieved for cells with active areas of 0.25 and 1 cm^2.

5.2 Results and Discussion

5.2.1 Two terminal (2T) monolithic tandems - Initial trials

At the initiation of this project, the atomic layer deposition tool (ALD) and compact tin oxide (SnO_2) material necessary to construct a tandem of the desired architecture were not available within the POD group at Oxford. Subsequently, the wide band gap (WBG) sub-cell was fabricated by Dr Adriana Paracchino of CSEM Switzerland as part of a collaboration. Dr Paracchino fabricated sub-cells using a 1.62 eV absorber ($FA_{0.83}Cs_{0.17}Pb(I_{0.83}Br_{0.17})_3$) and a compact SnO_2 electron transporting layer via ALD. Although not an ideal band gap for 2T tandem cells (with the optimum being around 1.8 eV[64]) this was CSEM's highest efficiency absorber at that time. Sub-cells were shipped to Oxford where the narrow band gap sub-cell was fabricated on top. The cells were then finished and tested in the University of Oxford. These cells displayed less than ideal performance due to the formation of a shunt diode, due to low R_{SH}, across the narrow gap cell. Figure 5.46 shows the superstrate stack used to fabricate 2T tandems and an SEM cross section of a representative device.

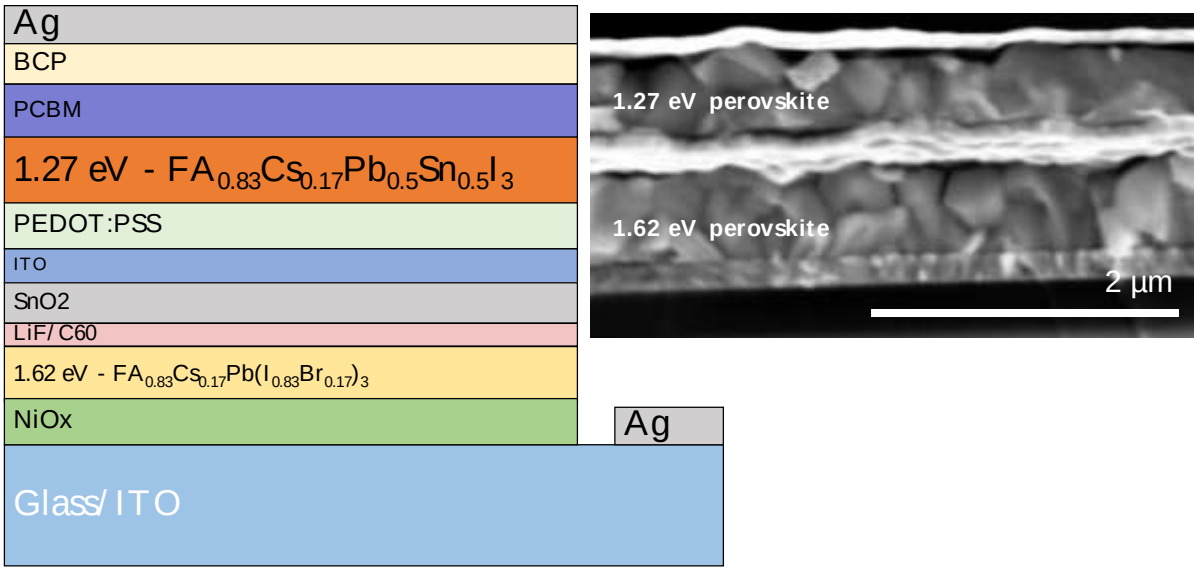

Figure 5.46 - The complete device stack for the 2-terminal tandems fabricated by CSEM and UOXF. Right of the stack is an SEM cross section of a device after testing.

Several batches of tandems were fabricated with varying success due to poor performance of the narrow band gap (NBG) perovskite deposited on top. Figure 5.47 and Table 5.6 show the full device metrics for a batch with the highest working efficiency using this method of fabrication.

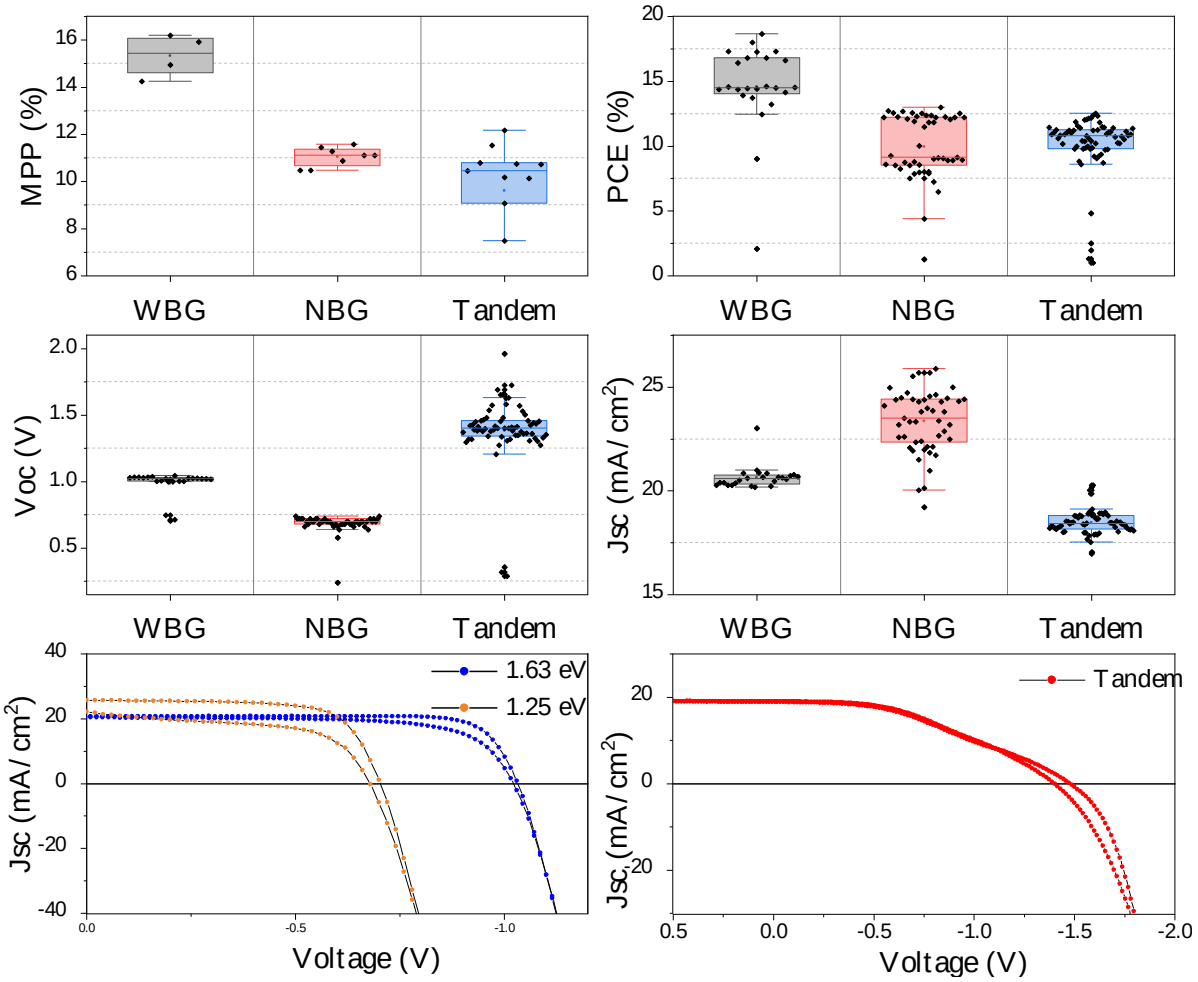

Figure 5.47 - Statistics of the individual control cells and the 2T tandems. The bottom two panels show, left, the individual sub cell champions and, right, the 2T tandem champion. Note the s-kink close to the max power point on the tandem cell. Cell area is 0.2 cm^2. MPP represents the max power point tracked efficiency over 60 seconds with the value being the final measurement point whereas PCE is the efficiency calculated from the J-V curve.

Cell	Jsc (mA/cm²)	PCE (%)	Voc (V)	FF	MPP (%)
Tandem(F)	18.97	12.14	1.41	0.45	-
Tandem(R)	18.79	11.89	1.35	0.47	12.17
NBG (F)	22.09	8.80	0.68	0.58	-
NBG (R)	25.70	12.97	0.70	0.71	11.57
WBG (F)	20.74	17.29	1.03	0.81	-
WBG (R)	20.40	14.38	1.02	0.69	16.19

Table 5.6 - Device metrics for a batch of 2T-tandems and the individual narrow band gap and wide band gap cells.

Figure 5.47 and the metrics displayed in Table 5.6 show there is clear voltage addition in the 2T tandem, however, the voltage is much lower than expected as both sub cells combined should achieve a V_{OC} of approximately 1.7 V - the champion cell only achieved 1.41 V. Whilst the J_{SC} in the NBG cell is much too low to for an efficient tandem, the J_{SC} achieved in the tandem cell is much too large to be functioning normally. An s-kink can also be seen at the max power point on the J-V curve. After some initial measurements, all devices were isolated by scratching around each device individually to remove any conductive layers between devices which can cause crosstalk, which may have accounted for the high J_{SC}. With the large current still measured post-scratch, it was postulated that due to the nature of the solution processing route and the failures seen in previous batches, that there may be a shunt pathway

across the NBG sub cell. This shunt pathway was modelled by adding a shunt diode across the NBG sub cell in a circuit model. The equivalent circuit model and resulting modelled J-V curve superimposed over the real J-V curve for the 2T-tandem is shown in Figure 5.48.

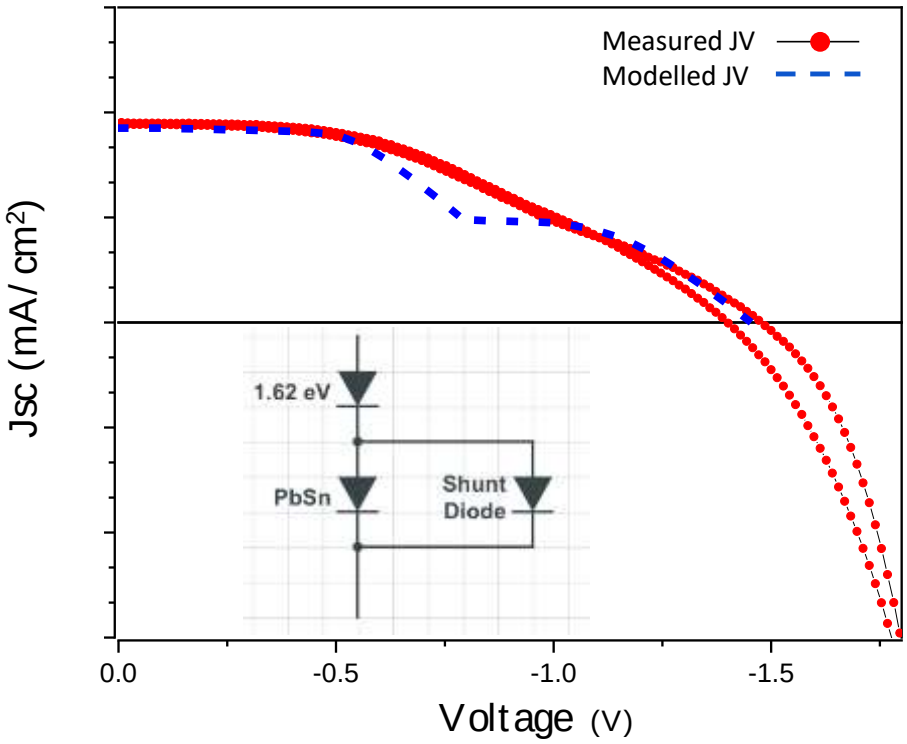

Figure 5.48 - The equivalent circuit model assuming diode like shunt characteristics and the resulting J-V characteristics. Modelling performed by Dr Suhas Mahesh, University of Oxford.

A shunt pathway across the NBG cell can account for the high short-circuit current and the low *Voc*. The effect was modelled through circuit analysis assuming a diode-like shunt characteristic and varying all diode parameters to obtain the best fit. This shunt diode was postulated to arise from pinholes

in the NBG sub cell. It was clear from these results that the processing of the NBG sub cell is crucial. This processing issue is addressed in the next section.

5.2.2 Narrow band gap absorber shunts

It was postulated that shunts in the previous batch were caused by pinholes and voids from rapid crystallization of the absorber layer. These could be observed as large "cloudy" areas on the glass/ITO side of single junctions that on close inspection looked like pockets of gas or voids. This was a regular occurrence over many batches when using a previous cell design. It is thought that this was not an issue with the group's previous cell design as device areas were of a smaller area (0.091 cm^2 versus 0.25 and 1 cm^2). However, on longer length scales, the density of pinholes and voids has a greater impact as pinholes present areas where the semiconductor can be bypassed, giving low R_{SH} [127]. In Figure 5.50 these pockets can be clearly seen via the cross-sectional SEM image as large voids at the PEDOT:PSS/perovskite interface. This was also identified in an almost identical perovskite blend by Liu *et al.* when fabricating infrared photodetectors[128]. They addressed the issue via a confined low temperature anneal they termed the "double side crystalized tuning method (DSCT)" which consisted of a low temperature anneal under a petri dish followed by a 120 °C anneal as shown in Figure 5.49. Interestingly, recent work by Wang *et al.* has also shown the appearance of voids in pure-Pb materials[129]. They attributed this to the loss of residual solvent during annealing.

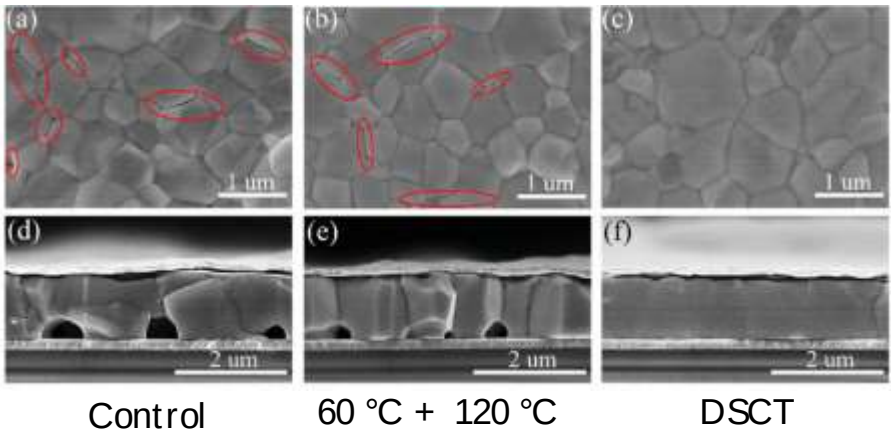

Figure 5.49 - The DSCT method created by Liu *et al.* to fabricate PbSn NIR photodetectors[128]. Adapted with permission.

The DSCT annealing method was replicated alongside a 100 °C control and a simple high temperature, 120 °C anneal. The higher temperature was chosen to drive off the higher boiling point solvents more quickly and to see the effects this has on the final film. It was thought this would cause more pinholes especially when considering the study by Liu *et al.* However, the DSCT method produced the lowest quality morphology and the 120 °C anneal produced pinhole and void free films. SEM images of the resulting films are shown in Figure 5.50.

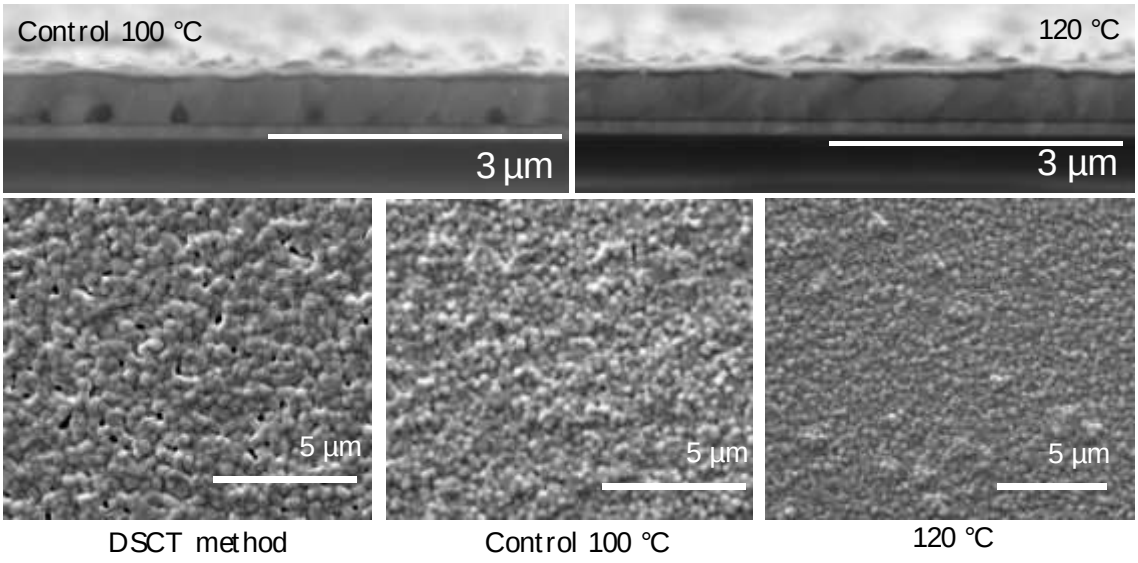

Figure 5.50 - Cross sectional and top-down SEM images of a control device and one annealed at 120 °C. At the bottom of the panel top-down SEM images are shown for films using the DSCT method, control temperature and 120 °C. Large voids at the PEDOT:PSS/perovskite interface can be seen for the control sample at 100 °C as well as pinholes in the top surface. The DSCT method shows the least favourable morphology, whereas 120 °C shows the best morphology. In retrospect, a side-by-side device comparison should have been made for witness devices, however, a consistent increase in yield and performance was realised from increasing the annealing temperature to 120 °C. This comparison was made at later date and is shown in the next section for both tandems and single junctions.

5.2.3 Full stack optimisation – contacts and passivation

With the installation of a new cluster tool deposition system, evaporated top contacts became achievable as well as ALD-deposited, compact SnO_2. Previously, this was only possible for C_{60} whilst the BCP layer was solution processed, which proved unsuccessful for complete cells, and limited the

choice of ETL to solution processed PCBM/BCP. High performance PbSn cells within the literature all utilise evaporated C_{60}/BCP top contacts[57,58,63,130]. In the next section solution processed and evaporated contacts are compared. A new passivation is also utilised in the form of an ethylene diamine and alumina nanoparticle (EDA/Al_2O_3-np) layer. Hu *et al.* fabricated a record PbSn cell in 2021 by using ethylenediammonium diiodide ($EDAI_2$)[57]. This solution processed passivation facilitated charge extraction at the top contact via the creation of a surface dipole. However, dissolution of the $EDAI_2$ proved unsuccessful with the same method for this study. In the same year, Kapil *et al.* utilised the related amine, ethylenediamine (EDA), to great effect but lower in performance than the cells published by Hu *et al.*[131]. During this time Heon Jin, University of Oxford, optimised an Al_2O_3-np layer deposited on the ETL side of PbSn perovskites that increased R_{SH} and improved all device metrics. At the time of writing, the exact mechanism is not understood. One hypothesis is that this alumina acts as a wetting layer to improve the coverage of spin coated PCBM. By combining the EDA and Al_2O_3-np into a single solution processed layer, devices fabricated in this study were enhanced. Cells were fabricated with and without the passivation layer for comparison. Evaporated C_{60}/BCP was also compared, including a bilayer using the "spike structure" first deployed by Kapil *et al.* in 2017 to enhance V_{OC}, which consists of a thin layer of PCBM (from a dilute solution) and an evaporated C_{60} layer[132]. Full details of all device stacks and layers for the optimisation are shown in Figure 5.51.

Stack Descriptions

A	B	C	D
Ag (100 nm)	Ag (100 nm)	Ag (100 nm)	Ag (100 nm)
BCP-sol	BCP-sol	BCP-sol	BCP-sol
PCBM (20mg/ml)	PCBM (20mg/ml)	PCBM (20mg/ml)	PCBM (20mg/ml)
Al2O3-np	EDA/Al2O3-np	Al2O3-np	EDA/Al2O3-np
PVSK (3:1) 700 nm	PVSK (3:1) 700 nm	PVSK (4:1) 700nm	PVSK (4:1) 700nm
PEDOT:PSS	PEDOT:PSS	PEDOT:PSS	PEDOT:PSS
glass/ITO	glass/ITO	glass/ITO	glass/ITO

E	F	G	H
			Ag (100 nm)
	Ag (100 nm)	Ag (100 nm)	BCP (5 nm) evap
Ag 100 nm	BCP (5 nm) evap	BCP (5 nm) evap	C60(20 nm) - evap
BCP(5 nm)-evap	C60(20 nm) - evap	C60(20 nm) - evap	PCBM (5mg/ml)
C60(20 nm) - evap	EDA	PCBM (5mg/ml)	EDA
PVSK (4:1) 700nm	PVSK (4:1) 700nm	PVSK (4:1) 700nm	PVSK (4:1) 700nm
PEDOT:PSS	PEDOT:PSS	PEDOT:PSS	PEDOT:PSS
glass/ITO	glass/ITO	glass/ITO	glass/ITO

Figure 5.51 - Full description of all device stacks used for this optimisation. These stacks were designed to compare the evaporated contact C_{60} and BCP against the solution processed ETLs PCBM and BCP. The experiment also allows for the comparison of both conditions with and without passivation.

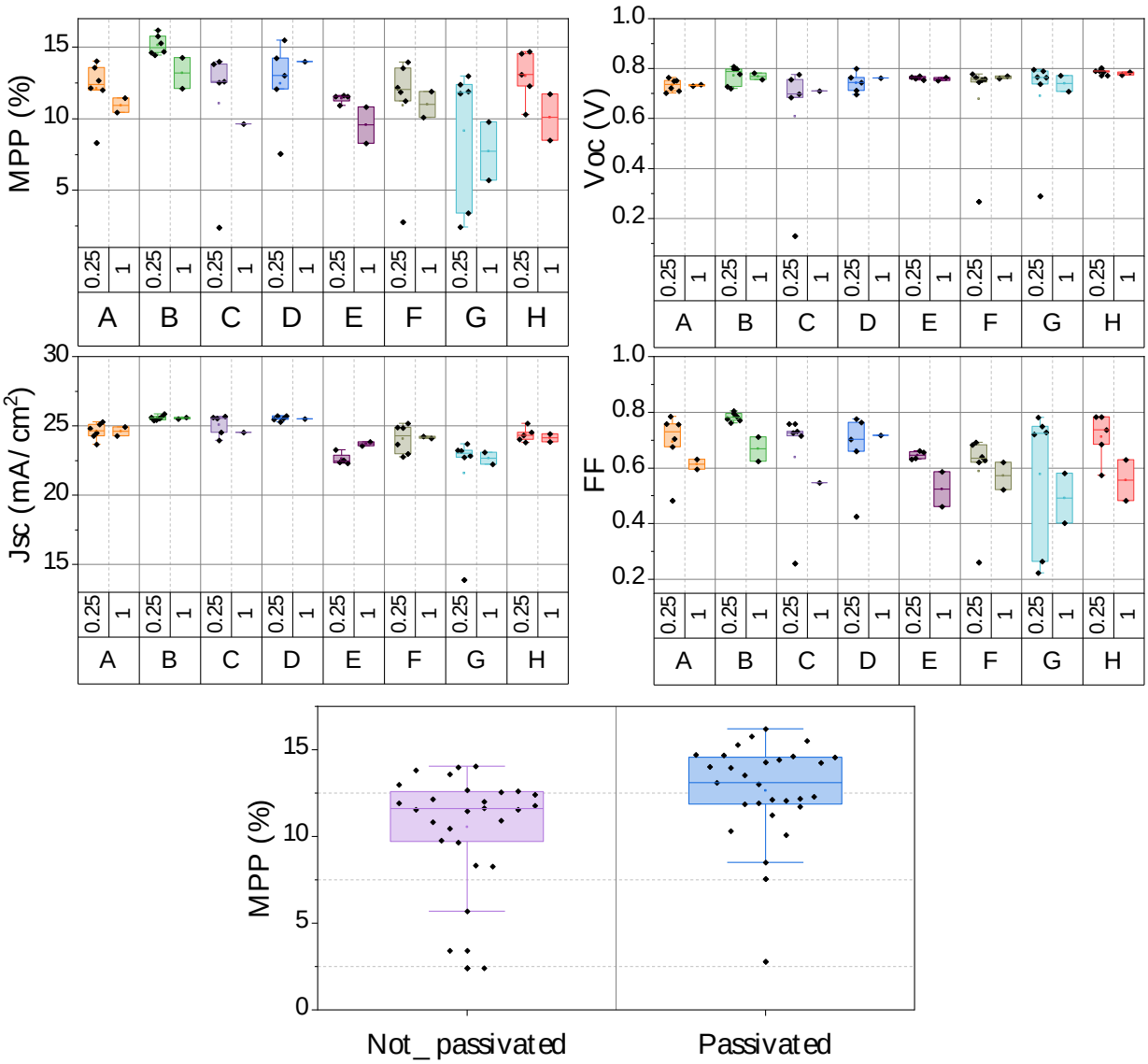

Figure 5.52 - All device metrics for the optimisation batch. At the bottom of the panel is the distribution in MPP for passivated and non-passivated cells. Devices are separated by device area, in cm^2, to highlight any differences in uniformity.

As shown in Figure 5.52, the single step passivation is successful in improving device performance by enhancing *Voc*. Champion devices for passivated and non-passivated cells are shown in Figure 5.53, and the metrics for the champions of all stacks are displayed in Table 5.7. Solution processed PCBM/BCP also outperforms both the spike structure and evaporated

C_{60}/BCP layers. This contrasts with the contacts usually selected for formamidinium/methylammonium (FAMA) perovskite blends. The position of the LUMO of C_{60} with respect to vacuum lies at -4.3 eV, PCBMs LUMO is closer to vacuum at -3.91 eV[133]. It is possible that replacing methylammonium for caesium at the A-site modifies the band structure, by changing the lattice volume or octahedral tilting, which can alter the overlap of orbitals (by altering the Pb-X bond length) that form the valence and conduction bands[134], such that the position of the conduction band makes alignment more favourable with PBCM for more efficient electron extraction.

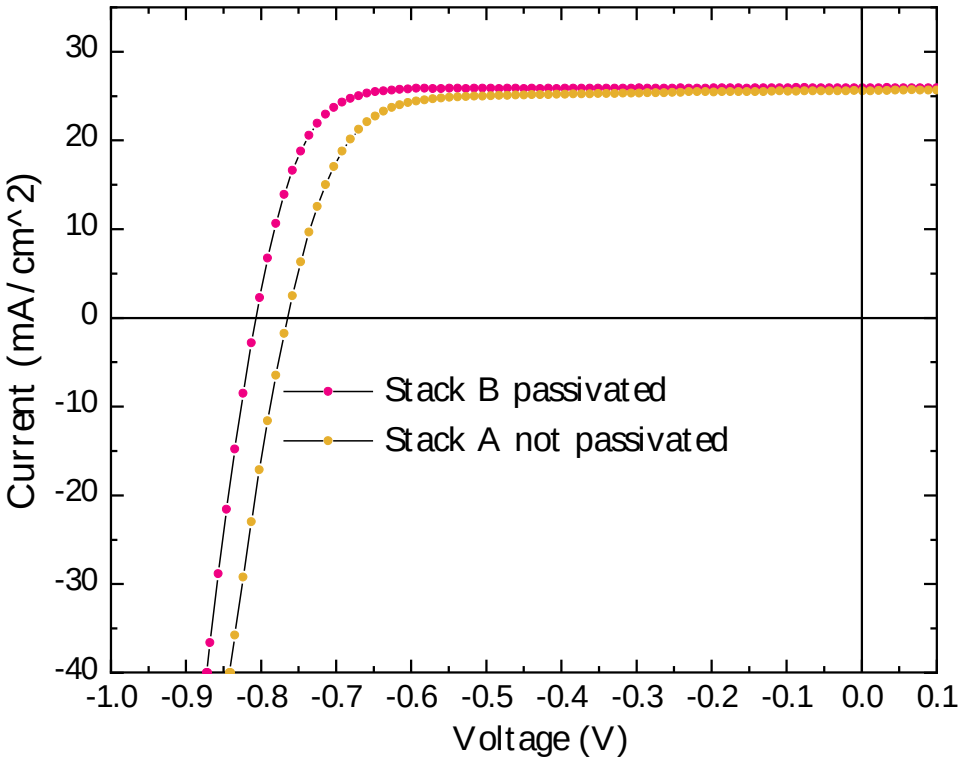

Figure 5.53 - J-V curves of champion cells from the passivated and non-passivated stacks. Both utilise PCBM. The passivation clearly improves the V_{OC} and R_{SH} of

devices giving a champion PCE of 16.84% for a 0.25 cm^2 device versus 14.84% for the control device of the same area.

Type	**Size cm^2**	**Passivation**	**PCE (%)**	**FF**	**Voc (V)**	**Jsc (mA/cm^2)**	**MPP (%)**
A	0.25	NP	14.84	0.76	0.76	25.12	14.05
B	0.25	Passivated	16.84	0.80	0.81	25.55	16.21
C	0.25	NP	14.85	0.76	0.76	25.61	14.01
D	0.25	Passivated	16.25	0.78	0.80	25.72	15.51
E	0.25	NP	12.24	0.66	0.77	22.53	11.63
F	0.25	Passivated	13.40	0.68	0.78	24.91	13.95
G	0.25	NP	15.06	0.78	0.77	23.70	12.99
H	0.25	Passivated	15.95	0.78	0.79	25.19	14.71

Table 5.7 – Showing the champion device metrics from each stack type. NP refers to cells that are non-passivated. The passivated champion cell shows a drastic improvement in V_{OC} and *FF*. PCE values are taken from forward scans.

5.2.4 Fabrication of the Optimised Tandem Batch

Despite various efforts to fabricate tandems in Oxford with the absence of a compact SnO_2 layer, none were successful across multiple batches, because of the solution processed top cell dissolving the bottom cell (a common solvent system was used for both). During this project, the group acquired an ALD system enabling the deposition of compact-SnO_2. This is a crucial replacement for BCP on the WBG sub cell as it gives much improved solvent resistance as it is a conformal oxide layer rather than a thin, small molecule layer that can be easily removed or infiltrated by solvents. The SnO_2 layer used in this study, was optimised by Dr Seongrok Seo, University of Oxford. Another important milestone came in 2019 when Lin *et al.* proved that 2T tandems could be successfully constructed without the use of a sputtered ITO interlayer[63]. Both updates allowed working *p-i-n* tandems to be constructed in Oxford for the first time.

With ALD-SnO_2 now available as an ETL and PbSn sub cell optimisation complete, a batch of tandem solar cells was created using the optimised parameters discussed in this chapter. Here the only variable of note is the comparison between 100 °C and 120 °C anneal as this was not investigated for single junctions previously and the effect temperature on the WBG sub cell needed to be investigated. Figure 5.54 displays the statistics for all devices made along with the champion J-V curves for both sub cells and champion tandem. Table 5.8 contains all the relevant champion device metrics.

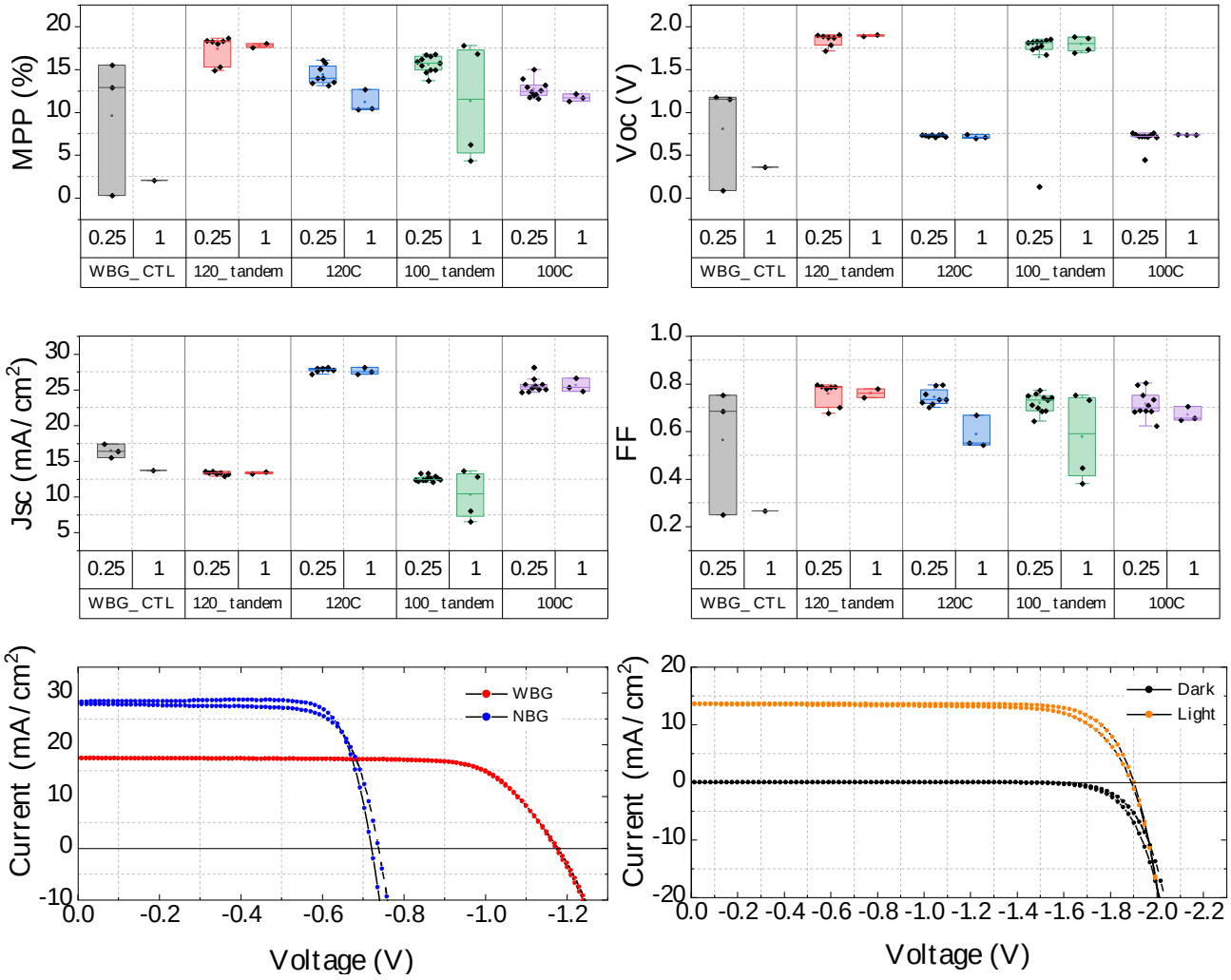

Figure 5.54 - Device statistics of the full batch of devices including controls. The bottom panel shows the champion control devices for NBG and WBG cells, and right, the champion tandem. Wide band gap cells and the SnO_2 layer were fabricated by Dr Seongrok Seo, University of Oxford. Device metrics are separated by device area to highlight any issues in uniformity. The champion PCEs for the 0.25 cm^2 control cells displayed are 16.08% and 15.47% for the NBG and WBG respectively. The champion efficiency for the 0.25 cm^2 tandem shown in orange is 20.63%. Champion values for all device types are shown in Table 5.8.

Variable	Area (cm^2)	PCE (%)	FF	Voc (V)	Jsc (mA/cm2)	MPP (%)
V1_tandem	0.25	18.25	0.74	1.87	12.88	16.74
V2_tandem	0.25	20.63	0.80	1.91	13.54	18.61
WBG_CTL	0.25	15.38	0.75	1.18	17.39	15.47
V1	0.25	16.25	0.79	0.76	26.45	14.96
V2	0.25	16.19	0.79	0.71	27.88	16.08
V1_tandem	1	19.52	0.75	1.88	13.64	17.75
V2_tandem	1	20.14	0.78	1.90	13.48	18.00
WBG_CTL	1	2.10	0.27	0.36	13.73	2.05
V1	1	13.30	0.66	0.74	26.62	12.12
V2	1	14.08	0.67	0.74	28.10	12.66

Table 5.8 – Champion values for all devices fabricated within the same batch shown in Figure 5.54. V1 and V2 represent devices annealed at 100 °C and 120 °C respectively.

The optimised batch showed a vast improvement over the previous 2T tandems. The voltage of both sub cells showed almost exact addition, when referencing the respective single junctions, to achieve a V_{OC} of 1.91 V for the 0.25 cm^2 champion. The larger 1 cm^2 is also able to achieve a MPP very close to that of the 0.25 cm^2 indicating good uniformity across the substrate. This

also indicated that the shunt issue of the previous tandem batch had been resolved. A drop off from the 20.63% scanned efficiency of the champion tandem down to its MPP value could be due to the hysteresis observed in the PbSn cells as shown in Figure 5.54. This could be resolved by optimising the deposition parameters and antisolvent drop time for tandem architectures as the substrate now differs from the single junction, meaning crystallisation of the perovskite layer may also be altered. The J_{SC} in the tandem cell is low in comparison to literature reports[60,62,63]. Increasing the thickness of the PbSn absorber layer would lead to improved absorption and an improved J_{SC}. The measured thickness of the PbSn absorber in this study is approximately 700 nm as measured by a Dektak profilometer. The concentration of the solutions used was 1.8 M. By increasing this to 2 M or greater, films approaching 1 μm commonly found in literature can be fabricated[135]. Achieving a *Jsc* of 30 mA/cm^2 in the PbSn junction, something commonly achieved in literature[55,136], would see the tandem J_{SC} increase to 15 mA/cm^2, resulting in an increase of efficiency to over 22% given the same V_{OC} and *FF*.

5.3 Summary and Outlook

To conclude, 2T- monolithic perovskite tandems in the *p-i-n* architecture have been successfully fabricated with excellent voltage addition to achieve a high V_{OC} of 1.91 V in the champion cell. The champion efficiency of the 0.25 cm^2 cell was 20.63% PCE with an MPP efficiency of 18.61%. This cell is almost four times larger than the best in class all-FACs tandem fabricated by

Palmstrom *et al.* with an improved V_{OC} and *FF* compared to their report[137]. For large area 1 cm^2 devices, a champion efficiency of 20.14% PCE and an MPP efficiency of 18.00% was achieved, this is highest PCE for a large area, all FACs *p-i-n* tandem to date. This was realised by removing shunt pathways in the lead-tin top cell facilitated by high temperature annealing and with a passivation strategy that combines a very low concentration of ethylene diamine with a dilute suspension of alumina nano particles. This provides the basis for further tandem work at the POD group in Oxford and confirms a working architecture and compact ALD SnO_2 ETL. The lower J_{SC} reported for these tandems versus their literature counterparts is due to the use of a thinner absorber layer in the PbSn sub cell. Increasing the concentration of the PbSn ink to greater than 2 M would be a straightforward way to resolve this issue. With an improved J_{SC} of 30 mA/cm^2 and the same *FF* and V_{OC} achieved in this batch, tandems with an efficiency over 22% PCE could possibly be fabricated. Optimising the deposition process to remove hysteresis will improve the stabilised MPP and bring it closer to the scanned value for PCE.

Chapter 6

Replacing DMSO - A Novel Lead-Tin Fabrication Route

DMSO has been shown to oxidise Sn^{2+} in solution to Sn^{4+} with elevated temperatures close to those used for annealing thin films[138,139]. In this chapter the removal of DMSO using a novel lead-tin precursor ink, that utilises dimethylammonium chloride (DMACl) to inhibit crystallisation of $FA_{0.83}Cs_{0.17}Pb_{0.5}Sn_{0.5}I_3$ thin films, is investigated. It is observed that crystallisation is slowed by driving the system through hexagonal polytype, intermediate phases before annealing. Upon annealing, specular, highly oriented thin films with enhanced grain sizes are formed with an optimum concentration of 40% of DMACl, with respect to the perovskite concentration. The resultant films are characterised by XRD, SEM, and 2D-XRD techniques. Following characterisation, devices are fabricated and tested for their ambient stability. The resulting champion device has enhanced ambient stability, remaining at 80% of its initial efficiency, four times longer than the device utilising DMSO.

6.1 Introduction

Both the long-term stability and fabrication of tin(II) (Sn^{2+}) containing perovskites remains a key challenge to their application in functioning photovoltaics. Narrow band gap (NBG) Sn-perovskites suffer from rapid crystallisation due to the fast reaction of Sn^{2+} with formamidinium iodide (FAI) and caesium (Cs) and degradation due to oxidation[140]. The main route to slowing down this rapid crystallisation process is to add DMSO as a co-solvent due to its highly coordinating ability and high boiling point. Smooth, specular, and pin-hole-free films can be then fabricated resulting in high performing devices, which is difficult to achieve with DMF as a standalone solvent[141]. However, Makhsud *et al.* first reported that DMSO can act as a powerful oxidising agent causing Sn^{2+} to oxidise to Sn^{4+} in solution. This report was followed closely by a similar study from Pascual *et al.*[139]. The degradation and subsequent inclusion of Sn^{4+} into the perovskite lattice induces p-doping and trap states that negatively affect the performance and long-term stability of thin films and devices[50,90,142]. To this end the field has been searching for a DMSO-free system that can still produce high quality thin films with comparable morphologies[141].

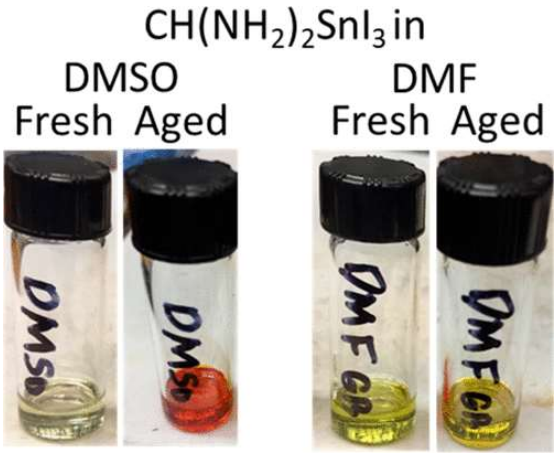

Figure 6.55 – Left: The oxidisation of Sn^{2+} to Sn^{4+} (clear to orange) in DMSO solvent. Right: No change of oxidation state when in neat-DMF solvent. Aging occurred at 120 °C for 5 hrs. Reproduced with permission from Makhsud *et al.*[138]

Inspired by the work of McMeekin *et al.,* who successfully removed DMSO by using DMACl to slow crystallisation in pure lead, $FA_{0.83}Cs_{0.17}Pb(I_{0.6}Br_{0.4})_3$ perovskites, DMACl was chosen to replace DMSO for fabrication of $FA_{0.83}Cs_{0.17}Pb_{0.5}Sn_{0.5}I_3$ films and the properties of the resulting films were analysed.

6.2 Results and discussion

6.2.1 Assessing thermal stability of DMACl inks

As an initial study, the solution ageing experiment by Makhsud *et al.* was repeated with the addition of SnF_2, which is found in most PbSn inks and has been demonstrated to be essential for high performing PbSn-based perovskite devices[63] (but was not included in the previous study) and the addition of DMACl to assess their impact on this process. Four solutions were prepared, and the conditions used in the study were recreated with the additions as shown in Table 6.9. In this chapter the DMACl concentration is referred to as a percentage with respect to the concentration the of perovskite precursor. For example, the perovskite concentration used was 1.8M so 50% DMACl would represent 0.9M. Full details of solution preparation are in Chapter 3.

#	Label	Description
1	Control	FASnI3 0.5 M in DMSO
2	SnF_2	FASnI3 0.5 M in DMSO, 5% SnF2
3	DMACl	FASnI3 0.5 M in DMSO, 100% DMACl
4	SnF_2 +DMACl	FASnI3 0.5 M in DMSO, 5 mol% SnF2 100 % DMACl

Table 6.9 - The solutions used to repeat the oxidation experiment by *Makhsud et al.*[138]

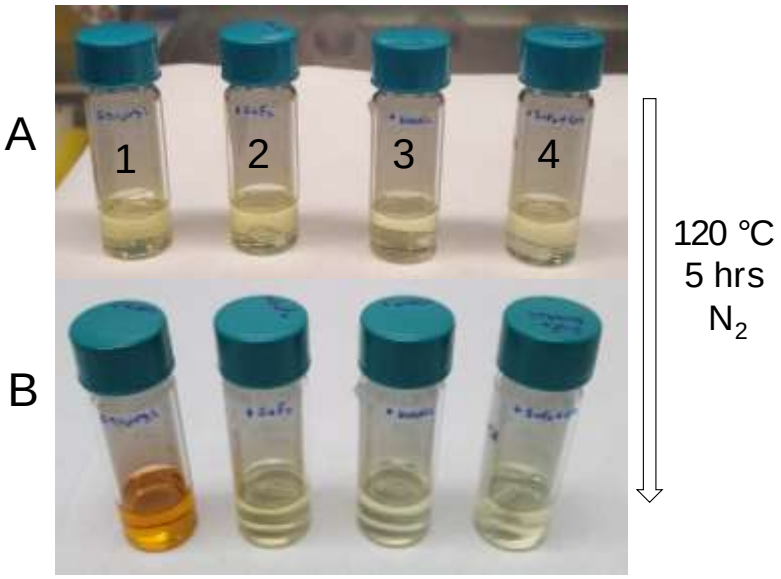

Figure 6.56 – A) Solutions as prepared at room temperature B) Solutions heated at 120 °C for 5 hrs. The orange colour of the control in B indicates oxidation of Sn^{2+} to Sn^{4+}. DMACl and SnF_2 containing are unchanged by eye. Due to the lack of an available UV-Vis spectrometer during the experiment no further assessments were made. The numbers on each vial correspond to the solution number in Table 6.9.

By visually assessing the inks containing DMACl, it appears that it can effectively supress the oxidation of Sn^{2+} to Sn^{4+}, which may be beneficial for ink preparation in suboptimal high-oxygen environments. It is worth noting that the inclusion of SnF_2 into the precursor solution also effectively supresses oxidation by DMSO. This could be an indicator as to why SnF_2 is an essential addition to mixed-PbSn inks in order to achieve high performing devices.[58,63,130,143]

6.2.2 Initial film assessment

After several rounds of visual optimisation with a range of solutions from pure DMF to 100% DMACl specular thin film formation across the full series

was realised. It was found that thin films could be fabricated by a standard method using gas quenching instead of antisolvent quenching and by applying a stream of N_2 6 seconds into the spin cycle. Gas quenching allows crystallisation to proceed at a reduced rate compared with the use of an anti-solvent[144] and reduces the amount of solvent in the processing atmosphere, which may aid reproducibility. When inks containing more than 40% DMACl were deposited, the resultant films did not fully convert to a black 3D-perovskite phase when annealing at the control temperature of 100 °C (explored later in this chapter). Annealing films further for 15 minutes at 150 °C allowed the films to crystalise into a smooth, black film. However, for 50% DMACl content and above, films had a hazier appearance and were very transparent to visible light, an indicator of pinhole formation and incomplete coverage.

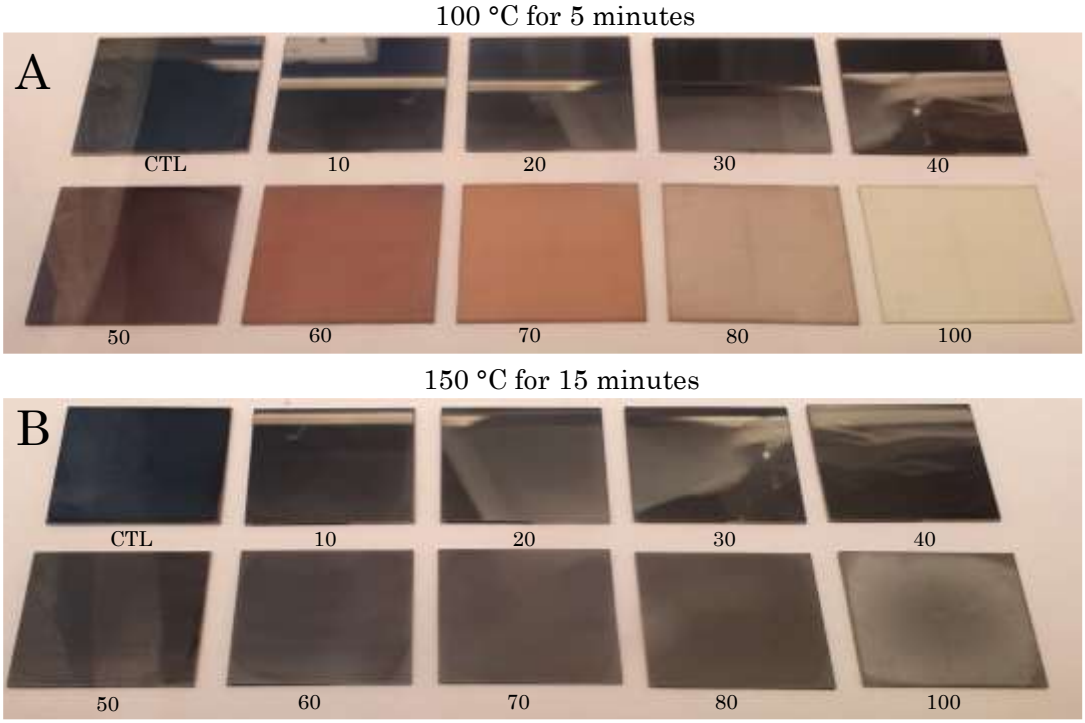

Figure 6.57 - A. Films annealed at 100 °C for 5 mins. Those with 40% DMACl and above did not convert to a black perovskite phase. B. The same films annealed at 150 °C for a further 15 minutes, films converted to the black phase within 1 minute at 150 °C.

6.2.3 The effect of DMACl on crystal structure

Following the successful fabrication of thin films from the DMF/DMACl solutions, the crystalline phases formed after annealing the $FA_{0.83}Cs_{0.17}Pb_{0.5}Sn_{0.5}I_3$ perovskite thin films were assessed by 1D-XRD. The optimised process was repeated to produce a new series of films on ITO substrates with the same range of DMACl as in the initial assessment. The resultant XRD patterns are shown in Figure 6.58. Initial observations showed that as the amount of DMACl is increased in the precursor solution, the intensity of the characteristic cubic perovskite peaks, the (100) and (200)

highlighted in Figure 6.58, increase in intensity relative to all other peaks, until a maximum is reached at 60 % DMACl. From 60% onwards the films have a hazy appearance accompanied by a lowering in intensity of the (100) peak. This is made clear in Figure 6.59 and Figure 6.60 below.

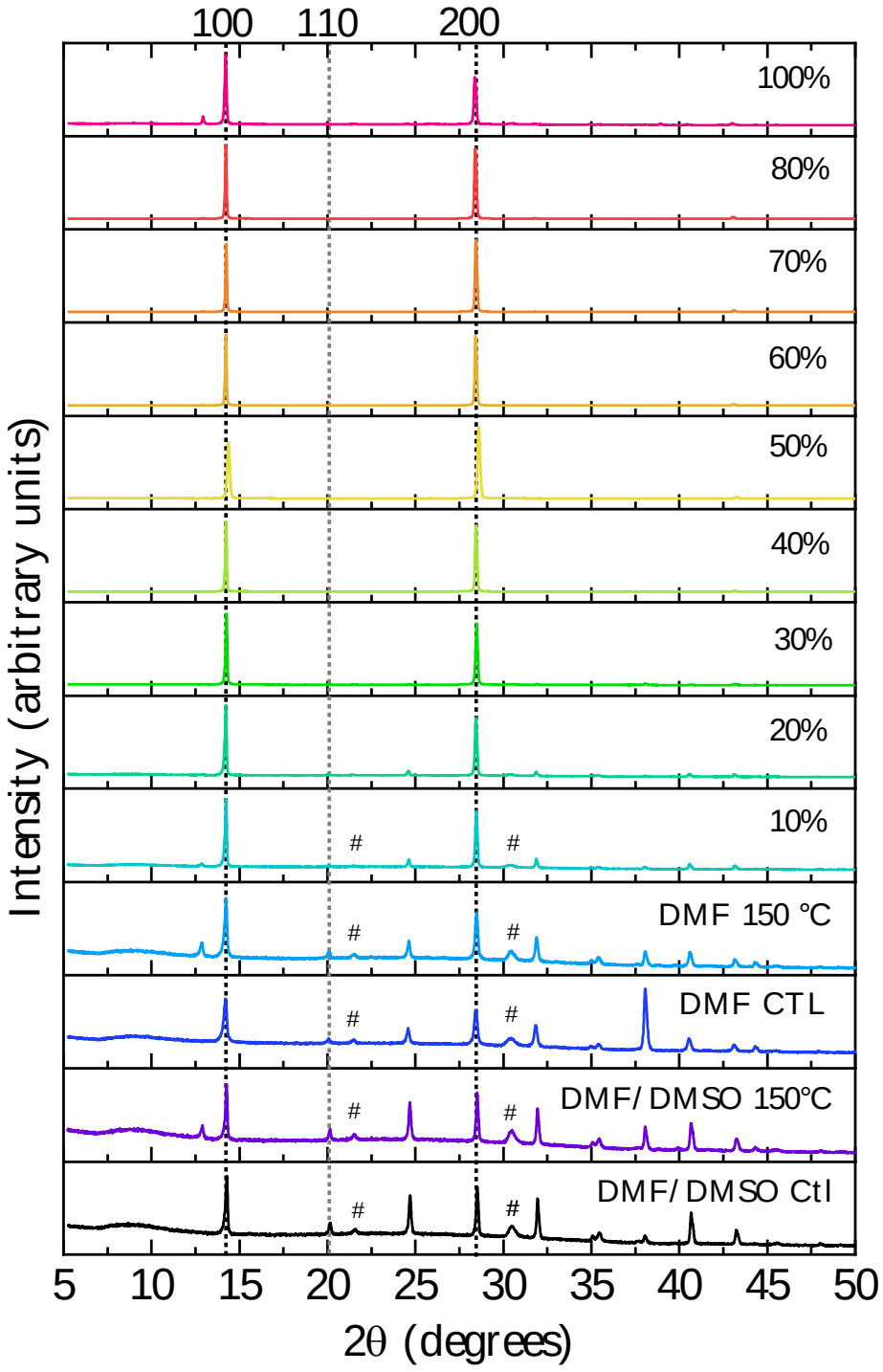

Figure 6.58 - The XRD patterns of $FA_{0.83}Cs_{0.17}Pb_{0.5}Sn_{0.5}I_3$ films with a range of DMACl concentrations in % on ITO substrates. ITO peaks are labelled with #. Intensity on the y-axis is scaled individually in each panel so (100) peaks can be clearly identified in each sample. The characteristic (100), (110), and (200) cubic

peaks are highlighted with dashed lines. 1D- XRD measurements in this plot were taken by Dr Christina Kamaraki, Oxford Photovoltaics.

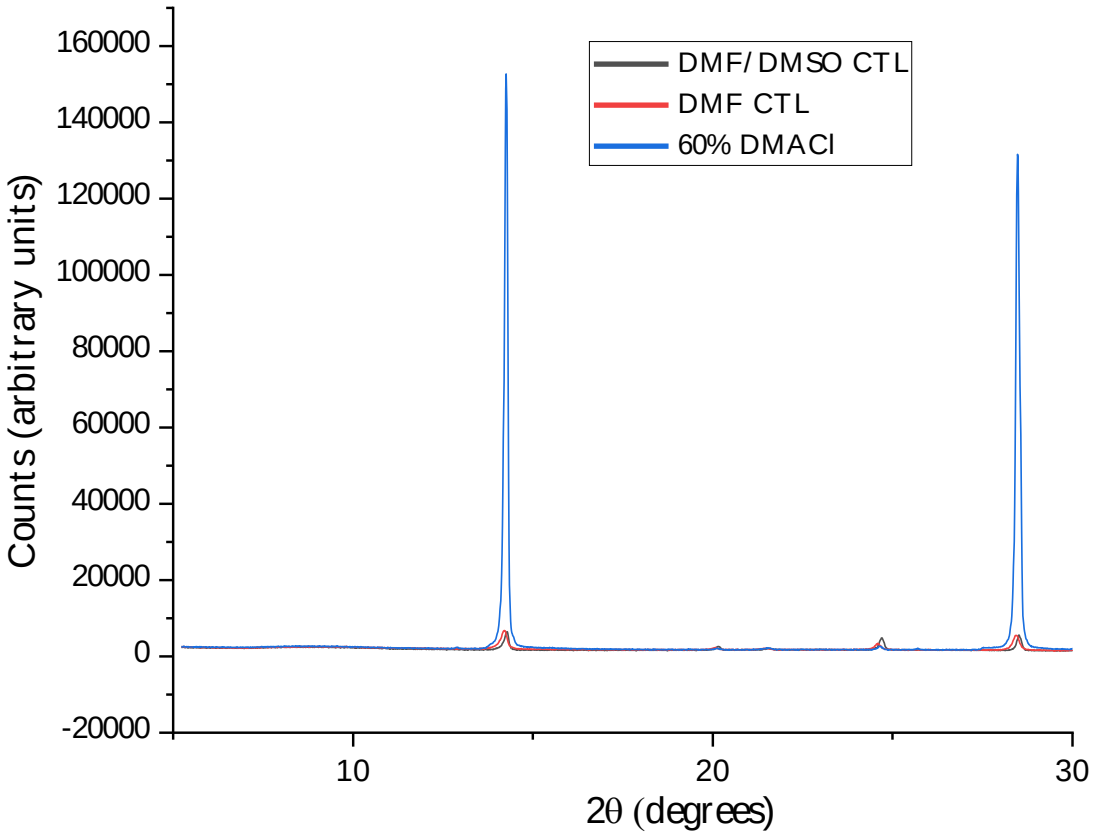

Figure 6.59 - The relative intensities for the 60% DMACl sample versus the two control films, DMF/DMSO and DMF only. The 100 and 200 peaks show intense diffraction versus the control samples.

The effect of orientation can be more easily distinguished across the series by plotting the ratio of the (100)/(110) peaks from each sample against the DMF only control sample as shown in Figure 6.60.

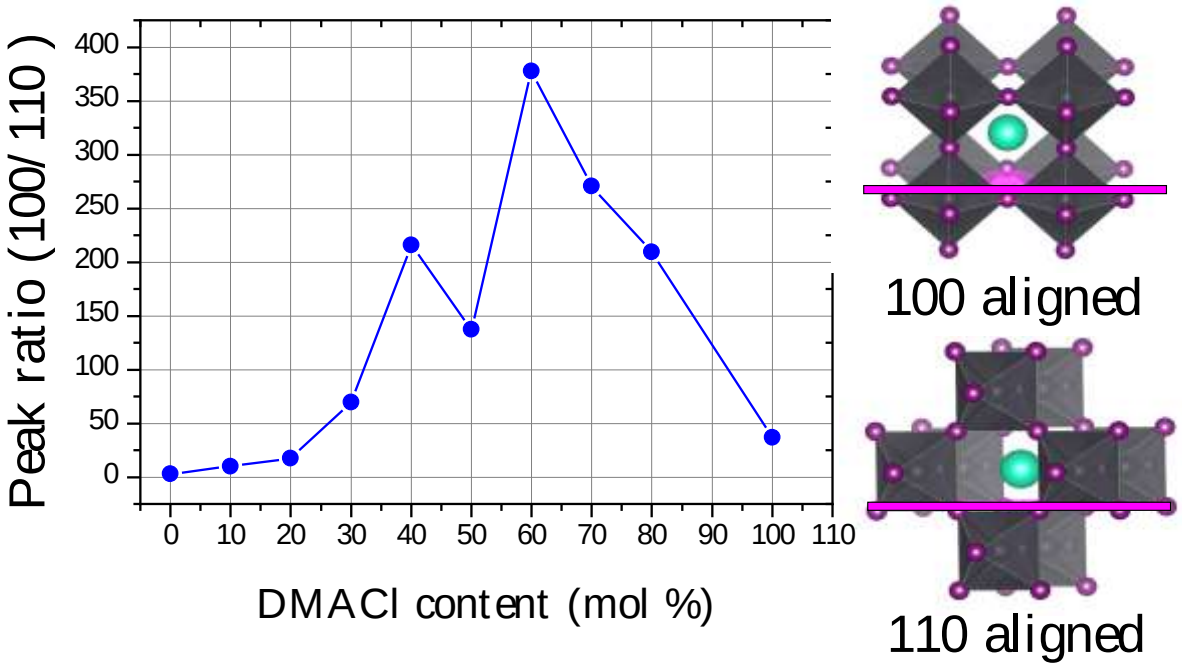

Figure 6.60 – Left: Showing the ratio of the (100)/(110) peak intensity of each sample across the series. Right: The general cubic perovskite structure with the (100) and (110) planes highlighted in lavender and oriented with respect to the substrate.

The large relative increase in (100) intensity, and subsequent bleaching of all other peaks, indicates that as the amount of DMACl in the precursor is increased the resulting films become more oriented with the (100) plane parallel to the substrate (Figure 6.60). The increase in orientation causes the (100) plane in the control films become barely visible on the same scale. This preferred orientation is depicted in Figure 6.61. There is a clear deviation from this trend at 50% DMACl content but it was unclear during the experiment what the cause of this could be and would require further investigation. Due to the less favourable morphology of the 50% DMACl film this was carried over into final devices.

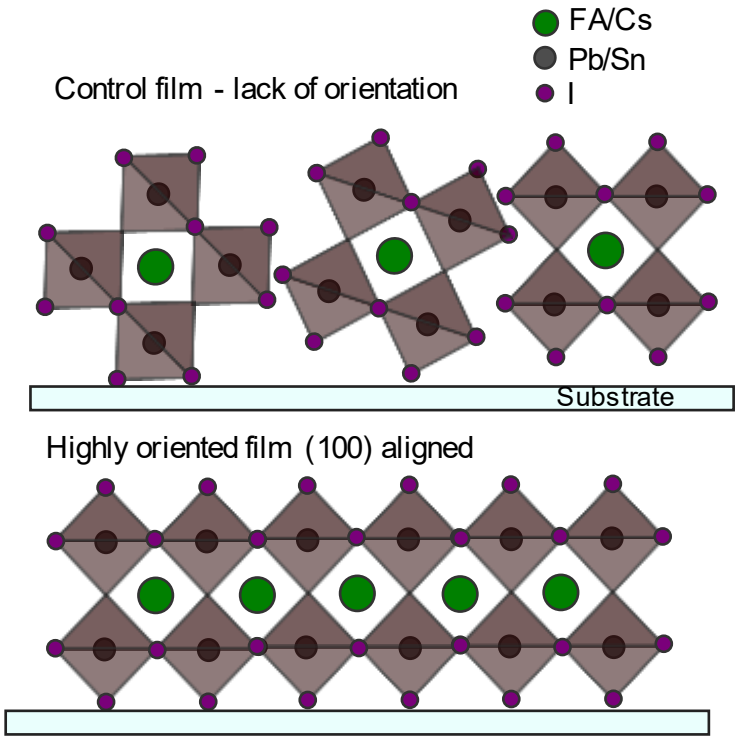

Figure 6.61 - An illustration to show the direction of orientation as deposited on a substrate and how this differs from the control film.

To corroborate the increase in orientation from 1D-XRD, a series of identical thin films was created focusing solely on the (100) plane by taking a snapshot of angles where this diffraction occurs using 2D-XRD. It is observed that as the percentage of DMACl is increased, the presence of complete Debye rings decreases. This loss of complete rings supports the hypothesis of a move away from a polycrystalline, randomly oriented film to films with an increase in orientation or texturing[145]. From both techniques we can conclude the film is in fact becoming highly oriented with the inclusion of DMACl.

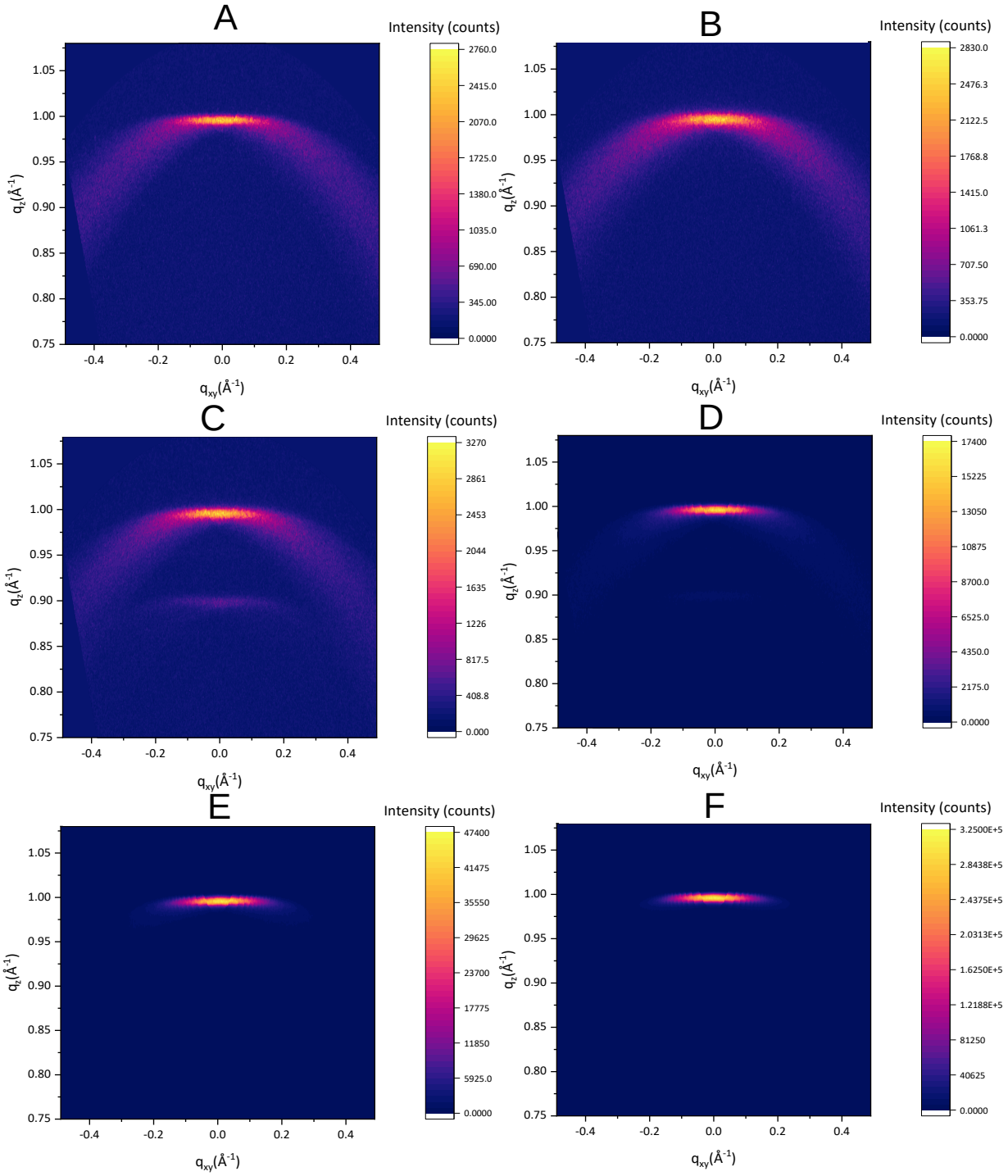
A
Intensity (counts)
2760.0
2415.0
2070.0
1725.0
1380.0
1035.0
690.00
345.00
0.0000
B
Intensity (counts)
2830.0
2476.3
2122.5
1768.8
1415.0
1061.3
707.50
353.75
0.0000
C
Intensity (counts)
3270
2861
2453
2044
1635
1226
817.5
408.8
0.000
D
Intensity (counts)
17400
15225
13050
10875
8700.0
6525.0
4350.0
2175.0
0.0000
E
Intensity (counts)
47400
41475
35550
29625
23700
17775
11850
5925.0
0.0000
F
Intensity (counts)
3.2500E+5
2.8438E+5
2.4375E+5
2.0313E+5
1.6250E+5
1.2188E+5
81250
40625
0.0000
q_z(Å^{-1})
q_{xy}(Å^{-1})
1.05
1.00
0.95
0.90
0.85
0.80
0.75
-0.4
-0.2
0.0
0.2
0.4

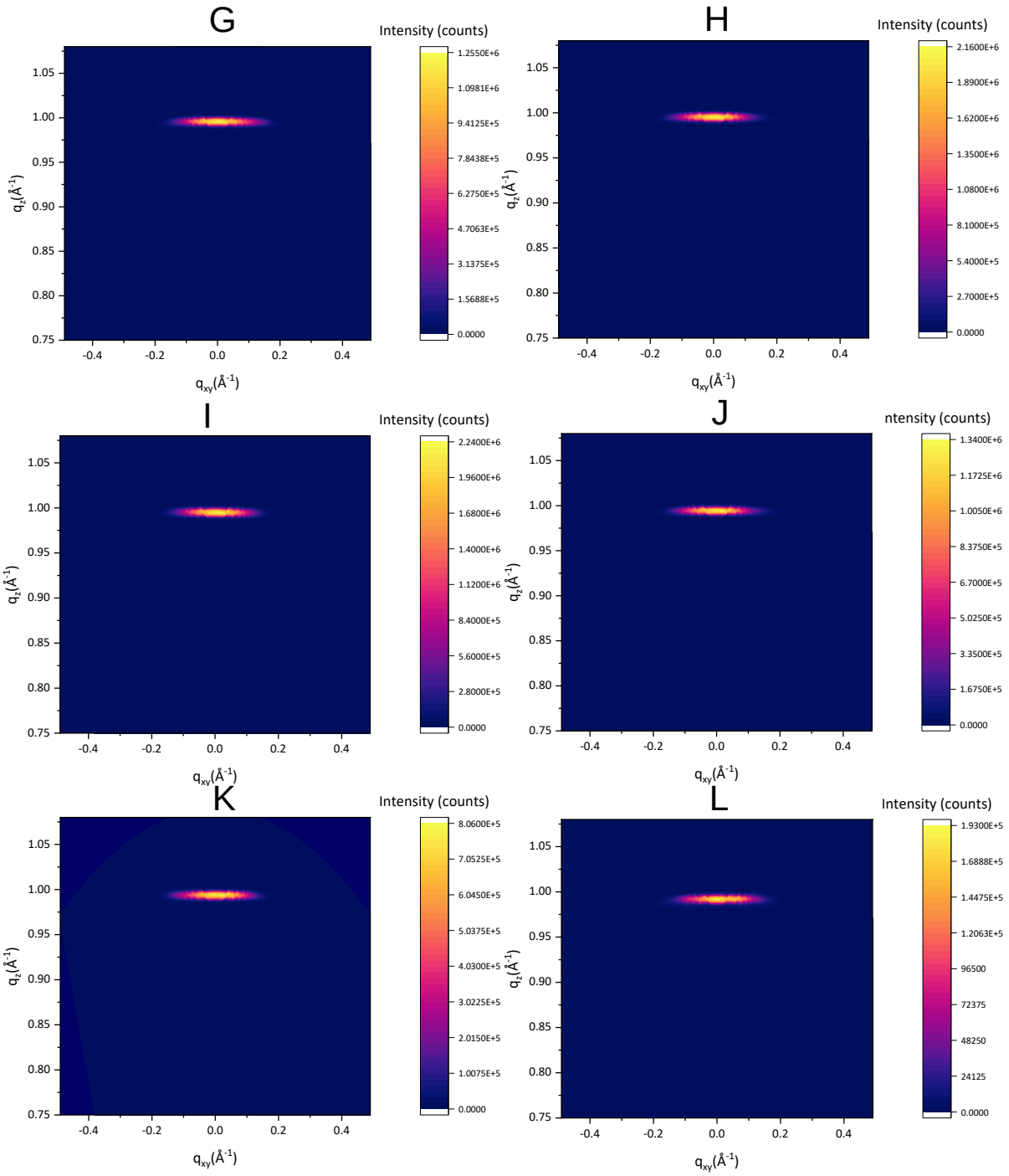

Figure 6.62 - A range of 2D-XRD diffractograms showing a snapshot of the (100) peak of each film. A) DMF: DMSO control film B) DMF control C) DMF annealed at 150 °C. D) - L) 10 - 100% DMACl. The reduction of the Debye rings for the (100) peak can be seen even at 10% DMACl, indicating an increase in orientation at low DMACl

concentrations. 2D-XRD patterns were measured and plotted by Philippe Holzhey, University of Oxford.

6.2.4 SEM imaging of half stacks

The XRD analysis revealed the orientation of crystal domains, but uniformity of final films is crucial for their application in devices. It is essential that films are free of pinholes, as this prevents shunt pathways between contacts[146]. To investigate film quality, thin films on glass/ITO/PEDOT:PSS substrates were fabricated and imaged using scanning electron microscopy (SEM). This sample configuration provided a conductive substrate to minimise charging during imaging with the SEM whilst also approximating how the active layer would grow in a device stack, as PEDOT:PSS is the hole transporter presently deployed in all state-of-the-art lead-tin devices[58,130,131,143]. The resulting films displayed in Figure 6.63 show a drastic change in morphology and grain size. In the control films that contain DMSO, grains are roughly 500 nm across but increase an order of magnitude to almost 4 μm in films that are still continuous between 20 – 50% DMACl. The DMF-only samples exhibited an undesirable morphology due to rapid, uncontrolled crystallisation consistent with literature reports[141]. At 10% DMACl, the film morphology shows a large quantity of pinholes. Crystallisation occurs too rapidly, producing films of incomplete coverage that are unsuitable for devices as discussed. Incomplete coverage reappears for concentrations of 60% and above. From the SEM analysis it can be concluded that films created from solutions containing 20-

50% DMACl would be the most suitable for device fabrication due to favourable film morphology.

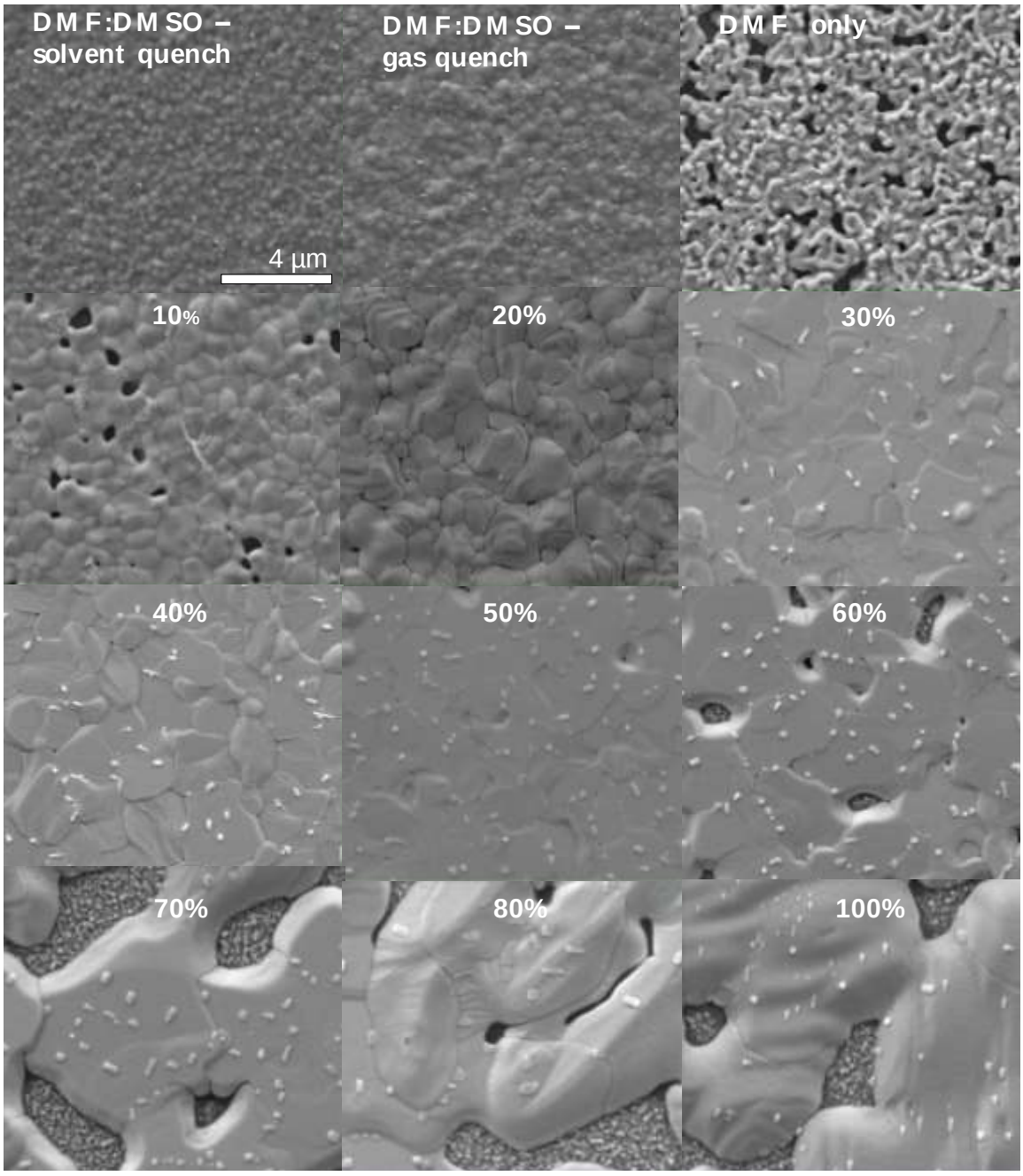

Figure 6.63 - SEM images of the entire range of DMACl films deposited on FTO/PEDOT: PSS substrates. Solvent vs. gas quenched DMF: DMSO films are also included and show similar morphologies. The scale bars are 4 µm in each image. The

incredibly rough regions seen underneath films at 60% DMACl and above is the underlying FTO surface. The small brighter particulates on the surface are assumed to be SnF_2.

6.2.5 Investigating intermediate phases

From the initial annealing experiments shown in Figure 6.57, at lower temperatures the final "black phase" perovskite was only formed in films with a DMACl content <60%. This effect was also observed by *McMeekin et al.* for the pure lead-based materials when DMACl was introduced. To investigate this, a series of films (shown in Figure 6.64), with the annealing step removed to halt crystallisation, was analysed using 1D-XRD as shown in Figure 6.66. It can be seen from these un-annealed films that instead of crystallising directly to the final perovskite phase, there is the appearance of several precursor phases that can be assigned to 2, 4, and 6 hexagonal polytypes (2H - 6H), as reported by McMeekin *et al.* and *Gratia et al.* where, instead of corner sharing BX_6 octahedra, there are now layers of face sharing BX_6 octahedra[147]. There is still a significant contribution from the cubic (100) peak that slowly diminishes in intensity as the amount of DMACl increases. This indicates that more of the precursor components are trapped in precursor states prior to annealing. This is also apparent by eye in the unannealed films from the change in colour across the series in Figure 6.64. A pictorial representation is shown Figure 6.65 of the well-documented polytypes that occur in Pb-based perovskite precursor phases[147].

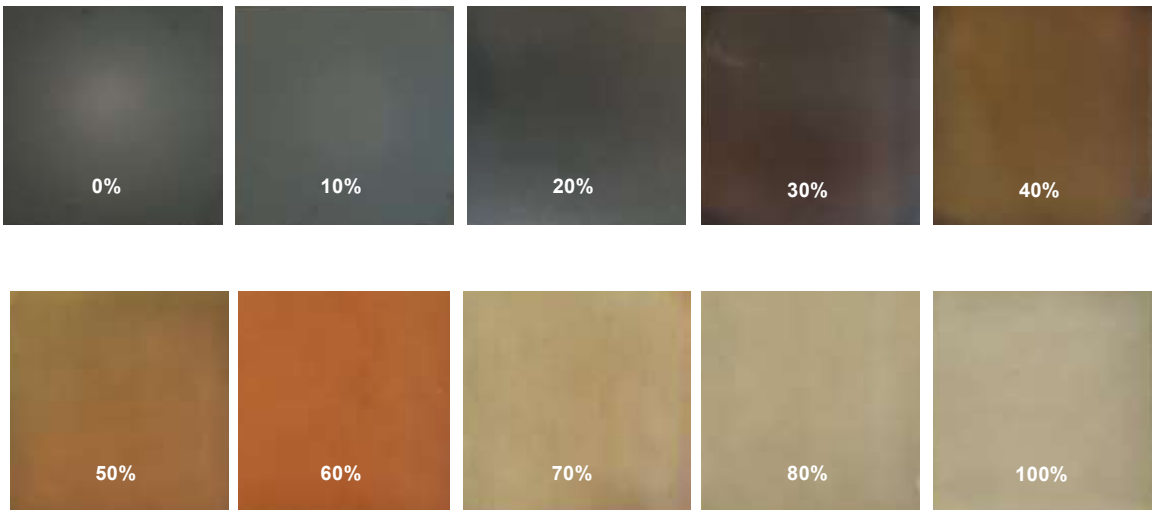

Figure 6.64 – Optical images of all films post-gas-quench with no annealing step. The colour change is evident across the series and is indicative of the presence of hexagonal polytypes[147].

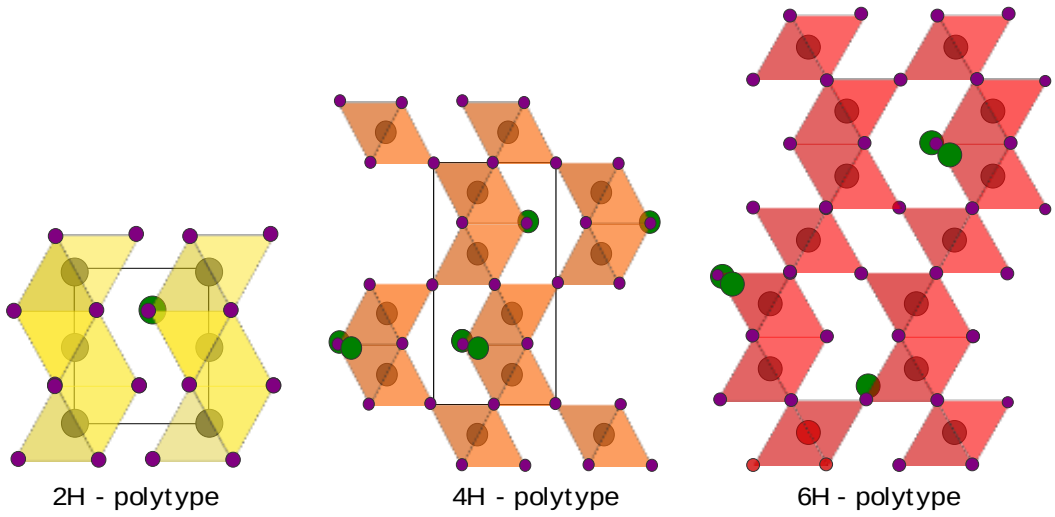

Figure 6.65 - Illustrative representations of the 2H, 4H and 6H layered polytype phases. It is postulated that DMACl causes these intermediate phases to form prior to annealing.

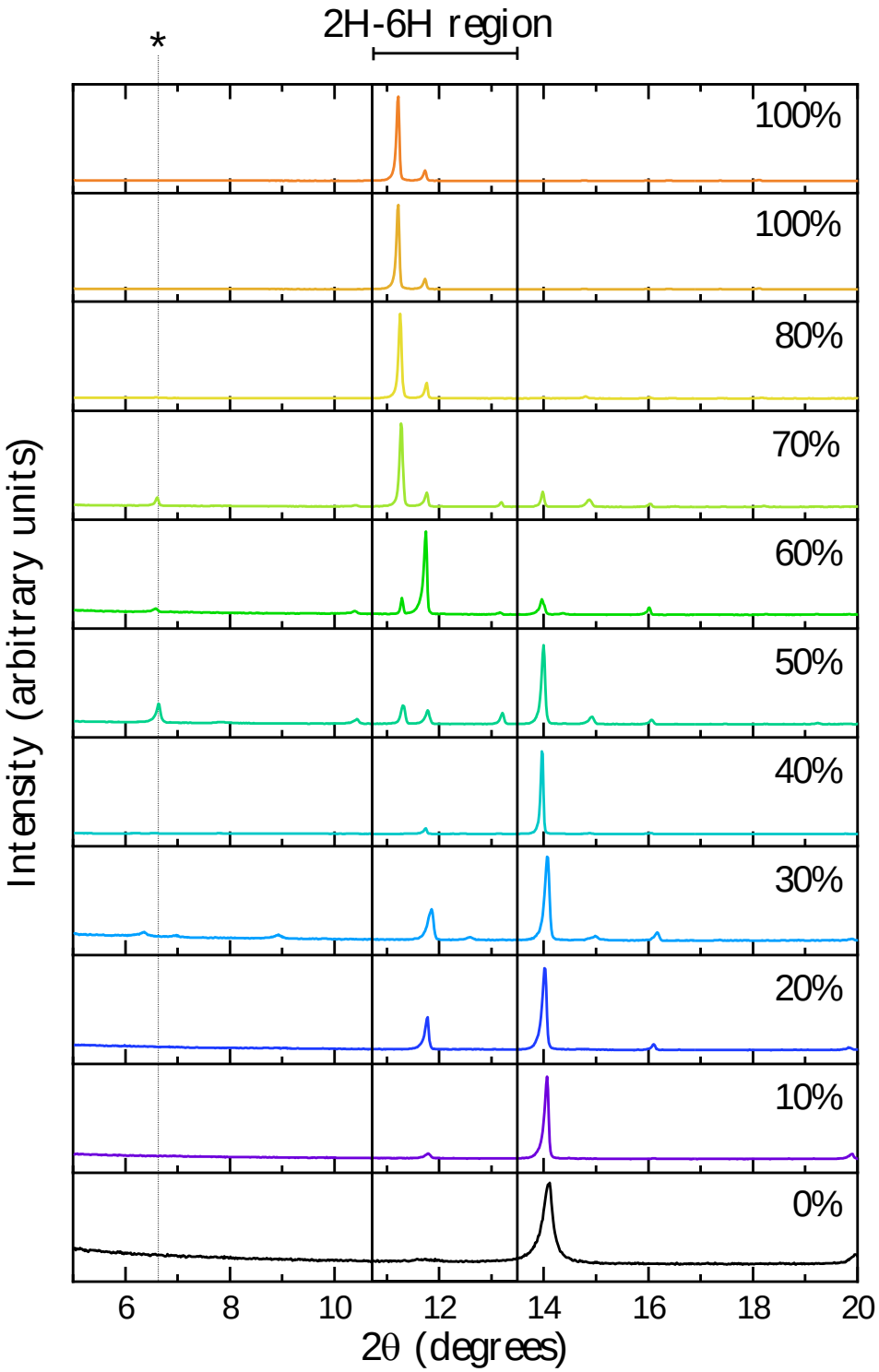

Figure 6.66 - 1D-XRD patterns of un-annealed PbSn films with a range of DMACl content. The boundaries from 2θ = 10.75 ° and 2θ = 13.5 ° highlight the region where the 2H-6H polytypes have been reported. *Indicates the presence of a new phase,

that is yet to be identified, in films of 50% DMACl and above. Intensity on the Y-axis is scaled individually to show the most intense peak in each panel so (100) peaks can be clearly identified in each sample.

Interestingly, the films that do not contain DMACl do not appear to go through a precursor phase but proceed directly to the cubic perovskite phase even without annealing. This is observed for films spun from neat DMF and DMF:DMSO mixtures, which is unlike the pure lead systems that crystalise via a DMSO-PbI_2 adduct[150,151]. This is a novel finding and has not yet been reported for lead-tin systems and could be a reason for their rapid crystallisation and issues with reproducibility. To investigate this further, *in-situ* Grazing-Incidence Wide-Angle X-ray Scattering (GIWAXS) was carried out for a film of 40% DMACl, DMF-only, and a DMSO control using gas quenching.

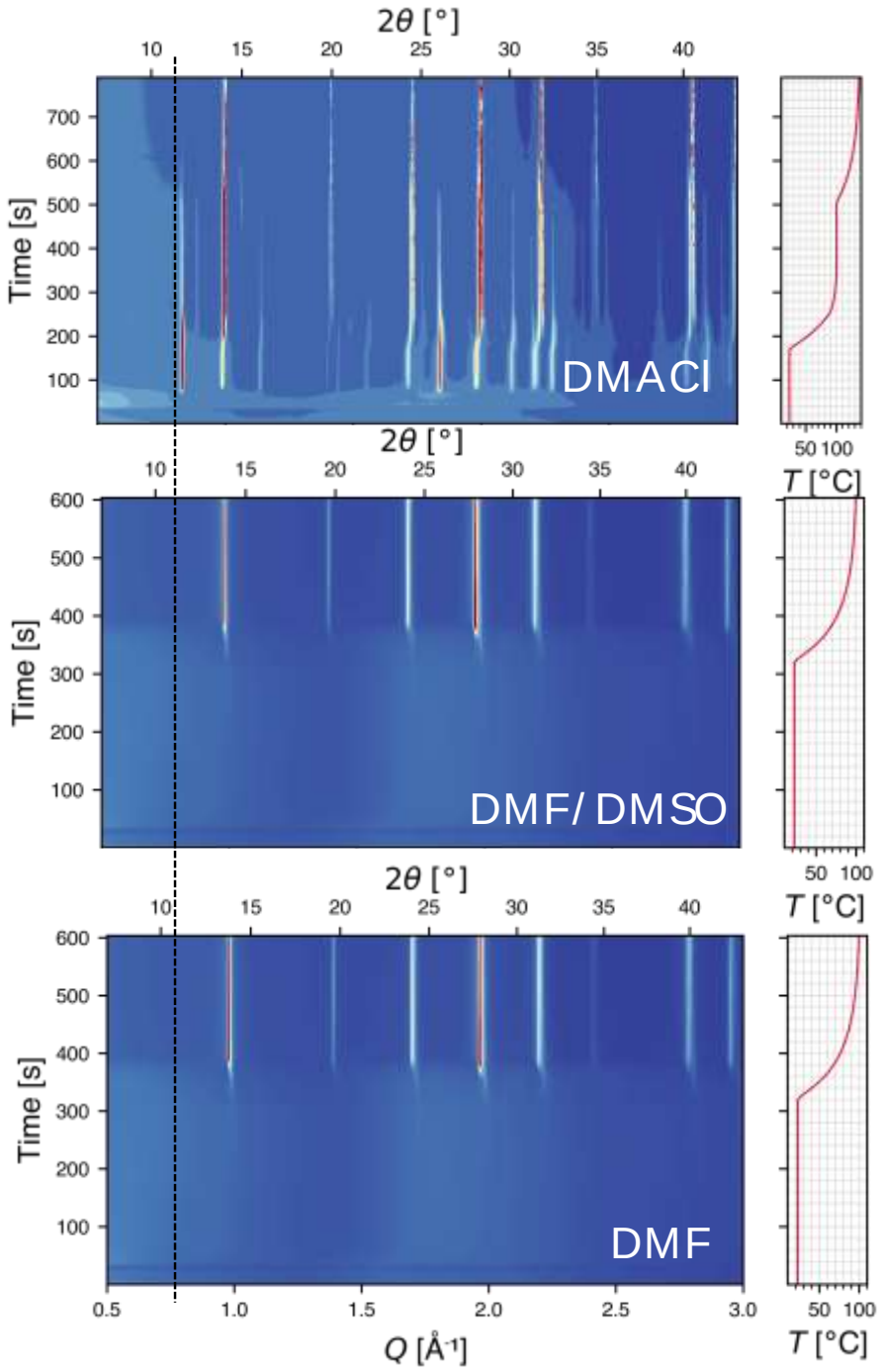

Figure 6.67 - *In-situ* GIWAXS plots for three samples. A) 40% DMACl. B) DMF:DMSO. C) DMF only. On the right of each plot is a temperature vs. time plot to show the annealing temperature of each film at various stages. The dashed line is placed to the left of a peak assigned to a 2H-polytype phase to guide the eye. This peak is not present in either control sample indicating the other two systems do not

proceed via this intermediate. The irregular heating profile seen in the DMACl sample was due to a brief error in thermocouple placement. GIWAXS measurements and plotting was performed by Dr Joel Smith, University of Oxford.

From the GIWAX data in Figure 6.67 an intermediate phase, assigned to the 2H-polytype at ~11.8°, is clearly seen but not visible in the DMF-only and DMF/DMSO phase and there are several other peaks that have not been assigned. However, these disappear during annealing much like the 2H-polytype peak. The lack of intermediate phase for the DMSO containing film is surprising, as discussed, given that the pure-Pb analogues go through an intermediate caused by a DMSO-PbI_2 adduct[150]. This could be a factor in batch-to-batch reproducibility for $FA_{0.83}Cs_{0.17}Pb_{0.5}Sn_{0.5}I_3$ thin films with crystallisation proceeding rapidly even with DMSO present. The inclusion of DMACl slows film crystallisation, and it is highly likely this is the cause for the increase in orientation and enhanced grain size. Following the assessment of this precursor phase, devices were made using the optimised gas quenching process for the entire range of DMACl percentages, including DMF-only. Two DMF/DMSO controls were also fabricated, one using the same gas quenching method and one by the solvent quenching method.

6.2.6 Device fabrication

The SEM analysis showed a region between 20% and 50% DMACl having favourable film morphology. Devices were constructed across the entire range to corroborate this finding and to find an optimum concentration.

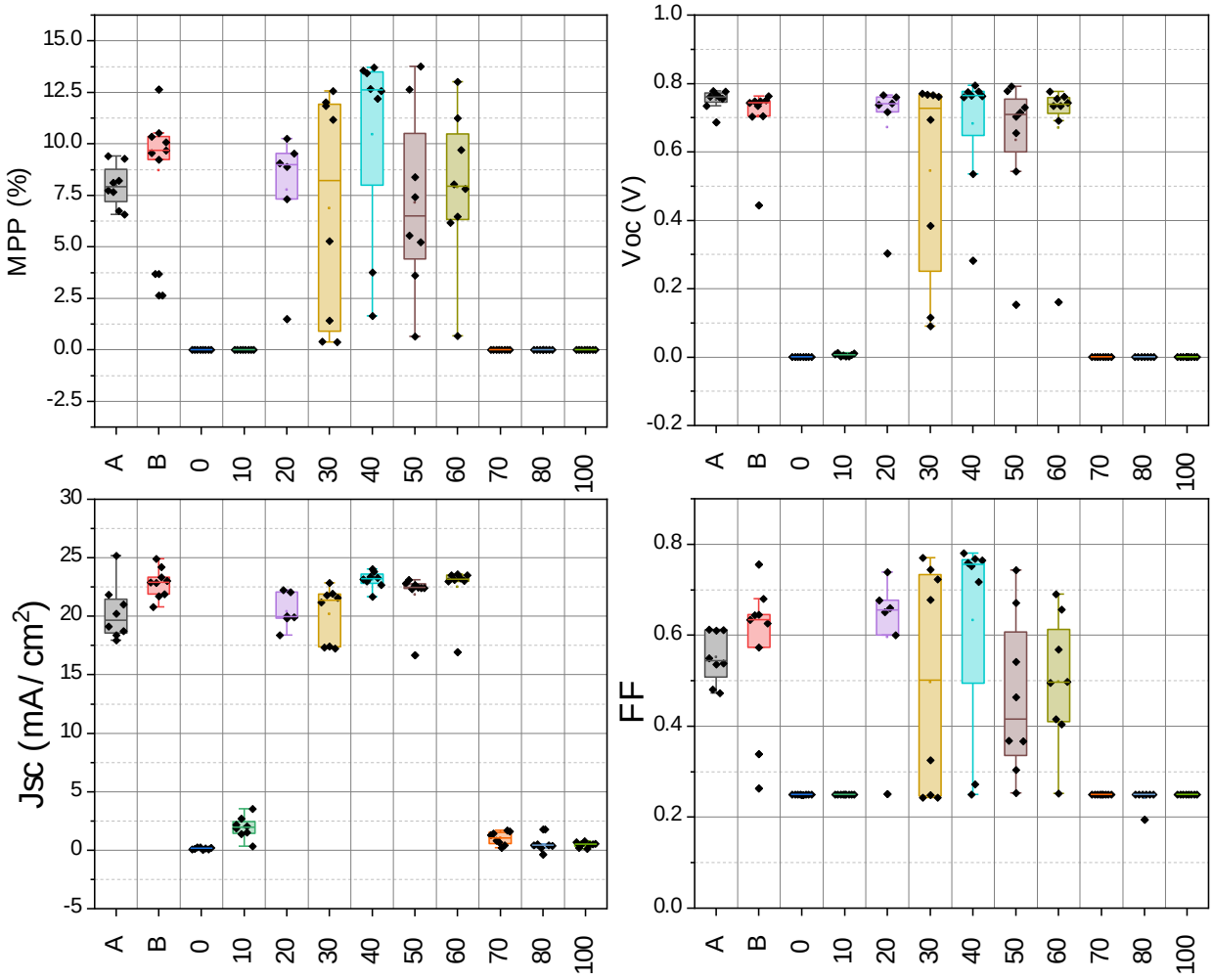

Figure 6.68 – Device metrics for the full range of DMACl excess. The highest median efficiency occurs at 40% excess of DMACl. A and B refer to controls made from DMF/DMSO that have been gas quenched or solvent quenched, respectively. The numbers on the x-axis refer to the percentage of DMACl. MPP represents the max power point tracked efficiency, over 60 seconds with the value being the final measurement point.

Figure 6.68 shows the statistics for a batch of devices spanning the full range of DMACl. The data from this batch showed that 40% was the optimum for devices, which is attributed to a superior morphology. Functional devices can still be made from 60% DMACl despite the poor morphology seen in SEM images. There is a slight band gap shift in devices observed from plotting dEQE/dE versus E from representative devices as shown in Figure 6.69. It is unclear why this slight shift occurs from 1.27 eV to 1.34 eV from the characterisation of the compositions and could be due to octahedral tilting induced by remaining DMA[152]. However, this band gap still falls within the ideal region of 1.1 – 1.35 eV for a narrow band gap absorber in a 2T tandem all-perovskite tandem[64].

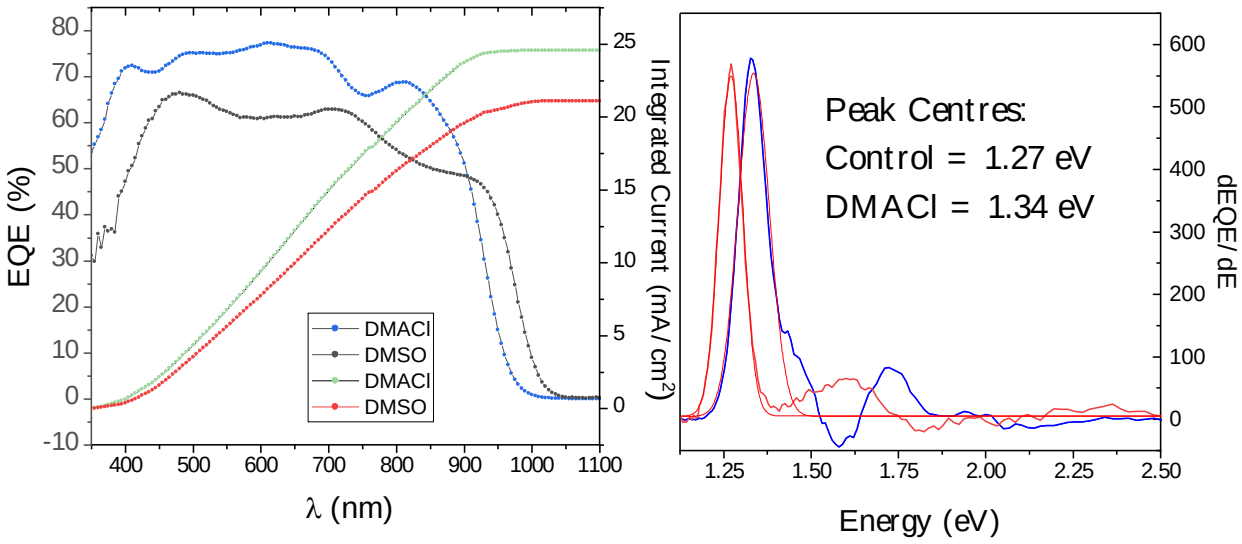

Figure 6.69 – EQE and dE/dEQE plots for representative devices of each composition. Peak centres were extracted from Gaussian fits to the plotted peaks. These devices were not fabricated in the same batch due to connection issues with the EQE setup but are representative of the control devices for each recipe.

Due to the high temperature required to anneal DMACl modified films, and the effect this may have had on the underlying PEDOT:PSS layer, the annealing temperature and its effect on devices was investigated with a second set of devices. Temperatures of 120 °C, 150 °C, and 170 °C were used to encompass the optimised control temperature, the film fabrication temperature, and a higher temperature, respectively. The performance statistics for this batch are shown in Figure 6.70.

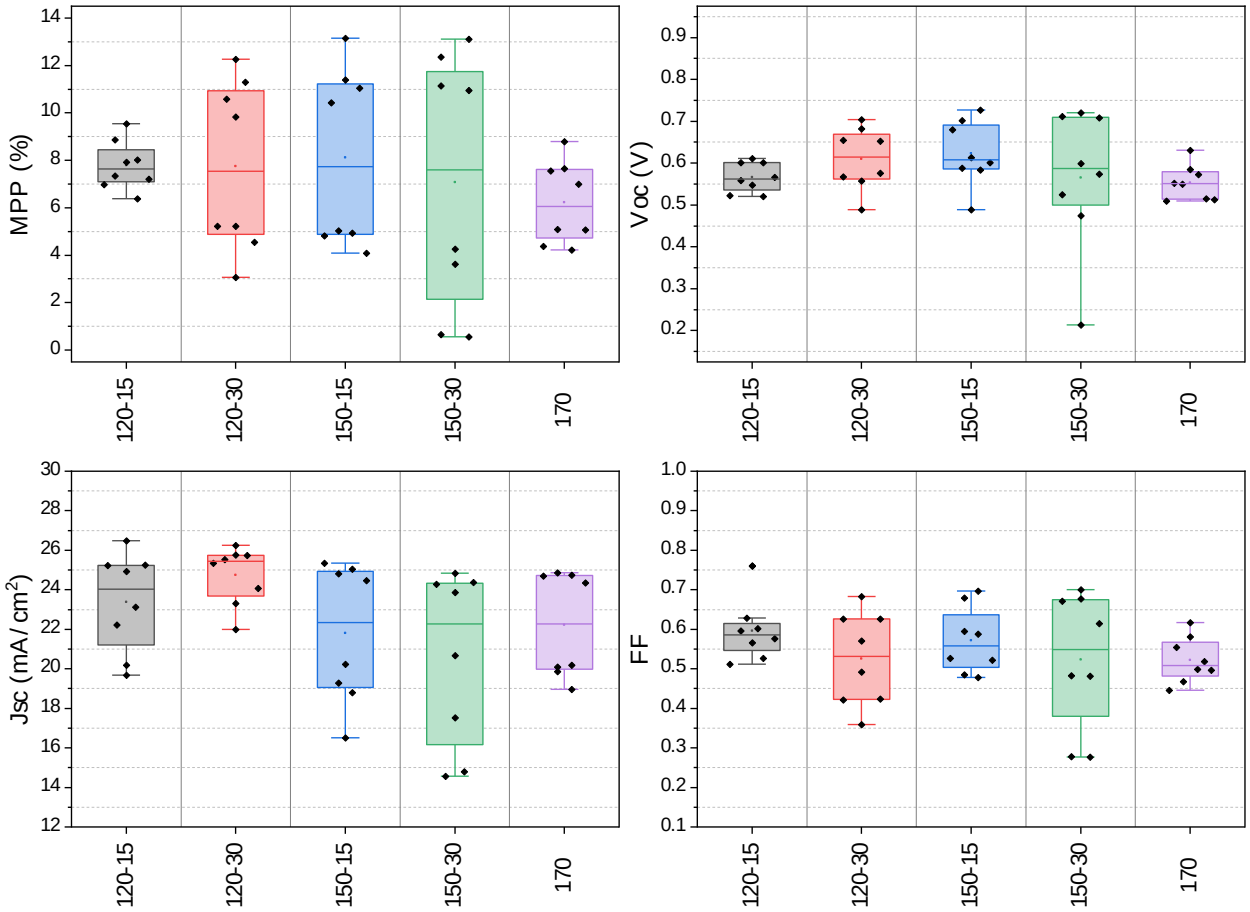

Figure 6.70 – Statistics for the temperature optimisation of the 40% DMACl modified $FA_{0.83}Cs_{0.17}Pb_{0.5}Sn_{0.5}I_3$ devices.

In all performance metrics except for J_{SC}, 150 °C for 15 minutes was the most effective. The reason for the drop of in J_{SC} is unclear. In retrospect, it would have been beneficial to repeat 1D-XRD analysis for the range of temperatures to see if any difference could be observed.

With the DMACl concentration and annealing temperature optimised, the focus for the next batch of devices was to test their ambient stability. Film ageing studies, whilst insightful, do not necessarily provide information about the stability of devices. The stability of lead-tin devices was investigated in 2020 by Mundt *et al.* and they observed a sharp drop off in performance over 200 minutes at 60 °C in ambient conditions. However, upon analysing XRD data of fresh and degraded devices, no changes to existing peaks or new peaks appeared in the resulting patterns. They conclude that the degradation occurs at the interface regions of devices far quicker than bulk degradation[153]. Ambient ageing was chosen as a more severe test than an encapsulated stress tests as O_2 is the main cause of oxidation in Sn containing films[154–156]. Further details of PbSn degradation can be found in Chapter 2.

A batch of devices was fabricated for both the optimum DMACl and DMSO containing films. In 2020, Werner *et al.* proved that DMSO could be effectively removed by gas quenching[91]. To decouple the effects of entrapped DMSO and the effects of film formation with DMSO the gas quenching method was used for DMSO control films.

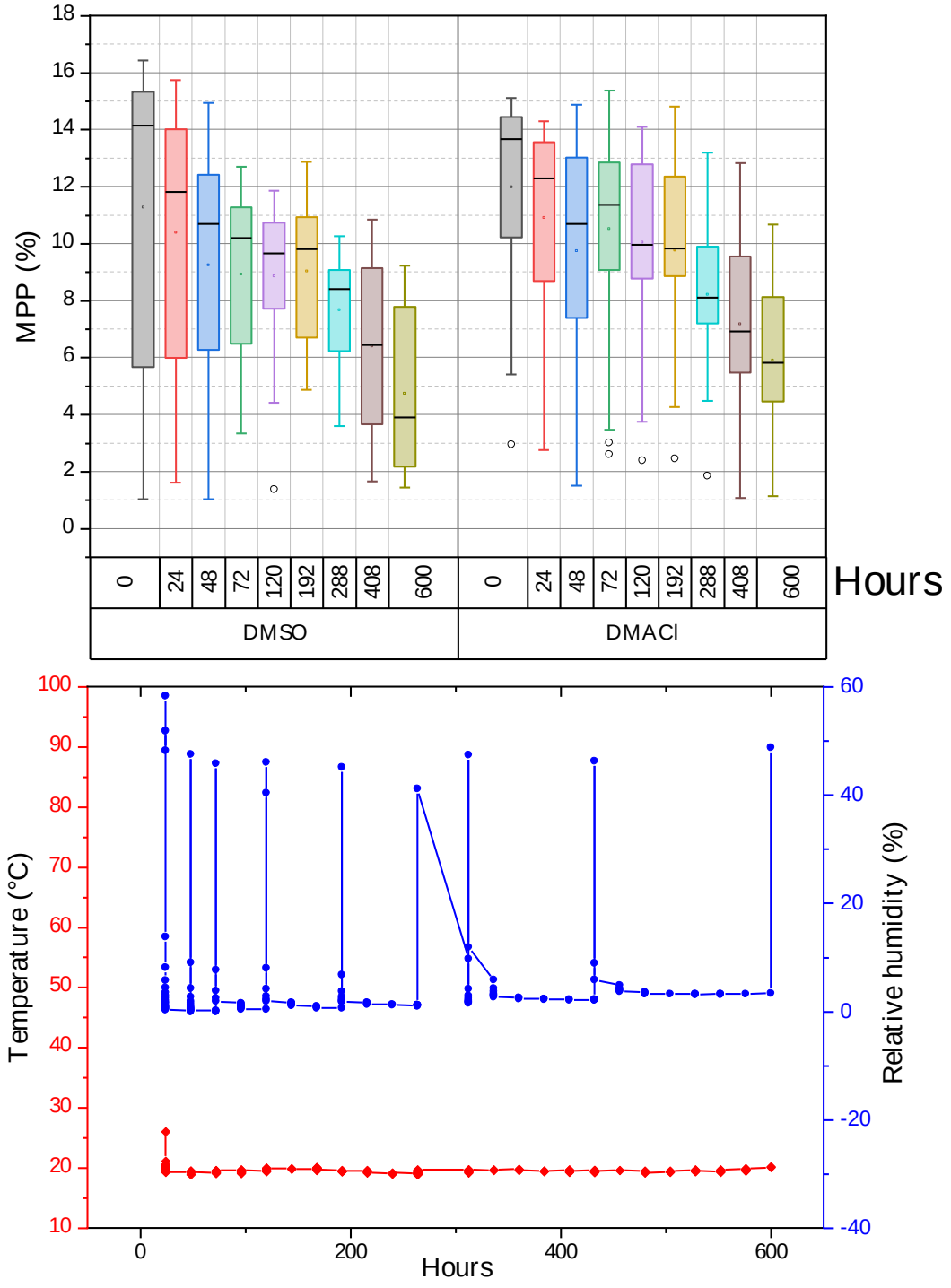

Figure 6.71 – Top: MPP versus days aged in air for 2 device populations of DMACl containing devices and a DMSO containing set fabricated in the same batch. Bottom: The temperature and humidity data as logged. Devices were kept in the dark over silica desiccant beads to decouple stability in air with stability towards humidity.

The spikes in humidity indicate when the storage box was open for device testing. The average humidity whilst stored was 2.3% RH and 47.2% when testing for approximately 1 hour/test. The temperature remained constant throughout with an average of 19.6 °C. Devices were unencapsulated.

There is negligible difference in the statistics for both device populations and can be visualised in Figure 6.72 where the median MPP values are plotted side by side. There is also a large spread in performance at the initial point of testing for all devices in this batch indicating sub-optimal processing conditions during fabrication. However, the champion cell from the DMACl showed a vast improvement in air stability. The DMSO containing device, whilst having a higher initial MPP, had a T_{80} lifetime (the time it takes to drop to 80% of its initial performance - a standard performance metric in the perovskite field[157]) of just 68 hours whereas the T_{80} for the DMACl containing device is 475 hours, a sevenfold increase in stability. From the J-V curves for the champion devices at 0 hours and 600 hours shown in Figure 6.73, the DMACl sample appears to be losing current over time but still has good diode characteristics and a slight drop in V_{OC}. The DMSO sample has an increase in *Voc* accompanied by a drop in current that is attributed to an extraction barrier forming at one of the contacts, effectively boosting V_{OC} by allowing charge carriers to build up while simultaneously blocking charge extraction.

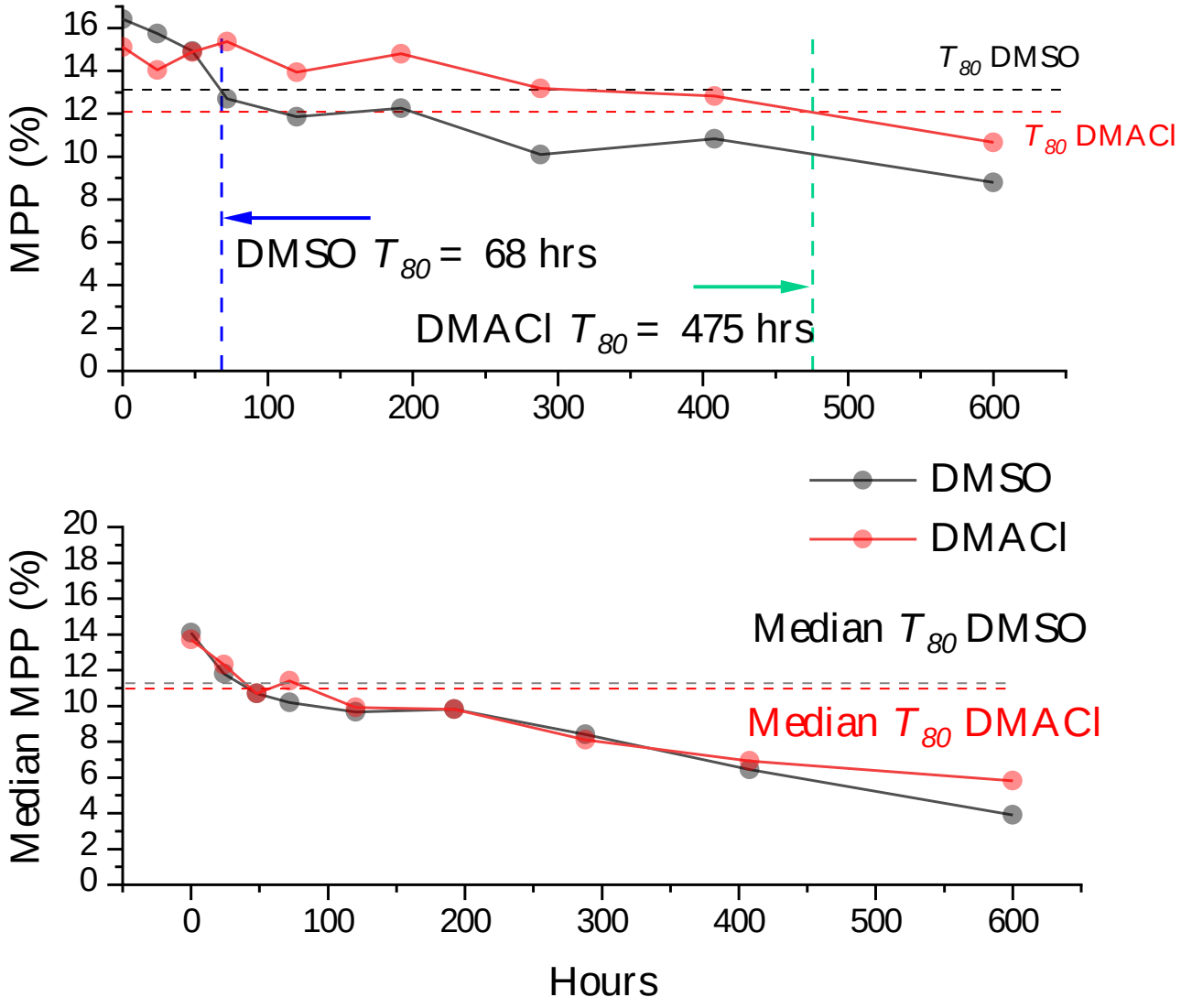

Figure 6.72 - The top panel showing the MPP over time for aged champion, unencapsulated, devices of DMACl and DMSO in dry air. The bottom panel shows the median MPP for each batch plotted as function of ageing time. The T_{80} lifetimes are highlighted for each sample.

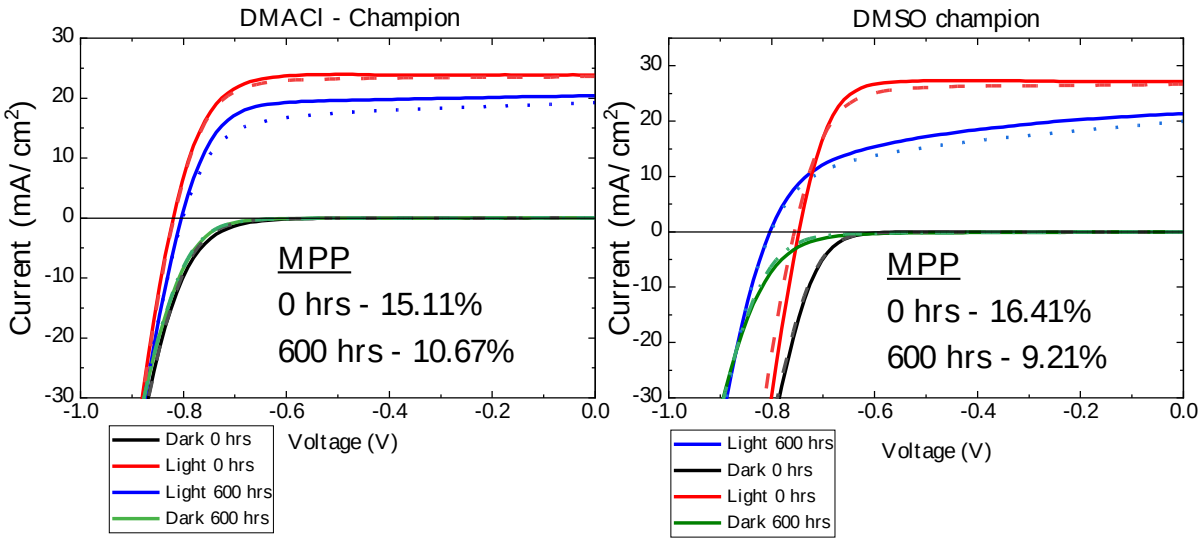

Figure 6.73 – J-V curves for the champion cells for each batch, identical to the cells shown in Figure 6.72. The DMSO sample appears to have an increased R_{SH} and R_S whereas the DMACl seems to only drop in current and a slight drop in V_{OC}. J-V curves are from measurements that were taken at the start and end of the ageing study at 0 and 600 hours, representing devices well past their T_{80} points.

6.3 Summary and Outlook

To summarise, through careful optimisation and material characterisation, a novel precursor formulation and thin film deposition route has been successfully used to replace DMSO in the precursor solution for PbSn. It is found that this is enabled by the formation of intermediate polytype phases prior to annealing that do not occur in films of DMF-only or DMF/DMSO, which is a new observation. The optimum DMACl concentration of 40% in DMF allows for the formation of smooth, compact, and pinhole-free films with enhanced grain size, orientation, and ambient stability for a champion device. These features are attributed to the large nature of the grains. It is postulated

that this inhibits the amount of ingress points for oxygen, slowing degradation. The median MPP as a function of ageing shows negligible difference between the two device populations presented but this could be due to sub-optimal processing conditions as there is a larger performance spread than should be expected for a batch of devices. However, the champion DMACl device had an impressive initial MPP of 15.12%, comparable to the established DMSO processing route that gave a champion MPP efficiency of 16.42%. The DMACl champion showed greatly improved ambient stability with a T_{80} of 475 hours versus the 68 hours recorded for the DMSO device. This work has provided a novel processing route for PbSn perovskites that could also be applied to neat-Sn thin films and may allow for less strict processing conditions. Future work should further characterise the precursor phases and investigate the degradation of DMACl modified films, which was outside the scope of this study. Focus should be made on full spin coating optimisation of this blend to improve baseline performance toward highly efficient cells with much improved stability.

Chapter 7

Conclusions and Outlook

The work in this thesis has focused on the narrow band gap perovskite absorber $FA_{0.83}Cs_{0.17}Pb_{0.5}Sn_{0.5}I_3$. Chapter 4 investigated several strategies to improve the photoluminescence quantum efficiency (PLQE) of the neat absorber and reduce non-radiative recombination at the interfaces with charge selective layers. Several thiocyanate additives were found to reduce non-radiative recombination within the bulk absorber whilst simultaneously increasing grain size and charge carrier diffusion lengths. However, when thiocyanate-modified materials were deployed into photovoltaic devices, a drop off in J_{SC} was seen for all additives. With the detection of unfavourable phases forming, shown by examining XRD patterns of companion films, it was postulated that these phases sit at the interface. This passivated the neat films, improving PLQE but reducing charge extraction at the interface with charge selective contacts. With promising PLQEs greater than those in the unmodified films and diffusion lengths much longer than that of the film thickness, it may be useful to optimise the concentration of these additives to investigate if a balance can be made between improved optoelectronic properties, and charge extraction for high-performing devices. The second half of the study focussed on the interface with charge selective contacts. Several hole transport layers (HTL) were screened as candidates to replace PEDOT:PSS. It was found that all could effectively reduce non-radiative

recombination in comparison to PEDOT:PSS with some outperforming the neat layer deposited on glass. Despite PLQE values equal to, or greater than, those for films on glass these HTLs showed a reduction in current density in devices. This was attributed to a known screening effect caused by mobile ions. This effect was less pronounced in PEDOT:PSS devices which may be due to its heavily doped nature. In the same study it was found that both fullerene-based electron transport layers, C_{60} and PCBM, introduce significant non-radiative recombination. The non-radiative recombination was reduced by inserting a thin layer of FASCN between the two materials, resulting in an enhanced V_{OC} in devices. This study highlighted significant losses at both interfaces and that careful selection of the HTL, and passivation is necessary to construct high-performing devices.

Chapter 5 focussed on the construction of 2T all-perovskite monolithic tandem solar cells. Initial batches highlighted an issue with the morphology of the PbSn sub cell in the form of pinholes and voids, confirmed by SEM microscopy. These microscopic defects caused sub cell shunts that resulted in low $V_{OC,}$ anomalously high $J_{SC,}$ and an s-kink in the diode's *J-V* curve. By altering the annealing method of the PbSn sub cell, these defects were no longer observed. Following this, a full-scale device optimisation was carried out. By combining these approaches, high efficiency 2T tandem solar cells were made resulting in champion PCEs of over 20% for both 0.25 cm^2 and 1 cm^2 devices, the latter being the highest reported 1 cm^2 all-FACs *p-i-n* tandem device to date.

Chapter 6 investigated the removal of DMSO in the precursor solution by using the ammonium halide salt DMACl. Addition of 40% DMACl, with respect to the perovskite concentration, sufficiently hindered the crystallisation of the $FA_{0.83}Cs_{0.17}Pb_{0.5}Sn_{0.5}I_3$ material. This concentration of DMACl caused the crystallisation to occur via a polytype intermediate phase not present in the DMSO containing inks. The resulting films showed a vastly different morphology, and preferred orientation. Devices fabricated using DMACl were able to reach comparable PCEs to those using DMSO, and, when aged in air, champion devices were able to achieve a T_{80} of over 400 hours compared to those made using DMSO having a T_{80} of only 68 hours. This chapter proved that removal of DMSO for Sn-containing perovskites is possible whilst still achieving high performance. It also proved that the choice of solvent and processing methodology can greatly enhance the ambient stability of resulting devices.

The investigations in this thesis have shown that $FA_{0.83}Cs_{0.17}Pb_{0.5}Sn_{0.5}I_3$ absorbers have excellent optoelectronic properties with much scope for improvement. These properties allow this material to be deployed into highly efficient tandems, which could prove crucial for future power generation.

Chapter 8

References

1. Steinberger, J. K., Lamb, W. F. & Sakai, M. Your money or your life? The carbon-development paradox. *Environ. Res. Lett.* **15**, 044016 (2020).
2. Hall, C., Tharakan, P., Hallock, J., Cleveland, C. & Jefferson, M. Hydrocarbons and the evolution of human culture. *Nature* **426**, 318–322 (2003).
3. Höök, M. & Tang, X. Depletion of fossil fuels and anthropogenic climate change—A review. *Energy Policy* **52**, 797–809 (2013).
4. Armaroli, N. & Vincenzo Balzani. *Energy for a Sustainable World - From the Oil Age to a Sun-Powered Future*. (WILEY-VCH).
5. Is the climate warming? | Royal Society. https://royalsociety.org/topics-policy/projects/climate-change-evidence-causes/question-1/.
6. Historic June heat wave smashes records in Europe - The Washington Post. https://www.washingtonpost.com/climate-environment/2022/06/20/france-germany-spain-europe-heatwave/.
7. Record high temperatures verified. *Met Office* https://www.metoffice.gov.uk/about-us/press-office/news/weather-and-climate/2022/record-high-temperatures-verified.

8. Maslanik, J. A. *et al.* A younger, thinner Arctic ice cover: Increased potential for rapid, extensive sea-ice loss. *Geophysical Research Letters* **34**, (2007).
9. Kimothi, S. *et al.* Intelligent energy and ecosystem for real-time monitoring of glaciers. *Computers and Electrical Engineering* **102**, 108163 (2022).
10. Chaudhary, C., Richardson, A. J., Schoeman, D. S. & Costello, M. J. Global warming is causing a more pronounced dip in marine species richness around the equator. *Proceedings of the National Academy of Sciences* **118**, e2015094118 (2021).
11. Watts, S. H. *et al.* Riding the elevator to extinction: Disjunct arctic-alpine plants of open habitats decline as their more competitive neighbours expand. *Biological Conservation* **272**, 109620 (2022).
12. Wang, X. *et al.* Enhanced habitat loss of the Himalayan endemic flora driven by warming-forced upslope tree expansion. *Nat Ecol Evol* **6**, 890–899 (2022).
13. Penn, J. L. & Deutsch, C. Avoiding ocean mass extinction from climate warming. *Science* **376**, 524–526 (2022).
14. Di Napoli, C. *et al.* Tracking the impacts of climate change on human health via indicators: lessons from the Lancet Countdown. *BMC Public Health* **22**, 663 (2022).

15. Sagan, C. Pale blue dot : a vision of the human future in space : second draft. *Library of Congress, Washington, D.C. 20540 USA* https://www.loc.gov/item/cosmos000044/.

16. Kabir, E., Kumar, P., Kumar, S., Adelodun, A. A. & Kim, K.-H. Solar energy: Potential and future prospects. *Renewable and Sustainable Energy Reviews* **82**, 894–900 (2018).

17. BP Statistical Review of World Energy 2022. 60 (2022). https://www.bp.com/content/dam/bp/business-sites/en/global/corporate/pdfs/energy-economics/statistical-review/bp-stats-review-2022-full-report.pdf

18. In Depth | Sun. *NASA Solar System Exploration* https://solarsystem.nasa.gov/solar-system/sun/in-depth.

19. Li, Z. Prospects of Photovoltaic Technology. *Engineering* (2022) doi:10.1016/j.eng.2022.07.008.

20. Sahoo, S. K., Manoharan, B. & Sivakumar, N. Chapter 1 - Introduction: Why Perovskite and Perovskite Solar Cells? in *Perovskite Photovoltaics* (eds. Thomas, S. & Thankappan, A.) 1–24 (Academic Press, 2018). doi:10.1016/B978-0-12-812915-9.00001-0.

21. Kang, S. *et al.* Ultrathin, lightweight and flexible perovskite solar cells with an excellent power-per-weight performance. *Journal of Materials Chemistry A* **7**, 1107–1114 (2019).

22. Kantareddy, S. N. R. *et al.* Introducing flexible perovskites to the IoT world using photovoltaic-powered wireless tags.

23. Kojima, A., Teshima, K., Shirai, Y. & Miyasaka, T. Organometal Halide Perovskites as Visible-Light Sensitizers for Photovoltaic Cells. *J. Am. Chem. Soc.* **131**, 6050–6051 (2009).

24. Min, H. *et al.* Perovskite solar cells with atomically coherent interlayers on SnO2 electrodes. *Nature* **598**, 444–450 (2021).

25. Swartwout, R., Hoerantner, M. T. & Bulović, V. Scalable Deposition Methods for Large-area Production of Perovskite Thin Films. *Energy & Environmental Materials* **2**, 119–145 (2019).

26. Jaysankar, M. *et al.* Toward scalable perovskite-based multijunction solar modules. *Progress in Photovoltaics: Research and Applications* **27**, 733–738 (2019).

27. Khan, F., Rezgui, B. D., Khan, M. T. & Al-Sulaiman, F. Perovskite-based tandem solar cells: Device architecture, stability, and economic perspectives. *Renewable and Sustainable Energy Reviews* **165**, 112553 (2022).

28. Atkins, P., Juilo de Paula & James Keeler. *Atkin's Physical Chemistry*. (Oxford University Press).

29. Housecroft, C. E. & Constable, E. C. *An Introduction to Organic, Inorganic and Physical Chemistry*. (Pearson Education Ltd).

30. Flowers, P., Theopold, K., Langley, R., Neth, E. J. & Robinson, W. R. Chemistry: Atoms First 2e. 1225.

31. Streetman, B. G. & Banerjee, S. *Solid State Electronic Devices*. (Pearson Education Ltd).

32. Yu, P. & Manuel Cardona. *Fundamentals of Semiconductors, Physics and Materials Properties*.

33. Nelson, J. *The Physics of Solar Cells*.

34. Wurfel, P. *Physics of Solar Cells - From Principles to New Concepts*. (WILEY-VCH).

35. Luo, D., Su, R., Zhang, W., Gong, Q. & Zhu, R. Minimizing non-radiative recombination losses in perovskite solar cells. *Nat Rev Mater* **5**, 44–60 (2020).

36. Abou-Ras, D., Kirchartz, T. & Rau, U. *Advanced Characterization Techniques for Thin Film Solar Cells*. (WILEY-VCH).

37. Manser, J. S., Christians, J. A. & Kamat, P. V. Intriguing Optoelectronic Properties of Metal Halide Perovskites. *Chem. Rev.* **116**, 12956–13008 (2016).

38. Miyasaka, T. *Perovskite Photovoltaics and Optoelectronics: From Fundamentals to Advanced Applications*. (WILEY-VCH).

39. Weber, D. CH3NH3PbX3, ein Pb(II)-System mit kubischer Perowskitstruktur / CH3NH3PbX3, a Pb(II)-System with Cubic Perovskite Structure. *Zeitschrift für Naturforschung B* **33**, 1443–1445 (1978).

40. Efficient Hybrid Solar Cells Based on Meso-Superstructured Organometal Halide Perovskites | Science. https://www.science.org/doi/10.1126/science.1228604.

41. Kim, H.-S. *et al.* Lead Iodide Perovskite Sensitized All-Solid-State Submicron Thin Film Mesoscopic Solar Cell with Efficiency Exceeding 9%. *Sci Rep* **2**, 591 (2012).
42. Stranks, S. D. *et al.* Electron-Hole Diffusion Lengths Exceeding 1 Micrometer in an Organometal Trihalide Perovskite Absorber. *Science* **342**, 341–344 (2013).
43. Jeong, J. *et al.* Pseudo-halide anion engineering for α-FAPbI3 perovskite solar cells. *Nature* **592**, 381–385 (2021).
44. Goetzberger, A., Joachim Knobloch & Bernhard Voss. *Crystalline Silicon Solar Cells*. (WILEY-VCH).
45. Søndenå, R., Stølen, S., Ravindran, P., Grande, T. & Allan, N. L. Corner-versus face-sharing octahedra in perovskites (. *Phys. Rev. B* **75**, 184105 (2007).
46. Park, N.-G., Grätzel, M. & Miyasaka, T. *Organic-Inorganic Halide Perovskite Photovoltaics - From Fundamentals to Device Architectures*. (Springer).
47. McMeekin, D. P. *et al.* A mixed-cation lead mixed-halide perovskite absorber for tandem solar cells. *Science* **351**, 151–155 (2016).
48. Noh, J. H., Im, S. H., Heo, J. H., Mandal, T. N. & Seok, S. I. Chemical Management for Colorful, Efficient, and Stable Inorganic–Organic Hybrid Nanostructured Solar Cells. *Nano Lett.* **13**, 1764–1769 (2013).

49. Eperon, G. E. *et al.* Formamidinium lead trihalide: a broadly tunable perovskite for efficient planar heterojunction solar cells. *Energy Environ. Sci.* **7**, 982–988 (2014).

50. K. Noel, N. *et al.* Lead-free organic–inorganic tin halide perovskites for photovoltaic applications. *Energy & Environmental Science* **7**, 3061–3068 (2014).

51. Pitaro, M., Tekelenburg, E. K., Shao, S. & Loi, M. A. Tin Halide Perovskites: From Fundamental Properties to Solar Cells. *Advanced Materials* **34**, 2105844 (2022).

52. Leijtens, T., Prasanna, R., Gold-Parker, A., Toney, M. F. & McGehee, M. D. Mechanism of Tin Oxidation and Stabilization by Lead Substitution in Tin Halide Perovskites. *ACS Energy Lett.* **2**, 2159–2165 (2017).

53. Im, J., Stoumpos, C. C., Jin, H., Freeman, A. J. & Kanatzidis, M. G. Antagonism between Spin–Orbit Coupling and Steric Effects Causes Anomalous Band Gap Evolution in the Perovskite Photovoltaic Materials CH3NH3Sn1–xPbxI3. *J. Phys. Chem. Lett.* **6**, 3503–3509 (2015).

54. Goyal, A. *et al.* Origin of Pronounced Nonlinear Band Gap Behavior in Lead–Tin Hybrid Perovskite Alloys. *Chem. Mater.* **30**, 3920–3928 (2018).

55. Gu, S. *et al.* Tin and Mixed Lead–Tin Halide Perovskite Solar Cells: Progress and their Application in Tandem Solar Cells. *Advanced Materials* **32**, 1907392 (2020).

56. Leijtens, T. *et al.* Tin–lead halide perovskites with improved thermal and air stability for efficient all-perovskite tandem solar cells. *Sustainable Energy & Fuels* **2**, 2450–2459 (2018).

57. Hu, S. *et al.* Optimized carrier extraction at interfaces for 23.6% efficient tin–lead perovskite solar cells. *Energy & Environmental Science* **15**, 2096–2107 (2022).

58. Hu, S. *et al.* Mixed lead–tin perovskite films with >7 µs charge carrier lifetimes realized by maltol post-treatment. *Chem. Sci.* **12**, 13513–13519 (2021).

59. Eperon, G. E. *et al.* Perovskite-perovskite tandem photovoltaics with optimized band gaps. *Science* **354**, 861–865 (2016).

60. Tong, J. *et al.* Carrier control in Sn–Pb perovskites via 2D cation engineering for all-perovskite tandem solar cells with improved efficiency and stability. *Nat Energy* **7**, 642–651 (2022).

61. Tong, J. *et al.* Carrier lifetimes of >1 µs in Sn-Pb perovskites enable efficient all-perovskite tandem solar cells. *Science* **364**, 475–479 (2019).

62. Yang, Z. *et al.* Enhancing electron diffusion length in narrow-bandgap perovskites for efficient monolithic perovskite tandem solar cells. *Nat Commun* **10**, 4498 (2019).

63. Lin, R. *et al.* Monolithic all-perovskite tandem solar cells with 24.8% efficiency exploiting comproportionation to suppress Sn(II) oxidation in precursor ink. *Nat Energy* **4**, 864–873 (2019).

64. Hörantner, M. T. *et al.* The Potential of Multijunction Perovskite Solar Cells. *ACS Energy Lett.* **2**, 2506–2513 (2017).

65. Eperon, G. E., Hörantner, M. T. & Snaith, H. J. Metal halide perovskite tandem and multiple-junction photovoltaics. *Nat Rev Chem* **1**, 1–18 (2017).

66. Shockley, W. & Queisser, H. J. Detailed Balance Limit of Efficiency of p-n Junction Solar Cells. 11.

67. Guillemoles, J.-F., Kirchartz, T., Cahen, D. & Rau, U. Guide for the perplexed to the Shockley–Queisser model for solar cells. *Nat. Photonics* **13**, 501–505 (2019).

68. Semonin, O. E. *et al.* Peak External Photocurrent Quantum Efficiency Exceeding 100% via MEG in a Quantum Dot Solar Cell. *Science* **334**, 1530–1533 (2011).

69. Cotal, H. *et al.* III–V multijunction solar cells for concentrating photovoltaics. *Energy Environ. Sci.* **2**, 174–192 (2009).

70. Lee, K., Zimmerman, J. D., Hughes, T. W. & Forrest, S. R. Non-Destructive Wafer Recycling for Low-Cost Thin-Film Flexible Optoelectronics. *Advanced Functional Materials* **24**, 4284–4291 (2014).

71. Ibn-Mohammed, T. *et al.* Perovskite solar cells: An integrated hybrid lifecycle assessment and review in comparison with other photovoltaic technologies. *Renewable and Sustainable Energy Reviews* **80**, 1321–1344 (2017).

72. Lin, R. *et al.* All-perovskite tandem solar cells with improved grain surface passivation. *Nature* **603**, 73–78 (2022).

73. Jeon, N. J. *et al.* Solvent engineering for high-performance inorganic–organic hybrid perovskite solar cells. *Nature Mater* **13**, 897–903 (2014).

74. Ashiotis, G. *et al.* The fast azimuthal integration Python library: pyFAI. *J Appl Cryst* **48**, 510–519 (2015).

75. de Quilettes, D. W. *et al.* Impact of microstructure on local carrier lifetime in perovskite solar cells. *Science* **348**, 683–686 (2015).

76. Kirchartz, T., Márquez, J. A., Stolterfoht, M. & Unold, T. Photoluminescence-Based Characterization of Halide Perovskites for Photovoltaics. *Advanced Energy Materials* **10**, 1904134 (2020).

77. de Mello, J. C., Wittmann, H. F. & Friend, R. H. An improved experimental determination of external photoluminescence quantum efficiency. *Advanced Materials* **9**, 230–232 (1997).

78. Dasgupta, A. *et al.* Visualizing Macroscopic Inhomogeneities in Perovskite Solar Cells. *ACS Energy Lett.* **7**, 2311–2322 (2022).

79. Snaith, H. J. How should you measure your excitonic solar cells? *Energy Environ. Sci.* **5**, 6513–6520 (2012).

80. Ball, J. M. & Petrozza, A. Defects in perovskite-halides and their effects in solar cells. *Nat Energy* **1**, 1–13 (2016).

81. Stewart, R. J., Grieco, C., Larsen, A. V., Doucette, G. S. & Asbury, J. B. Molecular Origins of Defects in Organohalide Perovskites and Their

Influence on Charge Carrier Dynamics. *J. Phys. Chem. C* **120**, 12392–12402 (2016).

82. Wang, A. *et al.* Recent promise of lead-free halide perovskites in optoelectronic applications. *Chemical Engineering Journal* **451**, 138926 (2023).
83. J. Oliver, R. D. *et al.* Understanding and suppressing non-radiative losses in methylammonium-free wide-bandgap perovskite solar cells. *Energy & Environmental Science* **15**, 714–726 (2022).
84. Mahesh, S. *et al.* Revealing the origin of voltage loss in mixed-halide perovskite solar cells. *Energy & Environmental Science* **13**, 258–267 (2020).
85. Caprioglio, P. *et al.* On the Relation between the Open-Circuit Voltage and Quasi-Fermi Level Splitting in Efficient Perovskite Solar Cells. *Advanced Energy Materials* **9**, 1901631 (2019).
86. Gao, F. *et al.* Enhanced performance of tin halide perovskite solar cell by addition of lead thiocyanate. *RSC Adv* **8**, 14025–14030.
87. Lian, X. *et al.* Highly Efficient Sn/Pb Binary Perovskite Solar Cell via Precursor Engineering: A Two-Step Fabrication Process. *Advanced Functional Materials* **29**, 1807024 (2019).
88. Khadka, D. B., Shirai, Y., Yanagida, M. & Miyano, K. Pseudohalide Functional Additives in Tin Halide Perovskite for Efficient and Stable Pb-Free Perovskite Solar Cells. *ACS Appl. Energy Mater.* **4**, 12819–12826 (2021).

89. Klug, M. T. *et al.* Metal composition influences optoelectronic quality in mixed-metal lead–tin triiodide perovskite solar absorbers. *Energy Environ. Sci.* **13**, 1776–1787 (2020).

90. Bowman, A. R. *et al.* Microsecond Carrier Lifetimes, Controlled p-Doping, and Enhanced Air Stability in Low-Bandgap Metal Halide Perovskites. *ACS Energy Lett.* **4**, 2301–2307 (2019).

91. Werner, J. *et al.* Improving Low-Bandgap Tin–Lead Perovskite Solar Cells via Contact Engineering and Gas Quench Processing. *ACS Energy Lett.* **5**, 1215–1223 (2020).

92. Wolff, C. M., Caprioglio, P., Stolterfoht, M. & Neher, D. Nonradiative Recombination in Perovskite Solar Cells: The Role of Interfaces. *Advanced Materials* **31**, 1902762 (2019).

93. Stolterfoht, M. *et al.* The impact of energy alignment and interfacial recombination on the internal and external open-circuit voltage of perovskite solar cells. *Energy & Environmental Science* **12**, 2778–2788 (2019).

94. Peña-Camargo, F. *et al.* Halide Segregation versus Interfacial Recombination in Bromide-Rich Wide-Gap Perovskite Solar Cells. *ACS Energy Lett.* **5**, 2728–2736 (2020).

95. Stolterfoht, M. *et al.* The impact of energy alignment and interfacial recombination on the internal and external open-circuit voltage of perovskite solar cells. *Energy & Environmental Science* **12**, 2778–2788 (2019).

96. Al-Ashouri, A. *et al.* Conformal monolayer contacts with lossless interfaces for perovskite single junction and monolithic tandem solar cells. *Energy & Environmental Science* **12**, 3356–3369 (2019).

97. Al-Ashouri, A. *et al.* Monolithic perovskite/silicon tandem solar cell with >29% efficiency by enhanced hole extraction. *Science* **370**, 1300–1309 (2020).

98. Song, D., Narra, S., Li, M.-Y., Lin, J.-S. & Diau, E. W.-G. Interfacial Engineering with a Hole-Selective Self-Assembled Monolayer for Tin Perovskite Solar Cells via a Two-Step Fabrication. *ACS Energy Lett.* **6**, 4179–4186 (2021).

99. Phung, N. *et al.* Enhanced Self-Assembled Monolayer Surface Coverage by ALD NiO in p-i-n Perovskite Solar Cells. *ACS Appl. Mater. Interfaces* **14**, 2166–2176 (2022).

100. Qiu, W. *et al.* Pinhole-free perovskite films for efficient solar modules. *Energy & Environmental Science* **9**, 484–489 (2016).

101. Abdelsamie, M. *et al.* Mechanism of Additive-Assisted Room-Temperature Processing of Metal Halide Perovskite Thin Films. *ACS Appl. Mater. Interfaces* **13**, 13212–13225 (2021).

102. Jiang, T. *et al.* Realizing High Efficiency over 20% of Low-Bandgap Pb–Sn-Alloyed Perovskite Solar Cells by In Situ Reduction of Sn4+. *Solar RRL* **4**, 1900467 (2020).

103. Castro-Méndez, A.-F., Hidalgo, J. & Correa-Baena, J.-P. The Role of Grain Boundaries in Perovskite Solar Cells. *Advanced Energy Materials* **9**, 1901489 (2019).

104. Wu, G. *et al.* Enlarging grain sizes for efficient perovskite solar cells by methylamine chloride assisted recrystallization. *Journal of Energy Chemistry* **65**, 55–61 (2022).

105. Yun, J. S. *et al.* Humidity-Induced Degradation via Grain Boundaries of HC(NH2)2PbI3 Planar Perovskite Solar Cells. *Advanced Functional Materials* **28**, 1705363 (2018).

106. Hui, Y. *et al.* Stability of Perovskite Thin Films under Working Condition: Bias-Dependent Degradation and Grain Boundary Effects. *Advanced Functional Materials* **31**, 2103894 (2021).

107. Wang, Q. *et al.* Scaling behavior of moisture-induced grain degradation in polycrystalline hybrid perovskite thin films. *Energy & Environmental Science* **10**, 516–522 (2017).

108. Schneider, C. A., Rasband, W. S. & Eliceiri, K. W. NIH Image to ImageJ: 25 years of image analysis. *Nat Methods* **9**, 671–675 (2012).

109. Pazos-Outón, L. M., Xiao, T. P. & Yablonovitch, E. Fundamental Efficiency Limit of Lead Iodide Perovskite Solar Cells. *J. Phys. Chem. Lett.* **9**, 1703–1711 (2018).

110. Mertens, K. *Photovoltaics - Fundamentals, Technology and Practice*. (Wiley, 2014).

111. Ulatowski, A. M., Herz, L. M. & Johnston, M. B. Terahertz Conductivity Analysis for Highly Doped Thin-Film Semiconductors. *J Infrared Milli Terahz Waves* **41**, 1431–1449 (2020).

112. Stoumpos, C. C., Mao, L., Malliakas, C. D. & Kanatzidis, M. G. Structure–Band Gap Relationships in Hexagonal Polytypes and Low-Dimensional Structures of Hybrid Tin Iodide Perovskites. *Inorg. Chem.* **56**, 56–73 (2017).

113. Straus, D. B., Guo, S. & Cava, R. J. Kinetically Stable Single Crystals of Perovskite-Phase CsPbI3. *J. Am. Chem. Soc.* **141**, 11435–11439 (2019).

114. Nath, N. C. D., Kang, H. C. & Lee, J.-J. Solvent engineering for two-dimensional perovskite of guanidium lead iodide. *Synthetic Metals* **291**, 117175 (2022).

115. Momma, K. & Izumi, F. VESTA 3 for three-dimensional visualization of crystal, volumetric and morphology data. *J Appl Cryst* **44**, 1272–1276 (2011).

116. Wang, Q. *et al.* Impact of the Hole Transport Layer on the Charge Extraction of Ruddlesden–Popper Perovskite Solar Cells. *ACS Appl. Mater. Interfaces* **12**, 29505–29512 (2020).

117. Wang, Y. *et al.* PTAA as Efficient Hole Transport Materials in Perovskite Solar Cells: A Review. *Solar RRL* **6**, 2200234 (2022).

118. Thiesbrummel, J. *et al.* Universal Current Losses in Perovskite Solar Cells Due to Mobile Ions. *Advanced Energy Materials* **11**, 2101447 (2021).

119. Rebetez, G., Bardagot, O., Affolter, J., Réhault, J. & Banerji, N. What Drives the Kinetics and Doping Level in the Electrochemical Reactions of PEDOT:PSS? *Advanced Functional Materials* **32**, 2105821 (2022).

120. Stolterfoht, M., Wolff, C.M., Márquez, J.A. et al. Visualization and suppression of interfacial recombination for high-efficiency large-area pin perovskite solar cells. Nat Energy 3, 847–854 (2018). https://doi.org/10.1038/s41560-018-0219-8 121. Sun, Y. *et al.* A full range of defect passivation strategy targeting efficient and stable planar perovskite solar cells. *Chemical Engineering Journal* **451**, 138800 (2023).

122. Kim, H. *et al.* Boosting the performance and stability of quasi-two-dimensional tin-based perovskite solar cells using the formamidinium thiocyanate additive. *J. Mater. Chem. A* **6**, 18173–18182 (2018).

123. Shahbazi, S., Li, M.-Y., Fathi, A. & Diau, E. W.-G. Realizing a Cosolvent System for Stable Tin-Based Perovskite Solar Cells Using a Two-Step Deposition Approach. *ACS Energy Lett.* **5**, 2508–2511 (2020).

124. Ehrler, B. *et al.* Photovoltaics Reaching for the Shockley–Queisser Limit. *ACS Energy Lett.* **5**, 3029–3033 (2020).

125. Werner, J. *et al.* Efficient Near-Infrared-Transparent Perovskite Solar Cells Enabling Direct Comparison of 4-Terminal and Monolithic Perovskite/Silicon Tandem Cells. *ACS Energy Lett.* **1**, 474–480 (2016).

126. Perovskite-perovskite tandem photovoltaics with optimized band gaps | Science. https://www.science.org/doi/10.1126/science.aaf9717.

127. Agarwal, S. & Nair, P. R. Pinhole induced efficiency variation in perovskite solar cells. *Journal of Applied Physics* **122**, 163104 (2017).

128. Liu, H. *et al.* Double-Side Crystallization Tuning to Achieve over 1 μm Thick and Well-Aligned Block-Like Narrow-Bandgap Perovskites for High-Efficiency Near-Infrared Photodetectors. *Advanced Functional Materials* **31**, 2010532 (2021).

129. Wang, M., Fei, C., Uddin, M. A. & Huang, J. Influence of voids on the thermal and light stability of perovskite solar cells. *Science Advances* **8**, eabo5977 (2022).

130. Xiao, K. *et al.* All-perovskite tandem solar cells with 24.2% certified efficiency and area over 1 cm2 using surface-anchoring zwitterionic antioxidant. *Nat Energy* **5**, 870–880 (2020).

131. Kapil, G. *et al.* Tin-Lead Perovskite Fabricated via Ethylenediamine Interlayer Guides to the Solar Cell Efficiency of 21.74%. *Advanced Energy Materials* **11**, 2101069 (2021).

132. Highly Efficient 17.6% Tin–Lead Mixed Perovskite Solar Cells Realized through Spike Structure | Nano Letters. https://pubs.acs.org/doi/10.1021/acs.nanolett.8b00701.

133. Wang, H., He, Y., Li, Y. & Su, H. Photophysical and Electronic Properties of Five PCBM-like C60 Derivatives: Spectral and Quantum Chemical View. *J. Phys. Chem. A* **116**, 255–262 (2012).

134. Li, Y. *et al.* Bandgap tuning strategy by cations and halide ions of lead halide perovskites learned from machine learning. *RSC Advances* **11**, 15688–15694 (2021).

135. Zhao, D. *et al.* Low-bandgap mixed tin–lead iodide perovskite absorbers with long carrier lifetimes for all-perovskite tandem solar cells. *Nat Energy* **2**, 1–7 (2017).

136. Wang, C., Song, Z., Li, C., Zhao, D. & Yan, Y. Low-Bandgap Mixed Tin-Lead Perovskites and Their Applications in All-Perovskite Tandem Solar Cells. *Advanced Functional Materials* **29**, 1808801 (2019).

137. Palmstrom, A. F. *et al.* Enabling Flexible All-Perovskite Tandem Solar Cells. *Joule* **3**, 2193–2204 (2019).

138. Saidaminov, M. I. *et al.* Conventional Solvent Oxidizes Sn(II) in Perovskite Inks. *ACS Energy Lett.* **5**, 1153–1155 (2020).

139. Pascual, J. *et al.* Origin of Sn(ii) oxidation in tin halide perovskites. *Materials Advances* **1**, 1066–1070 (2020).

140. Li, C. *et al.* Low-bandgap mixed tin–lead iodide perovskites with reduced methylammonium for simultaneous enhancement of solar cell efficiency and stability. *Nat Energy* **5**, 768–776 (2020).

141. Solvents for Processing Stable Tin Halide Perovskites | ACS Energy Letters. https://pubs.acs.org/doi/10.1021/acsenergylett.0c02656.

142. Takahashi, Y. *et al.* Charge-transport in tin-iodide perovskite CH3NH3SnI3: origin of high conductivity. *Dalton Trans.* **40**, 5563–5568 (2011).

143. Zhou, X. *et al.* Highly Efficient and Stable GABr-Modified Ideal-Bandgap (1.35 eV) Sn/Pb Perovskite Solar Cells Achieve 20.63% Efficiency with a Record Small Voc Deficit of 0.33 V. *Advanced Materials* **32**, 1908107 (2020).

144. Yu, Y. *et al.* A Review on Gas-Quenching Technique for Efficient Perovskite Solar Cells. *Solar RRL* **5**, 2100386 (2021).

145. Han, Y. *et al.* Controlling Spatial Crystallization Uniformity and Phase Orientation of Quasi-2D Perovskite-Based Light-Emitting Diodes Using Lewis Bases. *Advanced Materials Interfaces* **7**, 1901860 (2020).

146. Shin, S. S. *et al.* Solvent-Engineering Method to Deposit Compact Bismuth-Based Thin Films: Mechanism and Application to Photovoltaics. *Chem. Mater.* **30**, 336–343 (2018).

147. Gratia, P. *et al.* The Many Faces of Mixed Ion Perovskites: Unraveling and Understanding the Crystallization Process. *ACS Energy Lett.* **2**, 2686–2693 (2017).

148. Mohammed, M. K. A., Esmail Shalan, A., Dehghanipour, M. & Mohseni, H. R. Improved mixed-dimensional 3D/2D perovskite layer with formamidinium bromide salt for highly efficient and stable perovskite solar cells. *Chemical Engineering Journal* **428**, 131185 (2022).

149. Zhang, X. *et al.* Formamidinium-Based Quasi-2D Perovskite Nanoplates With Dimensionally Tuned Optical Properties. *IEEE Transactions on Nanotechnology* **17**, 1165–1170 (2018).

150. Ahn, N. *et al.* Highly Reproducible Perovskite Solar Cells with Average Efficiency of 18.3% and Best Efficiency of 19.7% Fabricated via Lewis Base Adduct of Lead(II) Iodide. *J. Am. Chem. Soc.* **137**, 8696–8699 (2015).

151. Zhang, Q. *et al.* Perovskite films prepared by solvent volatilization via DMSO-based intermediate phase for photovoltaics. *Solar Energy* **218**, 383–391 (2021).

152. Eperon, G. E. *et al.* The Role of Dimethylammonium in Bandgap Modulation for Stable Halide Perovskites. *ACS Energy Lett.* **5**, 1856–1864 (2020).

153. Mundt, L. E. *et al.* Surface-Activated Corrosion in Tin–Lead Halide Perovskite Solar Cells. *ACS Energy Lett.* **5**, 3344–3351 (2020).

154. Lim, V. J.-Y. *et al.* Air-Degradation Mechanisms in Mixed Lead-Tin Halide Perovskites for Solar Cells. *Advanced Energy Materials* **n/a**, 2200847.

155. Lanzetta, L. *et al.* Degradation mechanism of hybrid tin-based perovskite solar cells and the critical role of tin (IV) iodide. *Nat Commun* **12**, 2853 (2021).

156. Lanzetta, L., Aristidou, N. & Haque, S. A. Stability of Lead and Tin Halide Perovskites: The Link between Defects and Degradation. *J. Phys. Chem. Lett.* **11**, 574–585 (2020).

157. Lang, F. *et al.* Influence of Radiation on the Properties and the Stability of Hybrid Perovskites. *Advanced Materials* **30**, 1702905 (2018).